Title

Advancements in Aerosol Research: Evaluation of DIY Low-Cost Air Cleaners, Humidified Aerosol Optical Measurement Methodology, and Absorption Characterization of Urban Aerosols

Author

Dal Porto, Rachael

Publication Date

2024

Peer reviewed|Thesis/dissertation

Advancements in Aerosol Research: Evaluation of DIY Low-Cost Air Cleaners, Humidified Aerosol Optical Measurement Methodology, and Absorption Characterization of Urban Aerosols

By

RACHAEL DAL PORTO

DISSERTATION

Submitted in partial satisfaction of the requirements for the degree of

DOCTOR OF PHILOSOPHY

in

Civil and Environmental Engineering

in the

OFFICE OF GRADUATE STUDIES

of the

UNIVERSITY OF CALIFORNIA

DAVIS

Approved:

Christopher Cappa, Chair

Qi Zhang

Allison Aiken

Committee in Charge

2025

ABSTRACT

This dissertation presents findings from three independent but complementary studies addressing aerosol filtration efficiency of and in-room air cleaner and laboratory and field studies on the optical properties of absorbing aerosols in the atmosphere. First, the performance of a low-cost, DIY air cleaner that uses MERV-13 filters coupled with a standard box fan, known as the Corsi-Rosenthal Box (CR Box), was assessed using both research-grade instrumentation and low-cost sensors. The effective clean air delivery rate (CADR) depends on fan speed and ranged from 600 to 850 $ft^3\ min^{-1}$ (1019 to 1444 $m^3\ h^{-1}$), demonstrating the CR Box's effectiveness in reducing indoor particle concentrations as a cost-efficient alternative to more expensive, commercially available HEPA air purifiers. Second, we described and characterized the performance of a humidified cavity attenuated phase shift spectrometer (H-CAPS-PM_{SSA}) system that measures aerosol extinction and scattering, from which aerosol absorption is derived, and which has been modified to enable measurements at varying relative humidities up to ~90%. Using an updated truncation correction method, the modified system allows for accurate measurement of the effects of water uptake on light absorption, revealing critical insights into humidity-driven absorption enhancement. Lastly, during the Tracking Aerosol Convection Interactions Experiment (TRACER) campaign in Houston, Texas, optical properties of black carbon (BC), brown carbon (BrC), and dust were characterized. Measured mass absorption coefficients (MAC) were determined for BC, BrC, and dust were retrieved along with the dust refractive index. Significant contributions of dust and BC to regional absorption were determined, with BC accounting for 61% and 75% of absorption at 405 nm and 532 nm, respectively, dust accounting for 34% and 16% of absorption at 405nm and 532nm, and BrC accounting for 6% and 9%, respectively. These studies collectively advance understanding of cost-effective indoor air

cleaner performance, aerosol optical properties under humidified conditions, and the optical properties of absorbing aerosols in complex urban environments.

DEDICATION

To Mom and Dad,

for your love, support, and endless encouragement.

ACKNOWLEDGEMENTS

I would like to express my gratitude to my advisor, Dr. Chris Cappa, for his support throughout my PhD journey. His mentorship, encouragement, and insights have been invaluable, and I am grateful for the opportunities to learn and grow under his guidance. Thank you to my lab mate, Theresa, for her guidance and willingness to share her expertise not only in the field, but professionally as well. Her advice and camaraderie have made this journey not only manageable but also enjoyable.

I also want to thank my cats, Lotus and Nutmeg, for their constant companionship and their ability to bring calm even on the most stressful days. A heartfelt thank you to my partner, Chase, for being by my side throughout this journey, offering support and encouragement on both the good days and the difficult ones.

And most of all, I am deeply grateful to my parents, Bobby and Jill, for their unwavering support and belief in me. Their constant encouragement has been my strength, and their support has carried me through both the challenges and successes of this journey. Thank you for teaching me the value of hard work, for always being there when I needed guidance, and for believing in me even when I doubted myself. I couldn't have done this without you.

To all who have contributed to this journey, directly or indirectly, thank you.

MATERIAL PREVIOUSLY PUBLISHED OR PENDING PUBLISHING

Chapter 2, in full, is a reprint of the material as it appears in Aerosol Science and Technology. Dal Porto, R., Kunz, M. N., Pistochini, T., Corsi, R. L., & Cappa, C. D. (2022). Characterizing the performance of a do-it-yourself (DIY) box fan air filter. *Aerosol Science and Technology*, *56*(6), 564–572. https://doi.org/10.1080/02786826.2022.2054674. The dissertation author was the primary research and author of this paper.

Chapter 3, in part is currently being prepared for submission for publication of the material. The dissertation author was the primary researcher and author of this material.

Chapter 4, in part is currently being prepared for submission for publication of the material. The dissertation author was the primary researcher and author of this material.

TABLE OF CONTENTS

LIST OF FIGURES

LIST OF TABLES

1 INTRODUCTION

Atmospheric aerosols impact human health (WHO, 2024), air quality, and the climate (IPCC, 2023). Poor indoor air quality is a leading cause of death (WHO, 2024), and as such, indoor air filtration methods and their efficiency has become a topic of global interest, especially post-COVID-19 pandemic. Simultaneously, atmospheric aerosols, play a large role in Earth's radiative balance by both scattering and absorbing solar radiation. This dissertation addresses these interconnected themes by presenting investigations into the aerosol filtration efficiency of a DIY air cleaner (Chapter 2), the development and characterization of a new instrument to measure light absorption at elevated relative humidity (Chapter 3), and the optical properties of absorbing aerosols measured in Houston, Texas during the TRACER-CAT field study (Chapter 4).

1.1 Cost Effective Indoor Air Filtration

Filtration systems, whether integrated into ventilation systems or used as stand-alone portable units, are an effective method for reducing indoor particle concentrations (Curtius et al. 2021; Kelly and Fussell 2019; McNamara et al. 2017). Filters are rated by their minimum efficiency reporting value (MERV), with the most efficient being high-efficiency particulate air (HEPA) filters, which remove at least 99.97% of particles measuring 0.3 microns in diameter (ASHRAE, 2017). HEPA filters are widely used in commercial air purifiers and have demonstrated substantial benefits, including reducing the risk of airborne transmission of infectious diseases such as COVID-19 (Liu et al. 2022) and mitigating exposure to traffic-related aerosols and woodsmoke (Cox et al. 2018; Allen et al. 2011). Due to pressure drop and space constraints, HEPA filters are rarely used in ventilation systems but are common in portable air cleaners (Shaughnessy and Sextro 2006), however, their high cost and energy requirements often limit accessibility and adoption in resource-constrained settings (Pistochini, 2021).

In response, the Corsi-Rosenthal Box (CR Box) has emerged as a low-cost, do-it-yourself (DIY) alternative. The CR Box was originally proposed by Richard Corsi on Twitter and with Jim Rosenthal making the first prototype (Rosenthal 2020). The CR Box is constructed with 5 MERV-13 filters and a common box fan, offering an affordable solution for reducing particle concentrations in classrooms, homes, and other indoor environments. This study characterizes the size-dependent particle decay rates and clean air delivery rate (CADR) of the CR Box in comparison to commercially available, though often cost-prohibitive, HEPA-based air cleaners. Measurements were conducted using both research-grade and low-cost instruments, ensuring accessibility for a broader audience. By exploring the efficiency and cost-effectiveness of the CR Box, this work contributes to improving access to a more accessible air cleaner.

1.2 Absorbing Aerosols

Atmospheric aerosols impact climate both directly and indirectly due to their interactions with incoming solar radiation and their effect on cloud physics (IPCC, 2023; Andreae and Rosenfeld 2008; Ramanathan and Carmichael 2008). Aerosols directly impact Earth's radiative forcing by both scattering and absorbing incoming solar radiation. When aerosols scatter incoming solar radiation, they provide a net cooling effect on the Earth's atmosphere as some radiation that would normally reach the Earth's surface is scattered back into space. If, instead, the aerosols absorb that radiation, they create a net warming effect. Aerosols that absorb solar radiation are collectively referred to as "absorbing aerosols" (AA) and include black carbon (BC), brown carbon (BrC), and dust.

BC, BrC, and dust differ in their optical properties, sources, and impacts. In contrast to purely scattering aerosols, AA have a generally positive net radiative forcing. BC is a product of incomplete combustion that strongly absorbs visible light, and is abundant in the atmosphere, and

as such is a major contributor to positive radiative forcing (Bond et al. 2013). BrC, a subset of organic aerosols formed from biomass burning and secondary organic aerosol formation, absorbs light primarily in the ultraviolet and visible regions (Laskin et al. 2015). Dust aerosols, produced via mechanical processes such as wind action, exhibit optical properties that vary with size and chemical composition (Rodriguez-Navarro et al. 2018).

1.3 Aerosol Optical Properties Under Humidification

When aerosols interact with light, they scatter or absorb that light, and the sum of those two is called extinction. Total light extinction by particles depends on size, concentration, composition, and the wavelength of the incident light (Seinfeld and Pandis 2016). Water uptake by an aerosol particle also has an impact on extinction and overall optical properties. The amount of water that a particle uptakes is a function of particle composition and atmospheric conditions. Water by itself is purely scattering at visible wavelengths, however, when coating absorbing aerosols it has the ability to enhance absorption(Khalizov et al. 2009; Mikhailov et al. 2006). The influence on optical properties owing to water uptake are characterized by $f(RH)_z$ which is the ratio of wet particle scattering, extinction, or absorption, to its dry counterpart.

$$f(RH)_z = \frac{bZ_{humidifie}}{bZ_{dry}} \text{ ; where Z = extinction, absorption, or scattering}$$

The impact water uptake has on absorption by aerosol particles is a key uncertainty contributing to overall radiative impact.

This study introduces a novel humidified cavity-attenuated phase shift particulate matter spectrometer (HCAPS PM_{SSA}) system for concurrent measurement of aerosol extinction and scattering (yielding absorption by difference) at varying humidity levels. By enabling precise characterization of absorption and single scattering albedo (SSA) under controlled humidified

conditions, the HCAPS system addresses critical uncertainties in understanding the optical properties of hygroscopic aerosols.

1.4 TRACER Field Campaign

Houston has a distinct combination of anthropogenic and natural emission sources, making it an interesting environment for observing the optical properties of absorbing aerosols. The region's subtropical climate, characterized by high humidity and frequent thunderstorms, significantly influences aerosol behavior, including hygroscopic growth and mixing state. Interactions involving high humidity, petrochemical industries, marine aerosols, and vehicular traffic contribute to aerosol mixing states and hygroscopic growth, affecting their optical properties. The TRACER campaign, conducted by the Department of Energy (DOE) in Houston, examined these interactions focusing on aerosol events observed at the AMF1 main site in La Porte, Texas. Here, we focus on measurements made during the Carbonaceous Aerosols Thrust (TRACER-CAT) sub-campaign over the period July 1 to July 31, 2022. Located near the Houston Ship Channel and surrounded by industrial facilities, La Porte experiences emissions from petrochemical plants, refineries, and transportation infrastructure, creating a diverse aerosol mix.

The TRACER campaign provided a platform to investigate aerosol events in Houston, shedding light on the contributions of BC, BrC, and dust to absorption and their regional radiative impacts. This study focuses on three distinct aerosol events observed during the campaign, examining the variability in BrC contributions and the role of dust on absorption. By leveraging *in situ* measurements of aerosol optical properties, this work advances understanding of absorbing aerosols and their implications for radiative forcing.

1.5 References

Allen, R.W., Carlsten, C., Karlen, B., Leckie, S., van Eeden, S., Vedal, S., Wong, I., and Brauer, M. (2011). An air filter intervention study of endothelial function among healthy adults in a woodsmoke-impacted community. Am J Respir Crit Care Med 183 (9):1222–1230. doi:10.1164/rccm.201010-1572OC.

Andreae, M.O. and Rosenfeld, D. (2008). Aerosol–cloud–precipitation interactions. Part 1. The nature and sources of cloud-active aerosols. Earth-Science Reviews 89 (1):13–41. doi:10.1016/j.earscirev.2008.03.001.

AR6 Climate Change 2022: Mitigation of Climate Change — IPCC. (n.d.). Available at https://www.ipcc.ch/report/sixth-assessment-report-working-group-3/ (Accessed 28 April 2022).

Bond, T.C., Doherty, S.J., Fahey, D.W., Forster, P.M., Berntsen, T., DeAngelo, B.J., Flanner, M.G., Ghan, S., Kärcher, B., Koch, D., Kinne, S., Kondo, Y., Quinn, P.K., Sarofim, M.C., Schultz, M.G., Schulz, M., Venkataraman, C., Zhang, H., Zhang, S., Bellouin, N., Guttikunda, S.K., Hopke, P.K., Jacobson, M.Z., Kaiser, J.W., Klimont, Z., Lohmann, U., Schwarz, J.P., Shindell, D., Storelvmo, T., Warren, S.G., and Zender, C.S. (2013). Bounding the role of black carbon in the climate system: A scientific assessment. Journal of Geophysical Research: Atmospheres 118 (11):5380–5552. doi:10.1002/jgrd.50171.

Cox, J., Isiugo, K., Ryan, P., Grinshpun, S.A., Yermakov, M., Desmond, C., Jandarov, R., Vesper, S., Ross, J., Chillrud, S., Dannemiller, K., and Reponen, T. (2018). Effectiveness of a portable air cleaner in removing aerosol particles in homes close to highways. Indoor Air 28 (6):818–827. doi:10.1111/ina.12502.

Curtius, J., Granzin, M., and Schrod, J. (2021). Testing mobile air purifiers in a school classroom: Reducing the airborne transmission risk for SARS-CoV-2. Aerosol Science and Technology 55 (5):586–599. doi:10.1080/02786826.2021.1877257.

Kelly, F.J. and Fussell, J.C. (2019). Improving indoor air quality, health and performance within environments where people live, travel, learn and work. Atmospheric Environment 200:90–109. doi:10.1016/j.atmosenv.2018.11.058.

Khalizov, A.F., Xue, H., Wang, L., Zheng, J., and Zhang, R. (2009). Enhanced Light Absorption and Scattering by Carbon Soot Aerosol Internally Mixed with Sulfuric Acid. J. Phys. Chem. A 113 (6):1066–1074. doi:10.1021/jp807531n.

Laskin, A., Laskin, J., and Nizkorodov, S.A. (2015). Chemistry of Atmospheric Brown Carbon. Chem. Rev. 115 (10):4335–4382. doi:10.1021/cr5006167.

Liu, D.T., Phillips, K.M., Speth, M.M., Besser, G., Mueller, C.A., and Sedaghat, A.R. (2022). Portable HEPA Purifiers to Eliminate Airborne SARS-CoV-2: A Systematic Review. Otolaryngology–Head and Neck Surgery 166 (4):615–622. doi:10.1177/01945998211022636.

McNamara, M.L., Thornburg, J., Semmens, E.O., Ward, T.J., and Noonan, C.W. (2017). Reducing indoor air pollutants with air filtration units in wood stove homes. Science of The Total Environment 592:488–494. doi:10.1016/j.scitotenv.2017.03.111.

Mikhailov, E.F., Vlasenko, S.S., Podgorny, I.A., Ramanathan, V., and Corrigan, C.E. (2006). Optical properties of soot–water drop agglomerates: An experimental study. J. Geophys. Res. Atmospheres 111 (D7). doi:10.1029/2005JD006389.

Pistochini, T. (2021), Considerations for use and selection of portable air cleaners for classrooms, *Rep.*, 3 pp, Western Cooling Efficiency Center, University of California, Davis, https://ucdavis.app.box.com/s/81yd5wsylxsc8oi2vtgf569vorph3tfk.

Ramanathan, V. and Carmichael, G. (2008). Global and regional climate changes due to black carbon. Nature Geoscience 1 (4):221–227. doi:10.1038/ngeo156.

Rodriguez-Navarro, C., di Lorenzo, F., and Elert, K. (2018). Mineralogy and physicochemical features of Saharan dust wet deposited in the Iberian Peninsula during an extreme red rain event. Atmospheric Chemistry and Physics 18 (13):10089–10122. doi:10.5194/acp-18-10089-2018.

Rosenthal, J. (2020), A variation on the "box fan with merv 13 filter" air cleaner, https://www.texairfilters.com/a-variation-on-the-box-fan-with-merv-13-filter-air-cleaner/, Accessed: 2 January 2022.

Seinfeld, J.H. and Pandis, S.N. (2016). Atmospheric Chemistry and Physics: From Air Pollution to Climate Change. John Wiley & Sons.

Shaughnessy, R.J. and Sextro, R.G. (2006). What Is an Effective Portable Air Cleaning Device? A Review. Journal of Occupational and Environmental Hygiene 3 (4):169–181. doi:10.1080/15459620600580129.

2 Characterizing the performance of a do-it-yourself (DIY) box fan air filter

This chapter has been published in Aerosol Science and Technology Dal Porto, R., Kunz, M. N., Pistochini, T., Corsi, R. L., & Cappa, C. D. (2022). Characterizing the performance of a do-it-yourself (DIY) box fan air filter. Aerosol Science and Technology, 56(6), 564–572. https://doi.org/10.1080/02786826.2022.2054674

2.1 Abstract

Air filtration serves to reduce concentrations of particles in indoor environments. Most standalone, also referred to as portable or in-room, air filtration systems use HEPA filters, and cost generally scales with the clean air delivery rate. A "do-it-yourself" lower-cost alternative, known as the Corsi-Rosenthal Box, that uses MERV-13 filters coupled with a box fan has been recently proposed, but lacks systematic performance characterization. We have characterized the performance of a five-panel Corsi-Rosenthal air cleaner using both research-grade instrumentation (an aerodynamic particle sizer, APS) and a low-cost particle sensor. Measurements of size-resolved and overall decay rates of aerosol particles larger than 0.5 microns emitted into rooms of varying size with and without the air cleaner allowed for determination of the apparent clean air delivery rate—both as a function of size and integrated across particle sizes for a number-weighted median particle diameter of 1.2 ± 0.12 microns. The measurements made in the different rooms produced similar results, demonstrating the robustness of the method used. The size-integrated effective clean air delivery rate increases with fan speed, from about 600 to 850 $ft^3\ min^{-1}$ (1019 to 1444 $m^3\ h^{-1}$) as determined with the APS. The low-cost sensor yields similar clean air delivery rates as the APS, demonstrating a method by which others who lack access to research-grade instruments can determine the effectiveness of Corsi-Rosenthal Boxes that use components that differ from those used here. Overall, our

results demonstrate that our Corsi-Rosenthal air cleaner efficiently reduces suspended particle concentrations in indoor environments.

2.2 Introduction

Filtration is a robust and widely used method to reduce particle concentrations in indoor environments (Curtius, Granzin and Schrod 2021; Kelly and Fussell 2019; McNamara et al. 2017; MillerLeiden et al. 1996). Particle filters can be embedded in ventilation systems or added as stand-alone, portable units within rooms (Alavy and Siegel 2020; Shaughnessy and Sextro 2006). Filters vary widely in their efficiency and are characterized by the minimum efficiency reporting value (MERV), with the highest efficiency filters referred to as high efficiency particulate air (HEPA) filters (ASHRAE 2017). Filter efficiency varies with particle size, and HEPA filters remove at least 99.97% of particles having diameters of 0.3 microns, which is typically where the minimum filter efficiency occurs. While ventilation systems rarely use HEPA filters, owing to the accompanying large pressure drop and space requirements, most commercial in-room filtration systems rely on HEPA filters (Shaughnessy and Sextro 2006). Various studies support the benefits of portable HEPA-based air cleaners for reducing aerosol concentrations from many sources, including reducing risks of COVID-19 transmission. For example, Liu et al. (2021) reviewed portable HEPA-based air cleaners and concluded that such air cleaners have "potential to eliminate airborne SARS-CoV-2 and augment primary decontamination strategies such as ventilation." Curtius, Granzin and Schrod (2021) reached similar conclusions based on measurements of aerosol concentration reductions in a classroom. Additionally, portable HEPA-based air cleaners have been shown to significantly reduce concentrations of traffic-related aerosol concentrations in homes close to highways (Cox et al. 2018), improve clinical manifestations for patients with allergic rhinitis by reducing particulate

matter and dust mite allergen concentrations in bedroom air (Luo et al. 2021), and reduce woodsmoke particles in wood-burning communities with measurable health benefits in relatively young and healthy subjects (Allen et al. 2011).

The cost of HEPA-based air cleaners generally scales with their capacity, usually characterized by their clean air delivery rate (CADR) (Association of Home Appliance Manufacturers (AHAM) 2014). The CADR determines the number of equivalent air changes per hour (ACH) achievable in a room of a given size. For example, the typical floor size of a U.S. classroom is about 1,000 ft^2 (93 m^2) and with a volume of about 8,000 ft^3 (227 m^3). To achieve three ACH in a room this size, for example, requires a CADR of 400 $ft^3\ min^{-1}$ (680 $m^3\ h^{-1}$). AHAM recommends that the CADR of an air filter is about two-thirds of the room floor area, corresponding to a CADR of 666 $ft^3\ min^{-1}$ for a 1,000 ft^2 classroom. In the context of airborne infectious disease transmission, the risk of long-range transmission continually decreases as the CADR increases (Shen et al. 2021). Limitations to in-room filtration include noise, energy consumption, and initial and maintenance costs for replacement filters. An initial cost-survey of commercially available Energy Star rated in-room filters (U.S.EPA 2021a) designed for the residential market found costs ranging from \$0.71 to \$2.66 per CADR in units of $ft^3\ min^{-1}$ (Pistochini 2021), making them inaccessible to many people and in many contexts.

A recently proposed, easy-to-construct, and low-cost alternative air filter constructed from MERV-13 filters and a box fan provides an opportunity for more people to access filter-based air cleaners in an affordable manner. This do-it-yourself (DIY) air filter, known as the "Corsi-Rosenthal Box" (hereafter, CR Box), is finding use in classrooms and other indoor environments across the U.S. through a grassroots movement driven by social media and the accessibility of the materials (Emanuel 2021). Although MERV-13 filters have a lower intrinsic filtration

efficiency than HEPA filters, in-room air filtration using MERV-13 filters will still lead to a reduction in particle concentrations. While some work on airflow optimization in the CR Box has been done (Elfstrom 2021) and some initial characterization exists (Srikrishna 2021; Wieingartner, Rüggeberg and Wipf 2021), no systematic evaluation of the performance yet exists. Given the adoption of the CR Box in classrooms and other indoor environments, such evaluation is critical.

Here, we characterize the Corsi-Rosenthal Box performance via measurement of size-dependent particle decay for particles >0.5 microns in a classroom and a home office with and without the CR Box operating. Our method allows for determination of CADR values above the 450 ft^3 min^{-1} (765 m^3 h^{-1}) upper-limit of the standard method (Association of Home Appliance Manufacturers (AHAM) 2014). We make measurements using both research-grade instrumentation (i.e., an aerodynamic particle sizer) and using a low-cost sensor to illustrate how such measurements can be made by those who lack access to research-grade instrumentation. We compare the results for the CR Box to those measured for two commercial HEPA-based air cleaners in terms of overall efficacy and cost.

2.3 Materials and Methods

Here, we provide an overview of the methods used, with full details in the Supplementary Material. Decay rates of salt particles introduced to two rooms—a furnished but not occupied 5926 ft^3 (168 m^3) classroom and a 1277 ft^3 (36.2 m^3) furnished but not occupied home office—were measured with and without the filter-based air cleaners turned on. The salt particles were generated using a portable mesh nebulizer (Wellue) using an aqueous table salt solution (50 g/L). A box fan oriented at the wall operated at low speed throughout the measurements to maintain similar turbulence and mixing conditions between experiments. The measurements with this

mixing fan on but the filter-based air cleaners turned off provides the baseline ventilation plus particle deposition rate, as these are the primary loss pathways for particles in a room. The measurements with the filter-based air cleaners turned on additionally include the influence of the filter. The equivalent air changes per hour (*ACH*) (actual air exchange + particle deposition to indoor surfaces + particle removal by an air cleaner) for each experiment were determined by fitting an exponential decay curve to the time-varying particle concentration ($C_{p,t}$) during the decay period with a y-offset that corresponds to the background particle concentration ($C_{p,bgd}$):

$$C_{p,t} = C_{p,bgd} + C_{p,t=0} \cdot \exp\left[-\frac{t}{\tau}\right] = C_{p,bgd} + C_{p,t=0} \cdot \exp[-ACH \cdot t] \quad (1)$$

where t is the time in hours, τ is the decay lifetime in hours, and $C_{p,t=0}$ is the concentration at the start of the decay period. Here, we consider both the particle number concentration (p cm^{-3}) and volume concentration (μm^3 cm^{-3}) for the C_p values, although focus on the number concentration measurements.

When the filter-based air cleaners are turned on there is additional turbulence induced by the air filter fan that could alter the baseline deposition rate above that with the mixing fan alone. To assess the influence of this added turbulence we conducted experiments using two fans, the mixing fan and an additional box fan set in the location of the air filter. These experiments indicated that the additional turbulence from the air filter fan increased the baseline natural ventilation rate by 17 ± 11% in the home office but only 3% ± 3% in the classroom (**Figure S2-1**). The difference results from the classroom having active ventilation and a substantially higher baseline *ACH* compared to the home office.

The *ACH* from filtration (*F*), ventilation (*V*), and deposition (*D*) add in series. Therefore, the equivalent *ACH* attributable to only the filter-based air cleaners (ACH_F) is simply the difference

between the value measured with the air filter on (ACH_{F+V+D}) and the baseline ACH from room ventilation and particle deposition (ACH_{V+D}):

$$ACH_F = ACH_{F+V+D} - ACH_{V+D} \quad (2)$$

The ACH_{V+D} values used in Eqn. 2 are taken as the values measured with the air filter off and the mixing fan operating, but adjusted upwards by 17% or 3% to account for additional turbulence from the air filter fan. Eqn. 2 can be used to determine the weighted-average equivalent ACH_F across all particle sizes (by fitting to the particle number or mass concentration) or for specific size ranges. The corresponding CADR is:

$$CADR = V_R \cdot ACH_F \quad (3)$$

where V_R is the room volume. We use $ACH_{X,Np}$ and $CADR_{Np}$ when referring to the value determined from the particle number concentration and $ACH_{X,Vp}$ and $CADR_{Vp}$ when determined from the volume concentration, and where X corresponds to F, V, or D (or combinations thereof). Particle concentrations and decay rates were measured at 5 s time resolution using an aerodynamic particle sizer (APS; TSI model 3321) and a low-cost sensor (LCS; Plantower PMS 5003). The APS characterizes particles into bins from 0.5-20 microns diameter according to their aerodynamic diameters (D_{pa}) and thus allows for determination of size-specific ACH values. Size-specific values are only considered up to D_{pa} = 5.425 □m as above this value the decays are too noisy to allow for robust fitting, owing to the very low concentrations of particles above this size. The APS yields both number and volume concentrations. Note that, unless otherwise stated, results are reported based on the APS measurements. The LCS converts light scattering observations to report size-dependent particle mass and particle number concentrations using an unknown algorithm with a nominal lower diameter limit of 0.3 microns. The reported number concentrations observed here exhibit linear decays (after natural log transformation), as

expected, whereas the mass concentrations from the LCS exhibit distinctly non-linear decays. We therefore consider only the number concentration data from the LCS and discourage the use of the reported mass concentrations in this context.

Three filter-based air cleaners were tested: the Corsi-Rosenthal Box and two commercial HEPA-based air cleaners. The Corsi-Rosenthal Box was originally proposed by Richard Corsi on Twitter and with Jim Rosenthal making the first prototype (Rosenthal 2020). The CR Box used here is constructed using three 20" x 20" x 2" and two 16" x 20" x 2" MERV-13 filters (Air Handler, LEED/Green Pleated Air Filter, total cost $34.75) and a 20" box fan (Air King Model 4CH71G, $23.68). (See **Figure S2-2** and the Supplemental Material for a full description and discussion of cost). The CR Box here sits on legs that hold it about 4" (10 cm) off the ground and with the fan pointed upwards or sideways. In one variation, we tested the CR Box inverted such that the fan pointed at the floor, sitting about 4" (10 cm) off the floor. An inverted CR Box would potentially be more robust against potential foreign objects being dropped into the fan. One of the HEPA-based air cleaners (HEPA #1) has a stated tobacco smoke CADR = 300 ft^3 min^{-1} (510 m^3 h^{-1}) when operated at maximum speed while the other (HEPA #2) has a stated tobacco smoke CADR = 141 ft^3 min^{-1} (240 m^3 h^{-1}) when operated at maximum speed.

The loudness of the filter-based air cleaners and of the box fan alone were measured using a decibel monitor (Extech Instruments HD600) that was situated 5 ft (1.52 m) from the center of the filter-based air cleaners and located perpendicular to the air exhaust. The power use by the filter-based air cleaners was measured using a power logger (Fluke 1735 Power Logger Analyst). The pressure drop for the CR Box was measured using a high-resolution pressure gauge (DG-700, TEC). Estimates of the fan airflow rate alone and as part of the CR box were estimated from air flow velocity measurements (see *Supplemental Material*).

2.4 Results and Discussion

Average particle size distributions are shown in **Figure 2-1a** for three periods: when particles were being actively produced, near the end of the natural decay, and near the end of the air filtration period. The number-weighted median particle aerodynamic diameter ($D_{pa,Np}$), as characterized by the aerodynamic particle sizer, averaged 1.2 ± 0.12 □m. The volume-weighted median particle aerodynamic diameter ($D_{pa,Vp}$) averaged 2.8 ± 0.5 □m. Both the $D_{pa,Np}$ and $D_{pa,Vp}$ generally decreased over the course of an experiment, with the $D_{pa,Np}$ starting at ~1.4 □m and decaying during both the natural decay period and, to a lesser extent, during the period when the filter-based air cleaners were turned on (**Figure 2-1b**). Technically, the *CADR* is defined relative to the size range for various particle types, specifically smoke (0.09-1 □m), dust (0.5-3 □m), and pollen (0.5-11 □m), and is measured in a sealed chamber of specific size (1008 ft^3). As such, the number-weighted *CADR* measured here are most representative of "dust" *CADR* values and the volume-weighted *CADR* of the "pollen" values. However, we note that the size-dependent *CADR* values overlap with all three particle types.

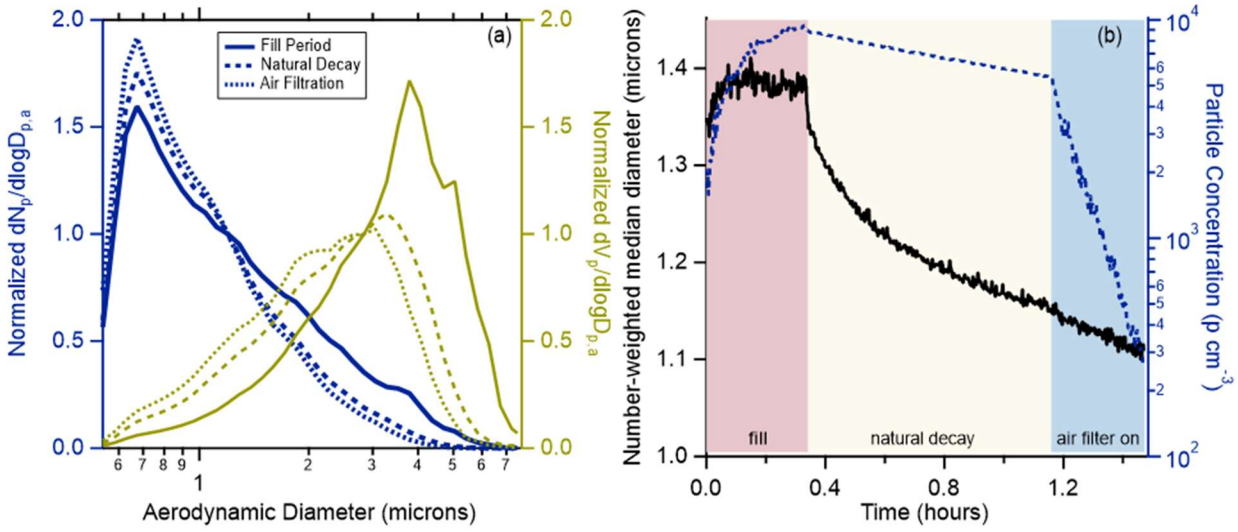

Figure 2-1. (a) Example number-weighted (left axis, blue) and volume weighted (right axis, gold) particle size distributions measured with the APS and shown for averages during the fill period with active particle production (solid line) period, near the end of the natural decay period (dashed line), and near the end of the active air filtration period (dotted line) for the home office. Number-weighted distributions are normalized to a diameter of 1.2 microns and volume weighted to 2.8 microns, corresponding to the number-weighted and volume-weighted median diameters, respectively. (b) Example results for one experiment in the home office showing the number-weighted median diameter (black solid line) and the particle number concentration (blue dashed line) across the fill period, natural decay period, and active air filtration period.

Example number-based particle decays from the APS measurements for the natural room ventilation and with the various air cleaners on are shown in **Figure 2-2**. The ACH_{V+D} was 3.5 ± 0.2 hr^{-1} (1□, precision-based uncertainty) for the unoccupied classroom and the ACH_{V+D} was 1.3 ± 0.1 h^{-1} for the unoccupied home office. **Figure 2-3** shows the resulting clean air delivery rates for air cleaners that were tested in both the classroom and home office, along with values for noise level and power draw (discussed further below). (Individual graphs for each parameter are provided in **Figure S2-4**.) Replicate *CADR* values for each air filter exhibited only small variations within each room and across the two rooms, although were generally larger for the measurements made in the classroom. The difference between the *ACH* values with and without the filter on was greater for the smaller home office (**Table 2-1**). Further, individual ACH_{V+D} values were determined for every air filter measurement in the home office but not the classroom (see Methods). Therefore, we take the *CADR* values determined from the home office as

generally more reliable and, unless otherwise stated, use them in the discussion that follows.

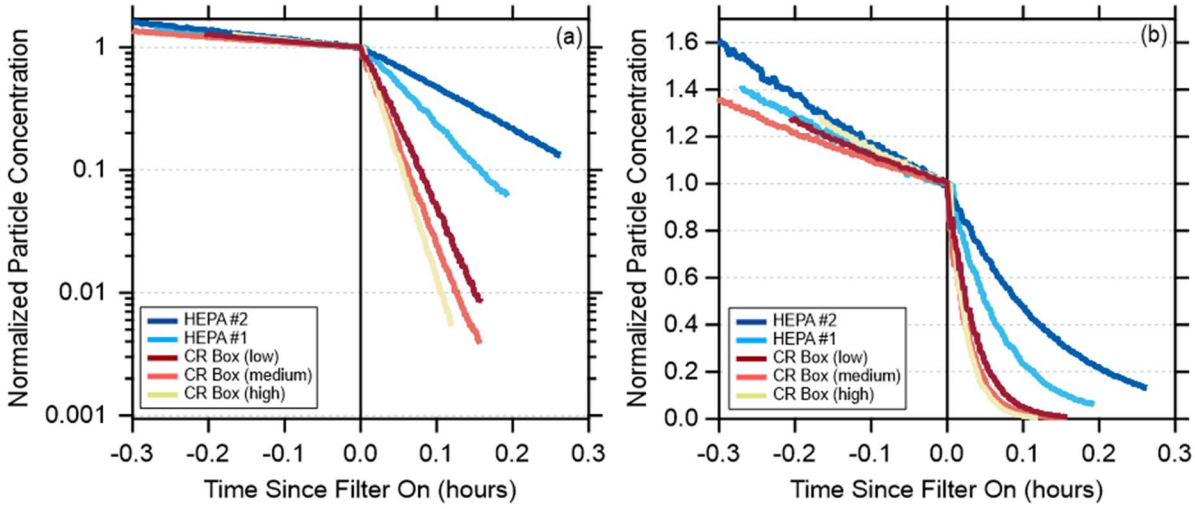

Figure 2-2. Example particle number decays measured in the home office for the natural ventilation + particle deposition (at t < 0) and with the filter-based air cleaners on (t > 0) shown on a (a) log scale and (b) linear scale. Particle concentrations have been normalized to unity at t = 0.

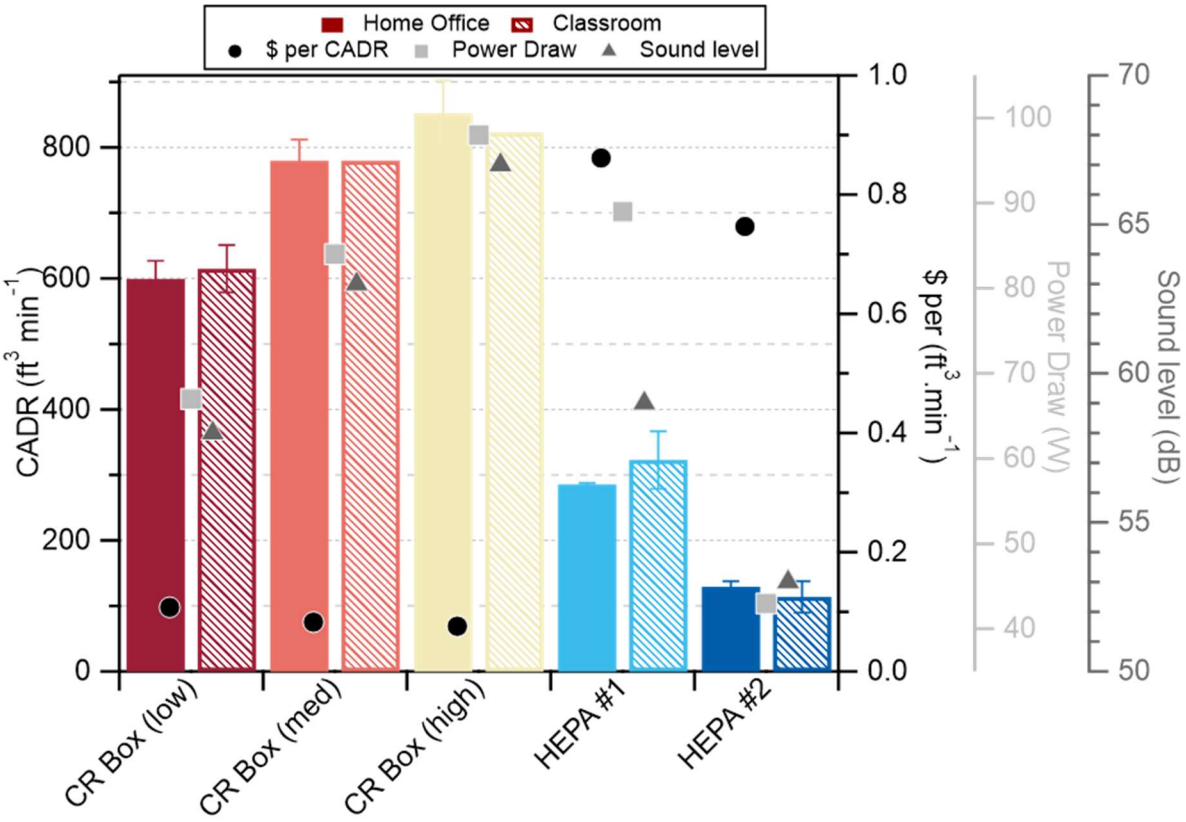

Figure 2-3. (left axis) The number-weighted clean air delivery rate for the various filter-based air cleaners (left axis, bars) as measured in the home office (left hash marks) and classroom (right hash marks). (right axis) The price normalized CADR (black circles), sound level (dark gray triangles), and power (light gray squares).

Table 2-1: Measured equivalent air changes per hour and clean air delivery rates.

Air Filter	ACH_{F+V+D} [#] (h^{-1})	$CADR_{Np}$ [*] (ft^3 min^{-1})	ACH_{F+V+D} [#] (h^{-1})	$CADR_{Np}$ [*] (ft^3 min^{-1})	$CADR_{Vp}$ [*] (ft^3 min^{-1})	Noise level (dB)	Power Draw (W)	$ per CADR
	Classroom		***Home office***					
None	3.5	--	1.3 ± 0.14	--		40		
CR Box (low)	9.8±0.4	614±36	29.6 ± 1.5	599 ± 27	614 ± 26	58 ± 2	67	0.11
CR Box (med)	11.4	780^	38.0 ± 0.1	780 ± 32	824 ± 32	63 ± 2	84	0.08
CR Box (high)	11.9	823^	41.5 ± 1.7	852 ± 50	903 ± 49	67 ± 1	98	0.08
HEPA #1	6.8±0.4	323±44	15.4 ± 0.5	285 ± 2	300 ± 2	59 ± 1	89	0.86
HEPA #2	4.7±0.3	114±24	7.9 ± 0.2	129 ± 8	118 ± 3	54 ± 1	43	0.74

[#]Based on number concentration measurement; not adjusted for additional turbulence

*****Calculated from individual pairs of ACH_{V+D} and adjusted ACH_{F+V+D} and so may not match with the CADR determined from the average ACH_{F+V+D}

[^]Only one measurement was made

Generally, the $CADR_{Vp} > CADR_{Np}$ with the exception of HEPA #2 (**Table 2-1**). The larger value for the $CADR_{Vp}$ results from the volume distribution being characterized by a larger median diameter compared to the number distribution and the filtration efficiency for MERV-13 filters increasing with size for particles in the APS measurement range (>0.5 microns). For HEPA #1 the $CADR_{Np}$ = 322 ± 44 ft^3 min^{-1} (547 ± 75 m^3 h^{-1}) for the classroom and 285 ± 2 ft^3

min^{-1} (484 ± 3.4 m^3 h^{-1}) for the home office, both in very good agreement with the manufacturer's specification of 300 ft^3 min^{-1} (510 m^3 h^{-1}). For HEPA #2 the $CADR_{Np}$ = 113 ± 24 ft^3 min^{-1} (192 ± 41 m^3 h^{-1}) for the classroom and $CADR_{Np}$ = 129 ± 8 ft^3 min^{-1} (219 ± 14 m^3 h^{-1}) for the home office, also in very good agreement with the manufacturer's specification of 141 ft^3 min^{-1} (240 m^3 h^{-1}). The good agreement between the measured $CADR_{Np}$ and the manufacturer's specifications provides a validation of the method.

The $CADR_{Np}$ for the Corsi-Rosenthal Box increases reasonably linearly with fan speed (**Figure S2-3**), from 600 ± 27 ft^3 min^{-1} (1020 ± 46 m^3 h^{-1}) at low speed to 779 ± 32 ft^3 min^{-1} (1324 ± 54 m^3 h^{-1}) at medium speed to 852 ± 50 ft^3 min^{-1} (1450 ± 85 m^3 h^{-1}) at high speed, as measured for the home office, and from 615 ± 36 ft^3 min^{-1} (1045 ± 61 m^3 h^{-1}) to 823 ft^3 min^{-1} (1400 m^3 h^{-1}) for the classroom. A linear fit with zero intercept to the $CADR_{Np}$ for the home office versus the fan total airflow rate estimates for the box fan at the three speeds indicates an effective filter efficiency of 41-58%, with the range indicating uncertainty in the CR Box airflow rates (see Supplementary Material; **Figure S2-3**). The air velocity measurements with the filters added indicated a 12% reduction in flow with a pressure drop (Dp) of 6.2 Pa at low speed. Accounting for this flow reduction increases the effective filter efficiency to 47-67%. The corresponding pressure drop at medium speed equaled 7.7 Pa and at high speed equaled 8.5 Pa. The $CADR_{Np}$ also varies linearly with the □p (**Figure S2-3**). The CADR increases by a greater amount going from low to medium speed than it does going from medium to high. Such behavior is consistent with the response of both the airflow rate and □p to changing the fan speed.

The size-dependent efficiency curves for the Air Handler MERV 13 filters indicates a minimum filtration efficiency (η_f) of ~55% for 0.35 micron diameter particles (D_p), which increases to ~85% for 0.75 micron diameter particles and to ~90% for 1 micron dimeter particles

(Air Handler via Grainger: 2022). Multiplying the observed particle size distribution by 1 - $\eta_f(D_p)$ and comparing with the original particle size distribution indicates an expected size-averaged filtration efficiency of about 87% by number and 93% by mass, larger than observed. This difference may result from a much lower air velocity across the five parallel filters in this study (<148 ft min^{-1} = 1.07 m s^{-1}) relative to those typically used for HVAC filter testing to determine MERV ratings (492 ft min^{-1} = 2.5 m s^{-1}) (ASHRAE 2017). For MERV-13 filters, inertial impaction and interception are the dominant loss mechanisms for the size range of particles considered here (Flagan 1988). For these mechanisms, the single-fiber collection efficiency for fibers in a filter bed increases with the Stokes number, and therefore face velocity, and depends on the particle-to-fiber diameter ratio and fiber packing density. The Stokes number for a 1 micron diameter particle having a density of 1 g cm^{-1} encountering a 5 micron diameter fiber, fairly typical of modern filters (Kowalski and Bahnfelth 2002; Kowalski, Bahnfelth and Whittam 1999), at a face velocity of 492 ft min^{-1} (2.5 m s^{-1}) equals 3.58, which is in the range over which the single-fiber filtration efficiency is particularly sensitive to changes in velocity (Flagan 1988). As such, a lower face velocity should mean lower removal efficiency due to the lessened effect of inertial impaction and interception. Alternatively, the reduced filtration efficiency measured in the experiment could also be attributed to leaks around the filter media, although the filter assembly was taped and visually inspected to seal any openings and thus we suspect that leaks play a minor role.

Size-dependent *ACH* and *CADR* values are determined by fitting decay curves to each particle size bin from the APS. The *ACH* for the natural room decay periods increase substantially with particle size (**Figure 2-4a**), likely due to higher particle deposition rates to indoor materials at larger aerodynamic diameters (Hussein and Kulmala 2008). The *ACH* for the

filter-based air cleaners also increase with particle size, but to a lesser extent than the natural room decay (**Figure 2-4a**). Consequently, the *CADR* for the filter-based air cleaners, which derive from the difference between the filter on and natural room decay *ACH* values, exhibit a weaker dependence on particle size compared to the *ACH* (**Figure 2-4b**). The *CADR* for the CR Box vary only weakly with particle size for all speeds and are relatively constant from about 0.7 to 2.5 microns (**Figure 2-4b**). This weak size dependence helps explain why the $CADR_{\mathrm{Vp}}$ values are only slightly larger than the $CADR_{\mathrm{Np}}$ values. However, such a weak size dependence is somewhat unexpected given the MERV-13 filter efficiency should increase sharply above 700 nm to about 1 micron, above which it should be constant and near unity. It is possible that the low face velocities on the filters relative to standard test conditions (ASHRAE 2017) led to atypical size dependence. Alternatively, additional turbulence from the filter exhaust air could have altered the particle deposition rates in the room from the baseline measurements leading to a flatter than expected size dependence, although the measurements with the added fan in place of the CR box suggest this had negligible influence. Notably, comparison of the size-specific *CADR* for particles with $D_{\mathrm{p,a}} > 1$ □m to the specified fan speeds indicates an η_f much less than unity, even after accounting for the 12% reduction in flow owing to filter resistance. The reason for this apparent lower than expected η_f for the CR Box is unclear.

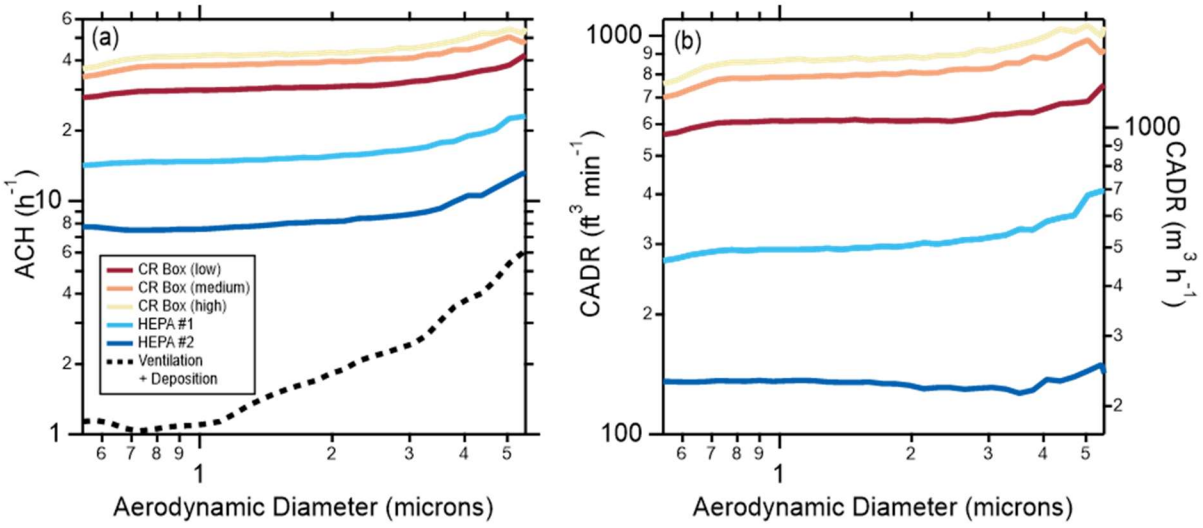

Figure 2-4. (a) Size-dependent equivalent air changes per hour with the various filter-based air cleaners operating (solid lines) and for the natural room ventilation + particle deposition alone (dashed line), as measured in the home office. (b) The corresponding clean air delivery rates for the various filter-based air cleaners. Results for the classroom are similar (not shown).

The CADR values for the Corsi-Rosenthal Box substantially exceed those of the particular commercial HEPA-based air cleaners used here (**Figure 2-3a**). For further comparison, no U.S. Energy Star certified air cleaners have CADR values (for either tobacco smoke, dust, or pollen) matching the CADR value for the CR Box even on low speed (**Figure S2-5**). Consideration of the cost-per-unit-air-cleaned for the low-speed CR Box (<\$0.072/(ft^3 min^{-1})) and for the two HEPA-based air cleaners (>\$0.7/(ft^3 min^{-1})) demonstrates that the DIY air filter is approximately one-tenth the initial cost of a commercially available HEPA-based air cleaners per unit of air cleaned (**Figure 2-3**).

The CR Box loudness varied from 58 dB (low speed) to 67 dB (high speed) (**Figure 2-3**; **Table 2-1**). The low speed loudness is similar to that measured for HEPA #1 (59 dB) but higher than

that for HEPA #2 (54 dB). For reference, a modern refrigerator has a noise rating of about 50 dB and a LEED certified vacuum must be <70 dB. To attain a CADR equivalent to the CR Box on low speed would require about two HEPA #1 units and 4 HEPA #2 units, which would yield 62 dB and 60 dB, respectively. The power draw for the CR Box varied from 67 W (low speed) to 98 W (high speed) and was 89 W for HEPA #1 and 43 W for HEPA #2, corresponding to 8.9 and 8.7 $ft^3\ min^{-1}.W^{-1}$ (15.1 and 14.8 $m^3\ h^{-1}.W^{-1}$) for the CR Box and 3.2 and 3.0 $ft^3\ min^{-1}.W^{-1}$ (5.4 and 5.1 $m^3\ h^{-1}.W^{-1}$) for the HEPA-based air cleaners. For comparison, the most efficient category of U.S. Energy Star certified portable air cleaners must have an efficiency equal or greater than 2.9 $ft^3\ min^{-1}.W^{-1}$ (4.9 $m^3\ h^{-1}.W^{-1}$, meaning the CR Box is three times more efficient than the Energy Star standard (U.S.EPA 2021b).

The *CADR* values for the inverted CR Box were all suppressed relative to the standard CR Box orientation (with the fan pointed upwards; **Table S1**). For example, in the inverted orientation the $CADR_{Np}$ = 481 $ft^3\ min^{-1}$ (817 $m^3\ h^{-1}$) on the low setting, compared to ~600 $ft^3\ min^{-1}$ (1019 $m^3\ h^{-1}$) in the standard orientation. This difference likely resulted from one or both of (i) short circuiting of the airflow wherein clean air exhausted by the fan is preferentially entrained into CR Box filters rather than being dispersed into the broader room, or (ii) increased shear forces that resuspended particles previously deposited on the floor and increase particle number concentrations in air. Therefore, we suggest that orienting a CR Box (or likely any air filter) such that the fan exhaust is towards the floor be avoided.

In addition to the measurements with the APS, we also characterized the CADR for the various air cleaners using a low-cost sensor. Such low-cost sensors are much more accessible to the public than research grade instrumentation, such as an APS. The CADR measurements made with the low-cost sensor yield generally similar results to those made with the APS (**Figure**

S2-6), with the $CADR_{Np}$ increasing with fan speed for the CR Box and with values for the HEPA-based air cleaners similar to the manufacturer's specification. However, the specific $CADR_{Np}$ depended on which reported particle size regime was used for the fitting. Such a result is somewhat surprising given that the low-cost sensor is not fundamentally a particle counting measurement, but instead derives particle number from the measured light scattering. The root-mean square difference between the low-cost sensor and APS $CADR_{Np}$ values was smallest for the $N_{p,>1.0}$ bin (72 ft^3 min^{-1}), marginally larger for the $N_{p,>0.5}$ (76 ft^3 min^{-1}) and $N_{p,>0.3}$ (78 ft^3 min^{-1}) bins, and substantially larger for the $N_{p,>2.5}$ (161 ft^3 min^{-1}) and $N_{p,>5.0}$ (220 ft^3 min^{-1}) bins. Without further knowledge of the algorithm behind the low-cost sensor data processing we cannot establish the origin of this apparent size dependence or why the $N_{p,>1.0}$ bin yields the most similar values. Nonetheless, our results suggest that the use of low-cost sensors can yield a reasonable measure of the relative *CADR* values between filter-based air cleaners and a reasonable estimate of the absolute *CADR* values, and thus a means by which those without access to expensive instrumentation can determine the efficacy of DIY filter-based air cleaners. This is particularly important as different combinations of fans and filters (e.g., filter size or MERV rating) may yield results that differ from those presented here. We note that preliminary results for a CR Box using the same filters but a different fan (Lasko, Model B20301) indicate a lower range of *CADR* values than reported here for the CR Box with the Air King fan.

2.5 Summary

We have measured the filtration efficiency for particles >0.5 microns of a DIY, open-source air filtration system, the Corsi-Rosenthal Box, comprised of a box fan and MERV-13 filters. At the lowest speed the clean air delivery rate for our Corsi-Rosenthal Box is >600 ft^3 min^{-1} (1019 m^3 h^{-1}) for a median particle diameter of 1.2 microns, demonstrating exceptional performance

relative to most commercially available filter-based air cleaners. The CADR increases with fan speed, with the highest value about 850 $ft^3\ min^{-1}$ (1444 $m^3\ h^{-1}$) for these particle sizes. However, the filter noise level also increases with fan speed, from 58 dB at low speed to 67 dB at high speed. The CR Box is cost efficient, with a cost-normalized CADR of <\$0.072/($ft^3\ min^{-1}$). We also demonstrate good agreement between results obtained using research-grade instrumentation and a low-cost sensor, which provides a methodology by which others can characterize the performance of other DIY air filtration systems. Future efforts to improve and characterize the CR Box might focus on decreasing the CR Box noise level without compromising filtration performance, characterizing the effectiveness for smaller particle sizes, or characterizing different CR Box designs that use different fans and filters or different numbers of filters, which may yield results that differ from those shown here.

2.6 Acknowledgements

The authors greatly appreciate the contributions from students in ECI/ATM 149 at UC Davis, who performed some preliminary experiments as part of a lab activity. Jim Rosenthal is thanked for constructing and promoting the first Corsi-Rosenthal box.

Author contributions:.RDP, MNK, TP, and CDC made measurements; RDP and CDC analyzed data; all authors interpreted results; RC designed the DIY air filter; CDC and RDP led the writing with contributions from all authors.

Competing interests: The authors declare no competing interests.

Data and materials availability: All data needed to evaluate the conclusions in the paper are present in the paper and/or the supplementary materials.

2.7 Funding

N/A

2.8 References

Air Handler via Grainger: (2022), Green pleat merv 13, https://www.grainger.com/ec/pdf/Air-Handler-Green-Pleat-Merv-13-Air-Filters-Guide.pdf, Accessed: 2 January 2022.

Alavy, M. and J. A. Siegel. 2020. In-situ effectiveness of residential hvac filters. *Indoor Air* 30:156-166. doi: 10.1111/ina.12617.

Allen, R. W., C. Carlsten, B. Karlen, S. Leckie, S. van Eeden, S. Vedal, I. Wong, M. Brauer. 2011. An air filter intervention study of endothelial function among healthy adults in a woodsmoke-impacted community. *American Journal of Respiratory and Critical Care Medicine* 183:1222-1230. doi: 10.1164/rccm.201010-1572OC.

ASHRAE. 2017. Standard 52.2: Method of testing general ventilation air-cleaning devices for removal efficiency by particle size. Atlanta, GA.

Association of Home Appliance Manufacturers (AHAM). 2014. Ansi/aham ac-1: Method for measuring the performance of portable household electric room air cleaners. Washington, DC.

Cox, J., K. Isiugo, P. Ryan, S. A. Grinshpun, M. Yermakov, C. Desmond, R. Jandarov, S. Vesper, J. Ross, S. Chillrud, K. Dannemiller, T. Reponen. 2018. Effectiveness of a portable air cleaner in removing aerosol particles in homes close to highways. *Indoor Air* 28:818-827. doi: 10.1111/ina.12502.

Curtius, J., M. Granzin, J. Schrod. 2021. Testing mobile air purifiers in a school classroom: Reducing the airborne transmission risk for sars-cov-2. *Aerosol Science and Technology* 55:586-599. doi: 10.1080/02786826.2021.1877257.

Elfstrom, D. (2021), by @DavidElfstrom, Title, Posted on: 15 August 2021, https://twitter.com/DavidElfstrom/status/1427112878616817669.

Emanuel, G. (2021), Does your kid's classroom need an air purifier? Here's how you can make one yourself, NPR, Published on: 26 August 2021, https://www.npr.org/sections/back-to-school-live-updates/2021/08/26/1031018250/does-your-kids-classroom-need-an-air-purifier-heres-how-you-can-make-one-yoursel.

Flagan, R. C. 1988. *Fundamentals of air pollution engineering*. Englewood Cliffs, N.J.: Prentice-Hall.

Hussein, T. and M. Kulmala. 2008. Indoor aerosol modeling: Basic principles and practical applications. *Water, Air, & Soil Pollution: Focus* 8:23-34. doi: 10.1007/s11267-007-9134-x.

Kelly, F. J. and J. C. Fussell. 2019. Improving indoor air quality, health and performance within environments where people live, travel, learn and work. *Atmospheric Environment* 200:90-109. doi: 10.1016/j.atmosenv.2018.11.058.

Kowalski, W. J. and W. P. Bahnfelth (2002), Merv filter models for aerobiological applications, https://www.nafahq.org/merv-filter-models/, Accessed: 2 January 2022.

Kowalski, W. J., W. P. Bahnfelth, T. S. Whittam. 1999. Filtration of airborne microorganisms: Modeling and prediction. *ASHRAE Transactions: Research* 105:4-17. doi.

Liu, D. T., K. M. Phillips, M. M. Speth, G. Besser, C. A. Mueller, A. R. Sedaghat. 2021. Portable hepa purifiers to eliminate airborne sars-cov-2: A systematic review. *Otolaryngol. Head Neck Surg.*:8. doi: 10.1177/01945998211022636.

Luo, J. Y., L. L. Ou, J. Ma, X. Y. Lin, L. M. Fan, H. C. Liu, B. Q. Sun. 2021. Efficacy of air purifier therapy for patients with allergic asthma. *Allergol. Immunopath.* 49:16-24. doi: 10.15586/aei.v49i5.146.

McNamara, M. L., J. Thornburg, E. O. Semmens, T. J. Ward, C. W. Noonan. 2017. Reducing indoor air pollutants with air filtration units in wood stove homes. *Science of the Total Environment* 592:488-494. doi: 10.1016/j.scitotenv.2017.03.111.

MillerLeiden, S., C. Lobascio, W. W. Nazaroff, J. M. Macher. 1996. Effectiveness of in-room air filtration and dilution ventilation for tuberculosis infection control. *Journal of the Air & Waste Management Association* 46:869-882. doi: 10.1080/10473289.1996.10467523.

Pistochini, T. (2021), Considerations for use and selection of portable air cleaners for classrooms, *Rep.*, 3 pp, Western Cooling Efficiency Center, University of California, Davis, https://ucdavis.app.box.com/s/81yd5wsylxsc8oi2vtgf569vorph3tfk.

Rosenthal, J. (2020), A variation on the "box fan with merv 13 filter" air cleaner, https://www.texairfilters.com/a-variation-on-the-box-fan-with-merv-13-filter-air-cleaner/, Accessed: 2 January 2022.

Shaughnessy, R. J. and R. G. Sextro. 2006. What is an effective portable air cleaning device? A review. *Journal of Occupational and Environmental Hygiene* 3:169-181. doi: 10.1080/15459620600580129.

Shen, J. L., M. Kong, B. Dong, M. J. Birnkrant, J. S. Zhang. 2021. Airborne transmission of sars-cov-2 in indoor environments: A comprehensive review. *Sci. Technol. Built Environ.* 27:1331-1367. doi: 10.1080/23744731.2021.1977693.

Srikrishna, D. 2021. Price-performance comparison of hepa air purifiers and lower-cost merv 13/14 filters with box fans for filtering out sars-cov-2 and other particulate aerosols in indoor community settings. *preprint on medRxiv*. doi: 10.1101/2021.12.04.21267300.

Taber, C. and M. Ivanovich. 2018. New federal regulations for ceiling fans. *ASHRAE Journal* 60:42-46. doi.

U.S.EPA (2021a), Energy star certified air purifiers (cleaners), https://www.energystar.gov/productfinder/product/certified-room-air-cleaners/results, Accessed: 29 December 2021.

U.S.EPA (2021b), Energy star product specifications for room air cleaners: Eligibility criteria version 2.0, https://www.energystar.gov/sites/default/files/ENERGY%20STAR%20Version%202.0%20Final%20Room%20Air%20Cleaners%20Program%20Requirements_0.pdf, Accessed: 29 December 2021.

Wieingartner, E., T. Rüggeberg, M. Wipf (2021), Measurement of the filtration performance of diy air cleaners (cadr values) for aerosol particles with diameters smaller than 1 micrometer., *Rep.*, 13 pp, University of Applied Sciences Northwestern Switzerland,

https://makehumantechnology.org/wp-content/uploads/2021/10/Messbericht_DIY_Air_Cleaner_2021-10-8-EN.pdf.

2.9 Supplemental Materials for: Characterizing the performance of a DIY air filter

The supplemental materials contains:

- A fuller description of the materials and methods
- Tables S1-S2
- Figures S1-S6

2.9.1 Materials and Methods

2.9.1.1 Particle Generation and Measurement

Our overall approach to determining equivalent air changes per hour, either with or without added air filtration, generally follows from the measurement of decay rates of particles introduced into rooms at concentrations well above background. Particles were generated using portable mesh nebulizers (Wellue®) filled with an aqueous solution of table salt (100 g L^{-1}). The nebulizers were operated on their maximum setting (0.9 ml min^{-1}) and up to two were used per room. A representative particle size distribution is shown in *Figure 2-1*. A box fan was turned on its low setting and positioned about 0.5 m from one wall of the room, pointing at the wall, to induce mixing in the room, ideally leading to a reasonably well-mixed condition.

Although a similar approach was taken for measurements made in the classroom and the home office, the experimental details differed slightly. For the classroom, experiments began with measurement of the background particle concentration with all doors to the room closed. Following the background measurement the nebulizer was turned on with the filter-based air cleaners turned off. The nebulizer automatically shut off after ~10 minutes at which point the filter-based air cleaners were turned on. Particle measurements continued for an additional ~30 minutes during which the particle decay was measured. The first experiment was conducted with the CR Box turned off to determine the baseline effective room air exchange rate owing to the

ventilation or natural infiltration or particle deposition to surfaces. Subsequent experiments had the CR Box turned on to either the low, medium, or high setting or the HEPA filters turned on to their highest setting. For the classroom, two replicate measurements were made for each of the HEPA filters and for the CR Box on low speed, but only one measurement each was made for the CR box at medium and high speed. For the home office the protocol differed slightly. Specifically, following the background particle measurement and subsequent particle generation the decay from natural ventilation/infiltration plus deposition was measured for ~20 minutes. At this point the air filter of interest was turned on and the decay with the air filter on was measured for ~15 minutes. This allowed for determination of a unique baseline air changes per hour for every filter measurement resulting from passive or active ventilation and particle deposition to surfaces. For the CR Box three replicate measurements at each speed were made, while only two replicates were made for the commercial HEPA filters in the home office.

The air exchange rate was determined by fitting an exponential decay curve to the particle concentration (C_p) with a y-offset corresponding to the background concentration ($C_{p,bgd}$) period starting approximately one minute after the nebulizer stopped, where:

$$C_{p,t} = C_{p,bgd} + C_{p,t=0} \cdot \exp\left[-\frac{t}{\tau}\right] = C_{p,bgd} + C_{p,t=0} \cdot \exp[-ACH \cdot t] \quad \text{(S1)}$$

where t is the time in hours, τ is the decay lifetime, and $C_{p,t=0}$ is the particle concentration at the start of the decay period. The value for $C_{p,t=0}$ depends on the particle source rate relative to the overall air exchange rate. The particle background concentration depends on the particle concentration in the exchanged air from outside the room and in-room sources besides the nebulizer. In our experiments, the background particle concentrations were sufficiently small that we could assume $C_{p,bgd} = 0$ as opposed to a free-fit with the derived ACH values differing by less than 1%. The ACH attributable to only the CR Box (ACH_F) is simply the difference between the

value measured with the CR Box on and the baseline ACH from room ventilation and particle deposition (that is, with the filter off, ACH_{V+D}), as these add in series.

$$ACH_F = ACH_{F+V+D} - ACH_{V+D} \quad \text{(S2)}$$

The robustness of the fits from Eqn. 1 were verified via linear fitting to the natural log transformed and background-subtracted particle concentration data. Eqn. 1 can be used to determine the weighted-average ACH_F across all particle sizes (by fitting to the particle number or mass concentration) or for specific size ranges. The corresponding CADR is:

$$CADR = V_R \cdot ACH_F \quad (3)$$

where V_R is the room volume, and with appropriate unit conversion. We use $ACH_{X,Np}$ and $CADR_{Np}$ when referring to the value determined from the particle number concentration and $ACH_{X,Mp}$ and $CADR_{Mp}$ when determined from the mass concentration, and where X corresponds to $V+D$ (natural room ventilation and deposition only), F (filter only), or $F+V+D$ (filter + natural room ventilation + deposition).

The influence of additional turbulence induced by the fan in the CR Box on particle deposition to surfaces was also assessed for the classroom and the home office. In both, a single fan, oriented towards a wall, was first turned on similar to the filtration experiments above. The nebulizer was then started and particles were produced for about 10 minutes and the concentration of particles in the room increased. Once the nebulizer stopped the particle concentration in the room was allowed to decay for 10-20 minutes with just the single fan operating. Then, a second fan with no filters attached was started and the particle decay was measured for an additional 20-30 minutes. This second fan was placed in the same position and with the same orientation as the fan in the CR Box. Example decays are shown in Figure S2-1.

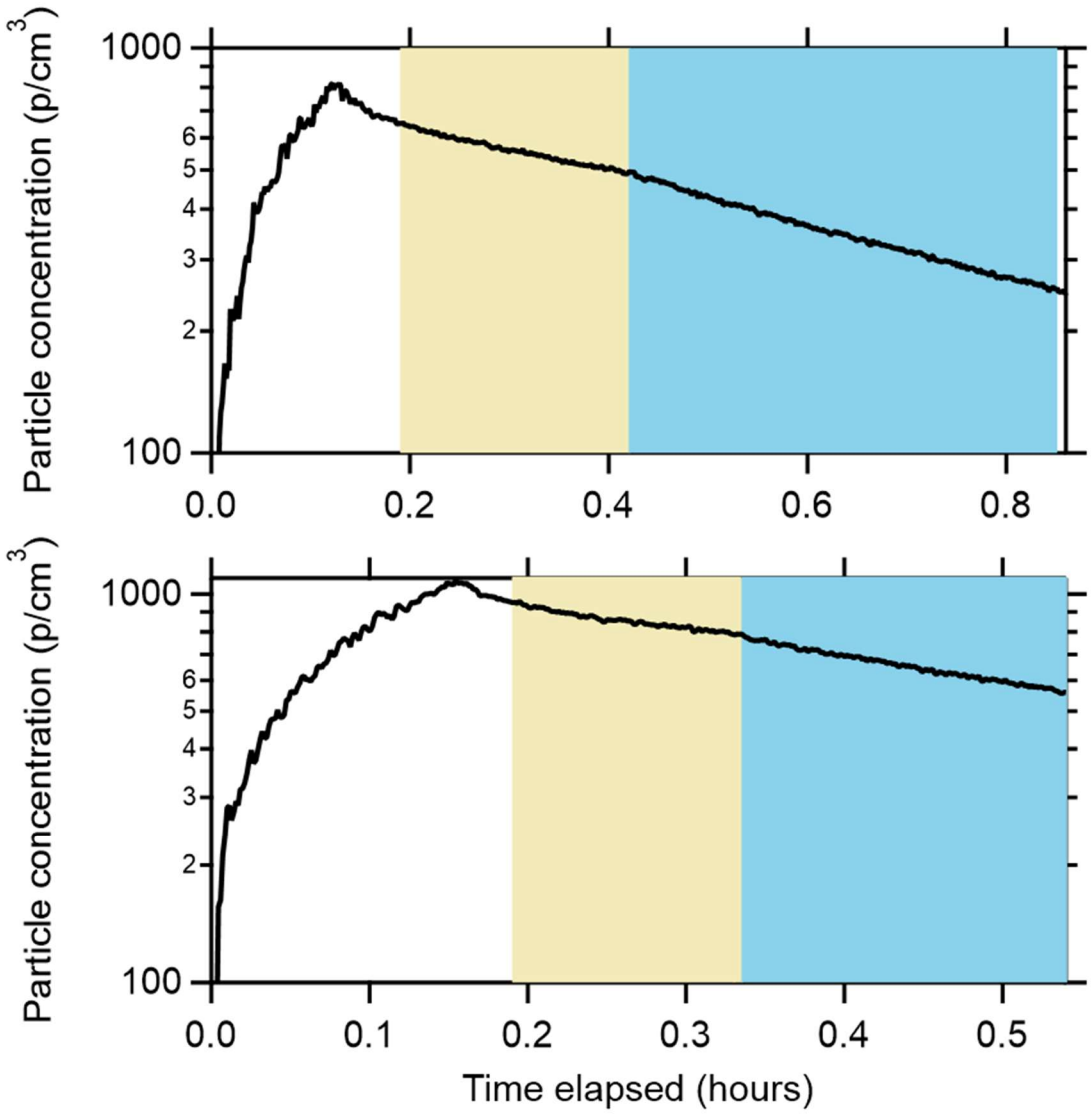

Figure S2-1. Particle decay with one fan (yellow) and with two fans (blue) for the home office (top) and classroom (bottom).

Particle concentrations and decay rates were measured using two independent methods. An aerodynamic particle sizer (APS; TSI model 3321) characterized particles having aerodynamic diameters from 0.5-20 microns with 5-second time resolution. The APS characterizes particles into bins according to their aerodynamic diameters (D_{pa}) and thus allows

for determination of size-specific *ACH* values. Size-specific values are only considered up to D_{pa} = 5.425 □m as above this value the decays are too noisy to allow for robust fitting. The APS is a well-established research-grade instrument for the characterization of particle concentrations and size distributions. As such, we use the measurements made with the APS for the main analysis in the main text.

A low-cost Plantower sensor (PMS 5003) characterized particles having optical diameters above about 0.3 microns with 5-second time resolution. Particle concentrations from the Plantower sensor were logged to an SD card using an Arduino METRO microcontroller with a Hi-LetGo data logging shield.[1] Temperature and relative humidity measurements measured using an Si7021 sensor (Adafruit) were also logged. The Plantower sensor converts and reports observations of scattering to size-dependent particle mass and particle number using an algorithm that is unknown. Also unknown is the relationship between particle number and mass concentration. The reported number concentrations observed here exhibit linear decays (after natural log transformation) whereas the mass concentrations exhibit distinctly non-linear decays. The reason for this is unclear, as one would expect that the number concentration and mass concentrations are related through a simple linear transformation for this type of instrument. Regardless of reason, since the number concentration measurements exhibit a linear decay, similar to the APS, we consider only the number concentration data from the Plantower sensor.

[1] For those who have interest in constructing their own low-cost sensor using a plantower sensor, there are a variety of resources available on the internet to get started. We also provide some basic documentation and code, as used in the ECI 149 class at UC Davis, that can be downloaded from https://ucdavis.box.com/s/pswqa1hr62ed4vvbzxmxw0ua39u3rr3f. Per the terms of the code from which we have borrowed, "the software is provided "as is", without warranty of any kind, express or implied, including but not limited to the warranties of merchantability, fitness for a particular purpose and noninfringement. In no event shall the authors or copyright holders be liable for any claim, damages or other liability, whether in an action of contract, tort or otherwise, arising from, out of or in connection with the software or the use or other dealings in the software."

2.9.1.2 Filter-based Air Cleaners

Three filter-based air cleaners were tested: the Corsi-Rosenthal Box and two commercial HEPA filters.

2.9.1.3 The Corsi-Rosenthal Box

The Corsi-Rosenthal Box was originally proposed by Rich Corsi on Twitter and with Jim Rosenthal making the first prototype (Rosenthal 2020). The CR Box used here is constructed using three 20” x 20” x 2” and two 16” x 20” x 2” MERV-13 filters (Air Handler, LEED/Green Pleated Air Filter, total cost $34.75) and a 20” box fan (Air King Model 4CH71G (9723), $23.68). The assembled Corsi-Rosenthal Box is shown in Figure S2-2. We note that the cost of the filters here was about half that from many vendors, possible owing to purchasing agreements between UC Davis and specific vendors. In a non-comprehensive internet search conducted on 21 November 2021 we found that the average price for a MERV-13 20” x 20” x 2” filter averaged $13.19 ± $2.22 and for a 16” x 20” x 2” filter averaged $15.39 ± $3.96, corresponding to a total cost of $70.36. Similarly, the particular Air King fan used here retails for about twice our purchase price when not on sale. Two of the 16” x 20” and two of the 20” x 20” filters are used to construct the side walls that sit on the 20” x 20” filter. The box fan is attached to the top and the seams are sealed with duct tape ($6). The box fan is oriented such that the fan blows out of the constructed filter box. This creates a slight negative pressure that may help to seal the box and limit leaks, although any persistent leaks from e.g., holes in the filters or the tape would be independent of the flow direction. The box fan includes a ~circular “shroud” that covers the box fan corners and prevents backflow of unfiltered air into the fan. (The use of a shroud was proposed for square box fans by David Elfstrom on Twitter (Elfstrom 2021).) Here the diameter of the open shroud is 17”. The CR Box sits on legs that hold it about 4” (10 cm) off the ground

and with the fan pointed upwards or sideways. In one variation, we tested the CR Box inverted such that the fan pointed at the floor, sitting about 4" (10 cm) off the floor. An inverted CR Box would potentially be more robust against potential foreign objects being dropped into the fan.

Figure S2-2. A photo of the assembled Corsi-Rosenthal Box.

2.9.1.4 *Commercial HEPA filters*

Two commercial HEPA filters were tested. One (HEPA #1) has a stated tobacco smoke CADR = 300 ft^3 min^{-1} (508 m^3 h^{-1}) when operated at maximum speed and includes two prefilters to capture larger particles and reduce volatile organic compounds, and a HEPA filter. It retails for about $250. The other (HEPA #2) has a stated tobacco smoke CADR = 141 ft^3 min^{-1} (240 m^3 h^{-1}) when operated at maximum speed, includes an activated carbon prefilter, and a noise level of 50 dB as specified by the manufacturer. It retails for about $100.

2.9.2 Measurement Environment

Measurements were made initially in three environments: (i) a 5926 ft^3 (167.8 m^3) classroom in Ghausi Hall at UC Davis; (ii) a 2890 ft^3 (81.8 m^3) office/meeting space in Ghausi Hall; and (iii) a 1277 ft^3 (36.2 m^3) home office in a residential building dating to 1923. For the home office the HVAC system was kept off throughout the measurements and thus the natural decay depended only on infiltration/exfiltration rates and particle deposition. Ultimately, only two of these environments were considered (the classroom and the home office) because the ventilation rates were sufficiently constant. In the office/meeting space the ventilation rate reduced when the occupancy sensors detected no movement for 15 minutes and shut off airflow after an additional 15 minutes of no movement. The ventilation rate in this room was too variable to allow for robust determination of the filter-specific *ACH* values. The smaller size of the home office compared to the classroom led to a greater difference in the *ACH* values measured with an air filter on versus with it off.

2.9.3 Fan Speed & Measurement

The fan has a manufacturer specified air flowrate of 1463, 1900, and 2163 $ft^3\ min^{-1}$ (2486, 3228, 3675 $m^3\ h^{-1}$) for low, medium, and high settings, respectively, tested under AMCA 230-99, which tends to overestimate fan speeds by 30% (Taber and Ivanovich 2018), although it is questionable how well this applies to box fans as the AMCA 230-99 method was developed for ceiling fans. Regardless, a 30% reduction corresponds to reduced air flowrates of 1024, 1330, and 1514 $ft^3\ min^{-1}$ (1740, 2260, 2572 $m^3\ h^{-1}$). The face velocities on the five filters (area ~ 10.25 ft^2 or 0.95 m^2) are 143, 185, and 211 ft min^{-1} (0.75, 0.94, 1.07 m s^{-1}) using the manufacturer's values and 100, 130, and 148 ft min^{-1} (0.51, 0.66, 0.75 m s^{-1}) using the reduced values. However,

taping the corners of the box fans can also lead to an increase in the air flow rate through the filters as it reduces the potential for back flow.

To assess these estimates, we measured the air velocity in feet per minute using a Veloci Calc Model 9555-P. Measurements were made at six radial positions approximately equidistant from each other, starting at the center of the fan, moving to the outer edge. These six positions were measured at the mid-point of each edge of the fan. Measurements were first taken with the fan as purchased, with no modifications, at both high and low speeds. Then, the corners of the fan were taped, and a measurement at low speed was taken with no filters and with 5 filters in the Corsi-Rosenthal Box configuration. The face velocity was integrated over the 24 measurements and their distance from the center. Average face velocities for the unaltered fan at high speed were 880 ft min^{-1} (268 m min^{-1}), 650 ft min^{-1} (198 m min^{-1}) for the unaltered fan on low speed, 668 ft min^{-1} (204 m min^{-1}) for the fan on low speed with taped edges, and 578 ft min^{-1} (176 m min^{-1}) for the Corsi-Rosenthal on low speed. Multiplying by the fan area but without accounting for the area taken up by the fan protective grate, these equate to air flowrates of 1800 ft^3 min^{-1} (3058 m^3 h^{-1}) for the high velocity fan with no modifications, 1331 ft^3 min^{-1} (2261 m^3 h^{-1}) for the low setting with no modifications, 1361 ft^3 min^{-1} (2312 m^3 h^{-1}) for the low setting with the fan edges taped, and 1171 ft^3 min^{-1} (1990 m^3 h^{-1}) for the low speed in CR configuration. Accounting for the protective grate area would increase these slightly. These values for the unadulterated fan are in between the reported and reduced manufacturers' specified values, but within the likely uncertainties. The fan flow rate in the CR Box configuration with the fan edges taped is reduced by only 12% from the unaltered fan.

2.9.4 *Loudness & Current Measurement*

The loudness of the filter-based air cleaners was measured using a decibel monitor that was situated 5 ft (= 1.52 m) from the center of the filter-based air cleaners and located perpendicular to the air exhaust. The background room noise level was 40 dB. Measurements were also made for the box fan separate from the filters. The power draw by the filter-based air cleaners were measured using a Fluke power meter. Because dB is a logarithmic scale, noise levels (L) must be added after log transformation as:

$$L = 10 \cdot \log\left(\sum_{i=1}^{n} 10^{\frac{L_i}{10}}\right)$$

2.9.5 Supplementary Tables

Table S1: Measured clean air delivery rates (ft^3 min^{-1}) for the Corsi-Rosenthal Box in the inverted orientation

Air Filter	***CADR*$_{Np}$** (ft^3 min^{-1})	***CADR*$_{Mp}$** (ft^3 min^{-1})
CR Box (low)	481	489
CR Box (med)	728	763
CR Box (high)	809	854

2.9.6 Additional Supplementary Figures

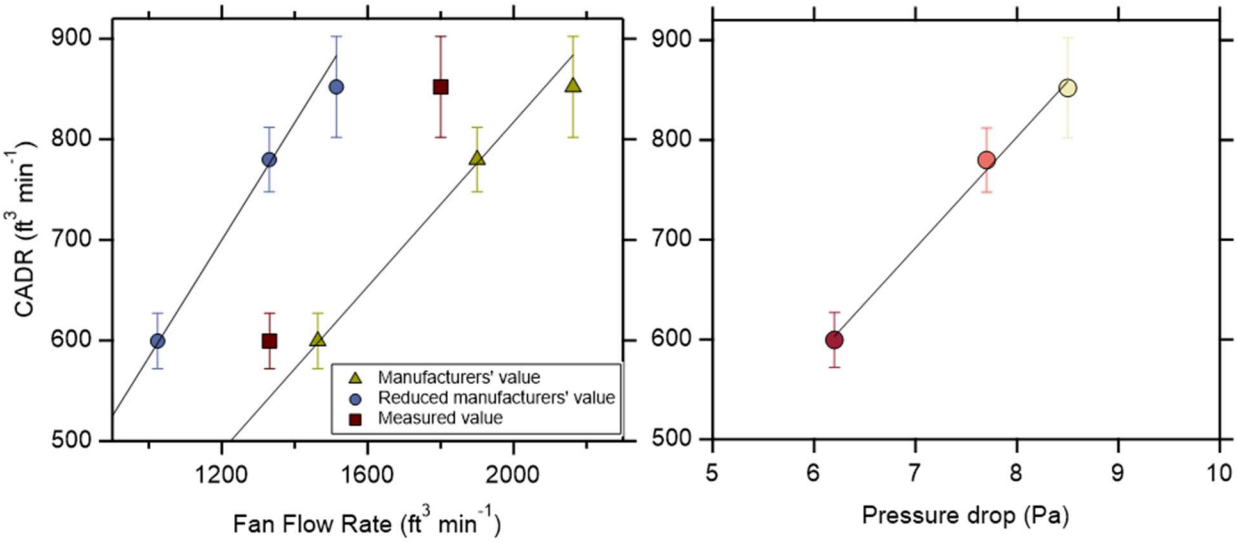

Figure S2-3. (left) Relationship between CADR for the Corsi-Rosenthal Box and the manufacturer reported (yellow triangles), the reduced manufacturer reported (blue circles), and air-velocity-estimated (red squares) air flow rates for the original box fan. The lines are linear fits forced through zero (slopes = 0.41, 0.58, and 0.47, respectively). (right) Relationship between CADR for the Corsi-Rosenthal Box and the measured pressure drop at low, medium, and high fan speeds.

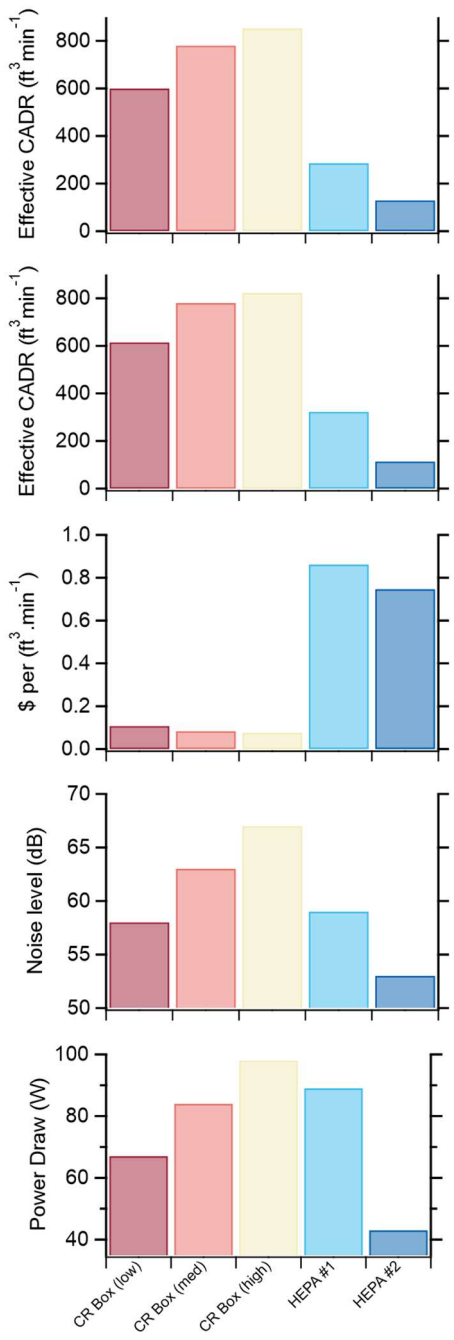

Figure S2-4. Results from Figure 2-3, shown as individual graphs rather than all together. Shown are (top to bottom) the effective CADR values determined in the home office and the classroom, the cost per effective CADR, the noise level, and the power draw.

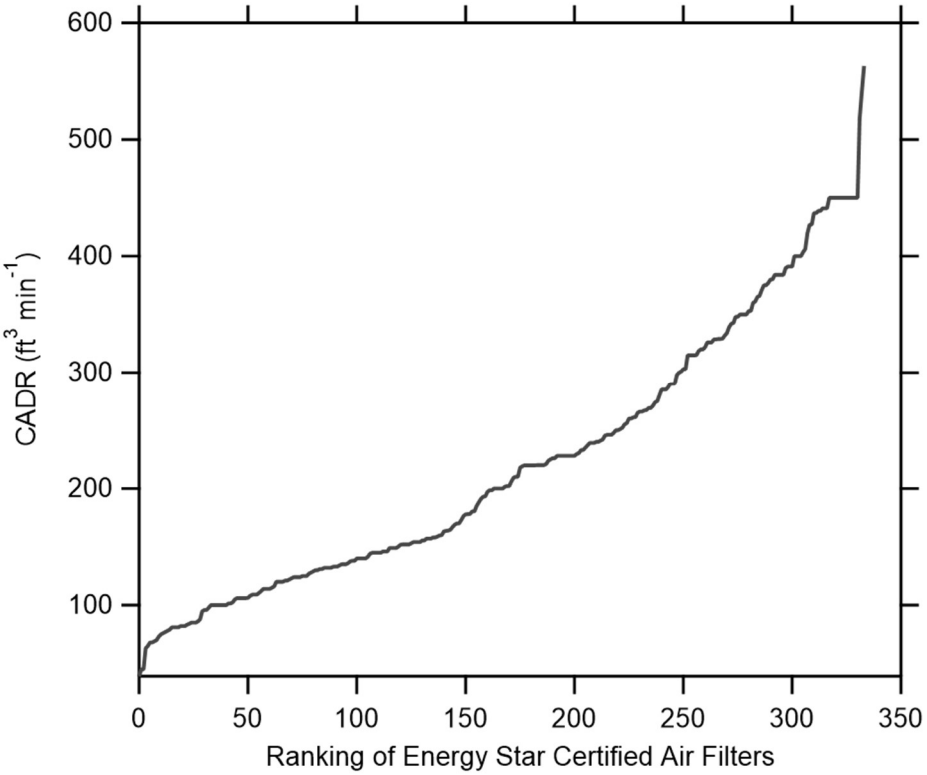

Figure S2-5. The distribution of maximum CADR values for commercially available filter-based air cleaners in the Energy Star database. These can be compared with the Corsi-Rosenthal Box.

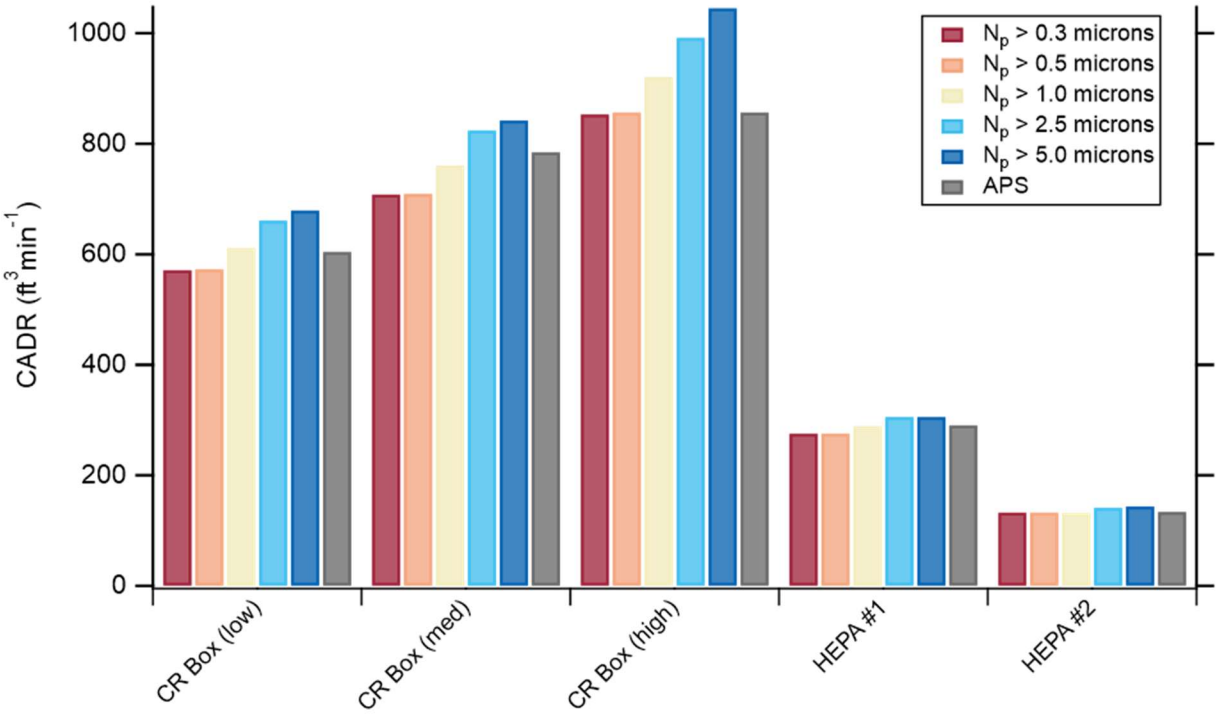

Figure S2-6. Comparison of the CADR values determined using the different apparent size bin number concentrations from the low-cost sensor (colors) compared to the CADRNp determined from the APS. Measurements are from the home office.

3 Development and validation of a humidified CAPS-PM$_{SSA}$ with an improved methodology to calculate truncation correction factor

Rachael Dal Porto[1], Ningxin Wang[2], Christopher D. Cappa[1, *]

[1] Dept. of Civil and Environmental Engineering, Univ. of California Davis; 1 Shields Ave., Davis, CA 95616 USA

[2] California Air Resources Board

CONTACT Christopher D. Cappa cdcappa@ucdavis.edu

ABSTRACT

Absorbing aerosols play an important role in the Earth's radiation budget, and current uncertainties associated with their radiative impacts remain substantial. An element of this uncertainty derives from insufficient understanding of the extent to which water, as a coating on absorbing particles, enhances the absorption. Here, we describe and characterize the performance of a cavity-attenuated phase shift particulate matter spectrometer (CAPS-PM_{SSA}) system that has been modified to enable concurrent aerosol extinction and scattering measurements, from which aerosol absorption is derived, at relative humidities up to ~90%. The modified instrument is referred to as the humidified CAPS (HCAPS). Additionally, we develop and validate an updated method to calculate the truncation correction factor, which is used to correct the scattering measurements, that can account for the effects of particle growth and compositional changes resulting from water uptake. The method can be applied to experiments that use either size-selected or polydisperse aerosol samples of either known or unknown composition. Overall, we show that measurements made with the HCAPS, when processed using the updated truncation correction method, enable accurate measurement of the influence of water uptake on light absorption.

3.1 Introduction

One way atmospheric aerosols impact climate is by altering the Earth's radiative budget by either scattering or absorbing incoming and outgoing solar and thermal radiation. When aerosols scatter incoming solar radiation back to space they provide a cooling effect by reducing the amount of light that is absorbed at the surface. Aerosols can also absorb incoming ultraviolet and visible radiation, depending on their composition, which warms the atmosphere. Absorbing aerosol components include black carbon (BC), some components of organic aerosols (collectively referred to as brown carbon (BrC)) and dust. These absorbing aerosols differ in their properties, including how strongly they absorb and how their absorption varies with wavelength.

Absorbing aerosols contribute disproportionately to the overall uncertainty in aerosol radiative forcing (Bond et al. 2013). Moreover, aerosol concentration and composition exhibit large spatial and temporal variability, which can cause regional forcing to differ substantially from the global average (Li et al. 2022; Williams et al. 2022). Global average BC direct radiative forcing (RF) is significant, positive, and uncertain, with median reported values ranging from 0.23 to 0.9 W/m^2 (Lund et al., 2018; Szopa et al., 2023; Li et al., 2022 and references therein). Consideration of absorption by BrC leads to a reduction in the overall cooling effect of organic aerosol (Laskin et al. 2015).

Since aerosol extinction is the sum of absorption and scattering, aerosol absorption can be measured directly or indirectly by measuring scattering and extinction and taking the difference. Aerosol optical properties depend on size, morphology, mixing state, and composition (Seinfeld and Pandis 2016). The single scattering albedo (SSA) is a ratio describing how scattering or absorbing a sample is. It ranges from zero (purely absorbing) to one (purely scattering):

$$Equation\ (1),\ SSA = \frac{b_{sca}}{b_{ext}}$$

It is important to understand how mixing of absorbing components with other aerosol components, either absorbing or non-absorbing, affects the overall absorption (Bond et al. 2013). A common assumption for modeling BC absorption is that coated BC adopts a core-shell morphology. In the core-shell assumption the solid aerosol component (here, BC) is coated by other aerosol components; most often both the core and overall particle are assumed spherical. Theoretically, coatings enhance the absorption by BC, with the extent of enhancement dependent on the size of the BC core and the relative thickness of the coating. Theoretical enhancements can be as large as a factor three or more under the core-shell assumption (Fierce et al. 2016; Lack and Cappa 2010; Bond et al. 2006; Jacobson 2001; Fuller et al. 1999).

However, it is possible that the solid absorbing component is located towards the outer edge of the particle or is not uniformly coated. In this case, the core-shell theory is not appropriate. The absorption enhancement in these non-core-shell particles is typically reduced compared to the equivalent core-shell morphology (Scarnato et al. 2013; Fuller 1995). Moreover, non-solid absorbing components, in particular BrC, could end up homogeneously mixed throughout an entire particle or preferentially segregated to a particular phase should phase separation occur. Theoretically, when an absorbing component is homogeneously mixed with other aerosol components there is also an enhancement of the overall absorption compared to an equivalent external mixture (Fuller et al. 1999).

Lab and field studies characterizing the magnitude of the absorption enhancement for BC-containing particles yield values that vary widely, from near unity (i.e., no enhancement) to greater than 2 (Xie et al. 2019; Liu et al. 2017; Cui et al. 2016; Peng et al. 2016; Saliba et al.

2016; You et al. 2016; McMeeking et al. 2014; Cappa et al. 2012; Lack et al. 2012; Khalizov et al. 2009; Knox et al. 2009; Moffet and Prather 2009; Zhang et al. 2008; Mikhailov et al. 2006; Schnaiter et al. 2005). Differences in the experimental conditions (e.g., monodisperse vs. polydisperse BC, the amount of coating), measurement method, or proper accounting of the contributions by BrC can help explain some of the variability that has been observed. However, a substantial limitation has been that nearly all these studies characterized absorption under dry conditions.

Water uptake by an aerosol also has an impact on the particle optical properties. The amount of water that a particle uptakes depends on particle composition and atmospheric conditions. Water by itself is purely scattering. When considered as a coating material, water can enhance absorption like any other coating material. The changes to optical properties owing to water uptake are characterized by $f(\mathrm{RH})_z$, which is the ratio of wet particle scattering, extinction, or absorption coefficients (b_z), to its dry counterpart:

$$\textit{Equation (2)},\ f(RH)_z = \frac{b_{z,humidified}}{b_{z,dry}}\ \textit{; where z = extinction, absorption, or scattering}$$

The impact water uptake has on absorption by aerosol particles is a key uncertainty in understanding the radiative forcing by BC and BrC. Experimental (Khalizov et al. 2009; Mikhailov et al. 2006) and modeling (Fierce et al. 2016; Ghan et al. 2012; Jacobson 2001, 2012) studies indicate water coatings play a prominent role in absorption enhancement. However, the actual influence of water uptake on absorption lacks a firm experimental basis in large part owing to a dearth of experiments (Brem et al. 2012; Zhang et al. 2008) and field observations, and limited tools to allow characterization of absorption at elevated relative humidity.

To improve model representation of absorbing aerosols and their coatings, further observational and experimental studies specifically measuring absorption from BC and BrC under humidified conditions are needed. Measurements of optical properties can be made with passive and remote sensing, as well as in situ. In situ measurements can be either online or offline, with most methods originally measuring absorption by dry particles. Filter based absorption measurements often have bias issues due to needing multiple corrections to account for the filter material and can overestimate absorption significantly when loading is high, and can pose issues under humidified conditions, including the aerosols already deposited on the filter taking up more water (Cappa et al. 2008; Lack et al. 2008). Some in situ and online absorption measurement methods use two separate measurements, one that measures scattering, and another that typically measures extinction. Some issues with using two separate instruments are that it can be difficult to ensure thorough instrument calibrations, and difficult to control sample conditions to ensure both measurements have the same conditions.

This study characterizes the performance of a humidified cavity-attenuated phase shift particulate matter spectrometer (HCAPS) system and demonstrates the performance for determination of aerosol optical properties, including absorption, at elevated humidity. The HCAPS measures scattering and extinction (and thus, absorption and single scattering albedo) concurrently on the same sample. A custom humidification box added before the commercial CAPS-PM_{SSA} enables alternating measurement of extinction and scattering for dry and humidified samples. Our system differs from other related setups (Carrico et al. 2021; Zhou et al. 2020), in two ways: (i) the use of a separated humidification box allows the humidified air stream to be directed to a multiple instruments or just a single CAPS-PM_{SSA}, and (ii) precise temperature control of the CAPS-PM_{SSA} enables robust determination of particle deliquescence.

This study also introduces a method to determine the truncation correction factor for scattering that accounts for aerosol water uptake as well as unknown aerosol composition.

3.2 Materials and Methods

3.2.1 Humidified Cavity Attenuated Phase Shift Spectrometer – PM_{SSA} (CAPS-PM_{SSA})

Aerosol scattering and extinction were measured at 630nm using a cavity-attenuated phase shift particulate matter spectrometer (CAPS-PM_{SSA}; Aerodyne Research) (Onasch et al. 2015). The CAPS-PM_{SSA} measures extinction based on the phase shift of a square-wave modulated light as it passes through a high-gain optical cavity. Scattering is determined concurrently on the same aerosol sample via the integration scattered light measured by a Lambertian integrating sphere nephelometer. The measured scattering requires a particle size and composition-dependent truncation correction factor to account for forward and backward scattered light that is not captured by the nephelometer. This truncation correction factor will be discussed further below. Here, we have modified the standard CAPS-PM_{SSA} instrument by enclosing the entire CAPS-PM_{SSA} cell in a temperature-stabilized and insulated box outfitted with a through-wall thermoelectric cooler controlled by a temperature controller. With this modification the CAPS-PM_{SSA} cell can be maintained up to a few degrees below ambient temperature. This helps to ensure that the lowest temperature, and therefore highest relative humidity, encountered by the air stream relative to the system is in the CAPS-PM_{SSA} cell. This helps with preventing condensation and with determination of the deliquescence point for samples that deliquesce. Relative humidity is characterized inline using an RH probe (Rotronic Hygroclip2) that is located in the same enclosure as the CAPS-PM_{SSA} cell and is thus at the same temperature as the cell. The RH probe was calibrated using saturated salt solutions.

To enable characterization of the influence of RH and water uptake on the measured scattering and extinction, an aerosol humidification system (the "RH Box") was added to the system upstream of the CAPS-PM_{SSA} instrument; the combination of the modified CAPS-PM_{SSA} and the RH Box will be referred to as the "HCAPS." A schematic of the HCAPS system is shown in Figure 1. The RH Box enables selective sampling by the CAPS-PM_{SSA} of a dry aerosol stream or of a humidified aerosol stream via a 3-way valve. The air stream is dried prior to sampling into the RH Box using denuder driers. The air stream is then split into a bypass (dry air) flow and a humidified flow. Humidification is achieved using a monotube Permapure Nafion drier (MD-700) in reverse (i.e., a humidifier), and where the amount of water added to the air stream is controlled by varying the temperature of the water flowing through the outer jacket of the humidifier. The temperature of the water is controlled to within 0.1°C using a bidirectional thermoelectric cooling system coupled with a heat exchanger. The water flow is controlled using a water pump.

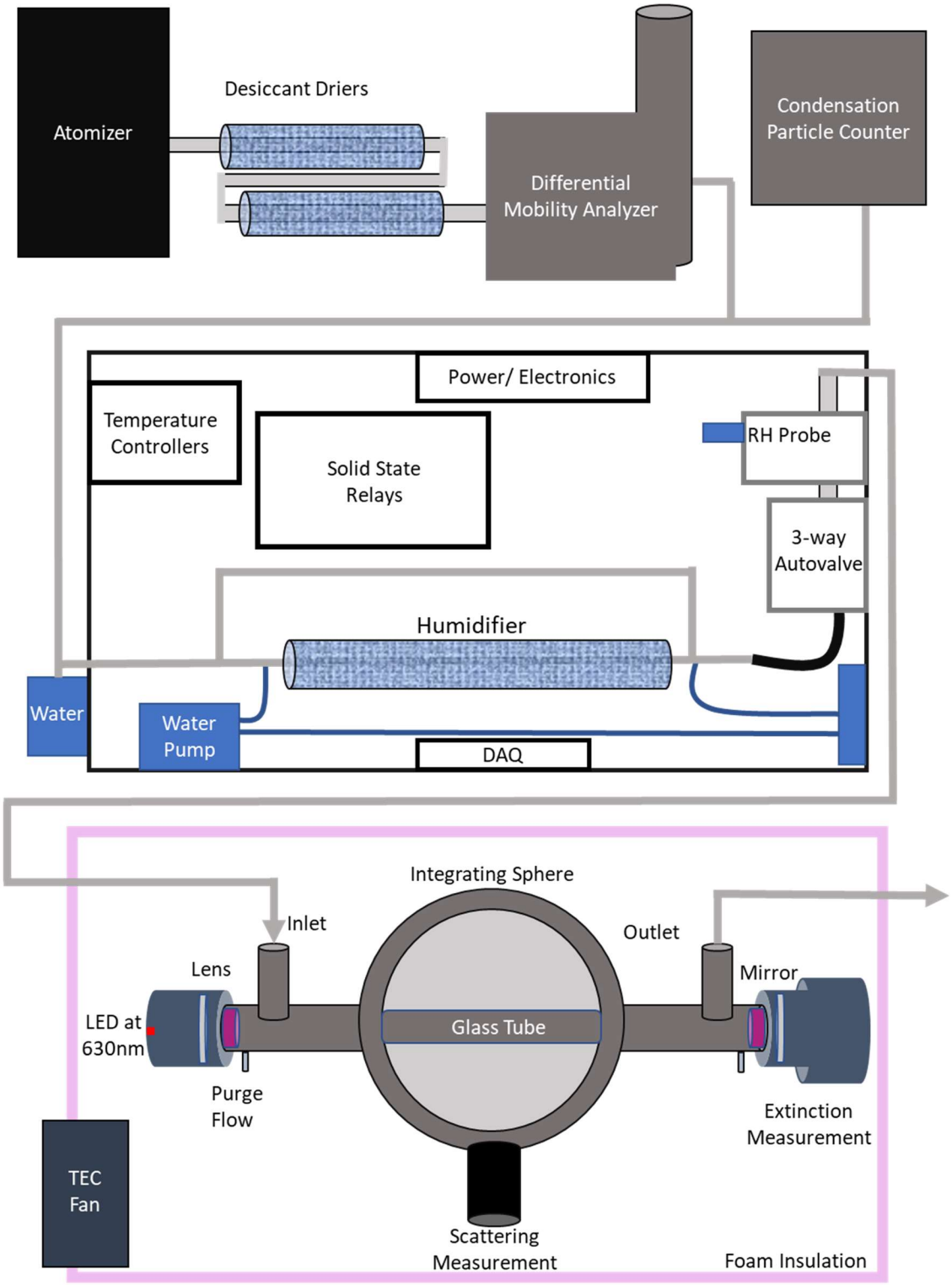

Figure 3-1 Schematic representation of the experimental setup, including the HCAPS system.

The RH Box is shown bounded by a black box and the modified Aerodyne CAPS-PM$_{SSA}$ is shown

bounded by a pink box. The aerosol flows are depicted in gray and the water flows depicted in dark blue.

Air constantly flows through both the bypass line and humidifier, with the air stream sampled to the CAPS-PM_{SSA} selected using an automated 3-way ball valve and the alternate air stream sampled to an excess pump using a 3-way solenoid; the two 3-way valves operate out of phase to allow for constant flow through both channels. The combination of continuous flow, control of the water temperature in the humidifier, and cooling and temperature stabilization of the CAPS-PM_{SSA} cell allows for accurate control of the humidification over the range of about 55% < RH < 95%. The various temperature, RH, and valve state values were controlled and measured using a custom Labview program with an NI-6008 DAQ device. In these studies, the CAPS-PM_{SSA} flowrate was 0.9 lpm.

The system setup allows operation in two modes. In one, the system is toggled between the dry and humidified channels with fixed or variable dwell times and a constant high RH (referred to as the constant RH mode). In the other, the system slowly ramps the RH by ramping the water temperature while continuously sampling from the humidified channel (referred to as RH ramping mode). With the constant RH mode, we have found that the minimum dwell time is limited by adsorption and desorption of water from surfaces in the system. There can be substantial lags in the response as the system equilibrates to a new condition; we have empirically determined that five-minute dwell times are sufficient. Particle-free air flow was used to determine instrument responsivity, with Figure S1 showing the response in RH when switched between the dry and humidified flow. With the RH ramping mode, if the RH is ramped too fast the observed deliquescence points for pure salt solutions are underestimated. Ramping

times of about 0.1 °C/min or less allow for good performance. This corresponds to an overall time for ramping from lower (~55%) to higher (~95%) RH of about an hour. The HCAPS system developed here shares some similarity to the instrumentation and designs of Carrico et al. (2021) and Zhou et al. (2020). The system described here differs from the Carrico et al. system in that in the Carrico et al. system, the entire system is in a temperature-controlled box, whereas in our system as well as the Zhou et al, system, only the CAPS cell is temperature controlled.

3.2.2 *Experimental Description*

We used the HCAPS to characterize how light absorption for single component aerosol of specific composition responds to changes in RH (Table 3-1). Polydisperse aerosol were generated from aqueous solutions with an atomizer and then dried to <20% RH by passing them through two silica bead diffusion driers. A differential mobility analyzer (DMA) was used to size select particles from this dry aerosol stream. The resulting monodisperse dry aerosol stream was mixed with clean, dry air to ensure sufficient flow to downstream instrumentation while maintaining a sample flow through the DMA of 0.5 lpm. The air stream was then split between a condensation particle counter (CPC; TSI Model 3076) and the HCAPS. Figure 1 outlines the laboratory setup.

Here, we focus on RH ramping experiments. In a typical experiment, dry aerosol of a given size and composition are initially sampled through the bypass to the CAPS-PM_{SSA}. The measured optical cross-sections for these dry particles yield the reference dry values for the determination of f(RH). The RH Box valves are then switched to allow sampling of the humidified aerosol stream starting from the lowest “high” RH value, typically 60-65%. The RH is then slowly ramped by increasing the temperature of the humidifier at 0.1 °C/min until the RH reaches

~90%. At this point the RH Box valve is switched back to allow sampling from the bypass, the temperature of the humidifier is dropped to its lowest value, the selected particle size is changed, and a new ramping cycle is started. Particle sizes over the range 75 nm to 500 nm Dp_m were considered, with the exact values varying by system.

Table 3-1: Aerosol types considered and their general properties

Single Component Aerosol	**Properties**
Ammonium Sulfate	Non-Absorbing, soluble
Nigrosine	Absorbing, moderately soluble (BrC surrogate)
Fullerene Soot	Absorbing, mostly insoluble (BC surrogate)

3.2.3 *Data Analysis and Correction Factors*

Accurate determination of light absorption coefficients in the HCAPS requires correction of both the directly measured extinction and scattering. These corrections include a correction of the extinction coefficient (b_{ext}) for absorption by water vapor, and a correction of the scattering coefficient (b_{sca}) for size and RH-dependent truncation losses. The absorption coefficients are then determined from the corrected b_{ext} and b_{sca}.

In the case of experiments using size-selected particles, accurate determination of the truncation correction factor (C_{ts}) requires that we account for the influence of multiply charged particles on the measured b_{ext} and b_{sca}. In the case of a polydisperse particle distribution, correction of the b_{sca} requires determination of an optically weighted C_{ts} value. In either case, for humidified particles we must additionally account for the influence of water uptake and particle growth on the C_{ts}. A

schematic of the analysis methodology is depicted in Figure 2 and a more detailed description of the corrections follows. The experiments here all use size-selected particles.

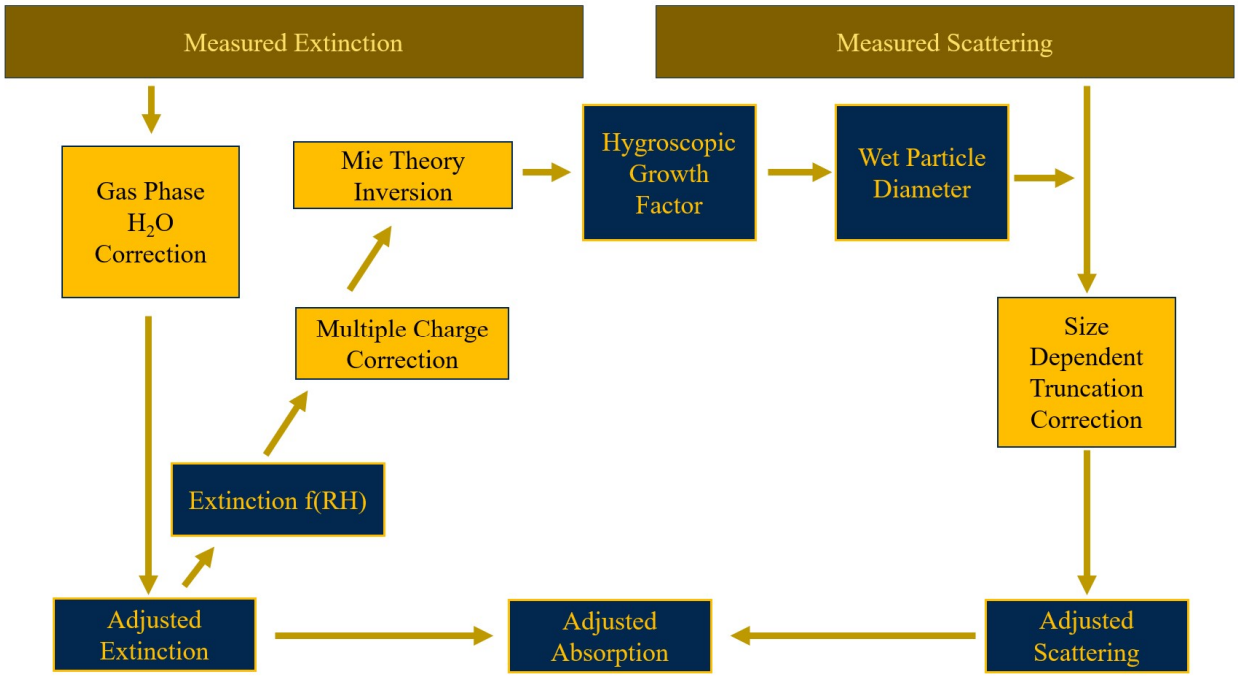

Figure 3-2. Schematic of data analysis methodology for the analysis of extinction and scattering observations from the HCAPS system. Extinction measurements undergo a gas phase water correction and are then used to determine a hygroscopic growth factor, and consequently the particles wet diameter. This wet diameter is then used when determining and applying the size dependent truncation correction factor to finalize the adjusted scattering measurement

Water vapor absorption correction: Although water vapor absorbs weakly in the visible, at 630 nm the cross-section is sufficiently large that its absorption has a notable impact on the observed extinction. We determined the water vapor sensitivity of the observed extinction equals 0.04 Mm^{-1} per 1% change RH. The correction for this artifact is referenced to the preceding instrument zero and the RH during that zero (RH_{ref}):

$$\textit{Equation (3)},\ b_{ext,corr} = b_{ext,obs} - 0.04\frac{1}{Mm}\cdot\left(RH - RH_{ref}\right)$$

Accounting for multiply charged particles: After the corrected extinction is determined, the $f_{RH,ext}$ is calculated. The monodisperse aerosol from the DMA can include multiply charged particles that have equal electrical mobility but larger actual diameters than those selected by the DMA (under the assumption of single charges). This leads to larger extinction coefficients compared to the case with all particles at the selected size. This has two implications. First, the inversion of hygroscopic growth factors from $f_{RH,ext}$ depends on the particle size; for the same $f_{RH,ext}$ larger diameters will yield larger GF_{RH} values. Second, the C_{ts} values are implicitly size-dependent.

There are two ways we dealt with multiply charged particles. In the first, we determined the fraction of singly (q1) and doubly (q2) particles that yielded closure between the observed and calculated extinction cross-section for the dry particles of a given size under an assumption of spherical particles. In general, the q2 fraction depends on the combined effects of charging statistics and the shape of the original polydisperse particle size distribution; for our experiments the q1 fraction typically increased with particle size. In the second, we determined a single value for an equivalent effective diameter ($D_{p,m,eff}$) that allowed for closure of the observed and calculated b_{ext}, again assuming spherical particles. Use of either of these two yielded similar results, and the results presented here used the second method. In practice, the importance of q2 particles could be reduced via modifications to the experimental setup, for example via double size selection after reneutralization or mass selection followed by size selection; such modifications were not possible in our experiments owing to limitations in instrument availability. For instances where polydisperse particles are sampled directly into the HCAPS, such as ambient sampling, no such correction for multiple charging is needed.

Determination of hygroscopic growth factors: The RH-corrected $f_{RH,ext}$ values are then converted into equivalent hygroscopic growth factors using spherical-particle Mie theory along with the effective diameter values. Specifically, the dry particle extinction is calculated using the dry particle $D_{p,m,eff}$ values and humidified particle extinction is calculated using $D^{RH}_{pm,,eff} = GF_{RH} \cdot D^{dry}_{p,m,eff}$ and where the selected GF_{RH} values used are those that minimize $|f^{obs}_{RH,ext} - f^{calc}_{RH,ext}|$. In performing the inversion, we use steps of $\Delta GF_{RH} = 0.01$.

Water typically has a smaller real refractive index (n) than most aerosol components. Also, water is nearly (although not entirely) non-absorbing in the visible with an imaginary refractive index (k) close to zero. As such, water uptake engenders a decrease in n for both absorbing and non-absorbing systems and also in k for absorbing systems. The refractive indices used in the Mie calculations for humidified particles are calculated assuming volume mixing rules for homogeneous mixtures (Erlick et al. 2011).

Truncation correction for scattering: There are apertures at the entrance and exit of the CAPS cell to allow light, and the air stream, to enter and exit. The directly observed scattering thus will be biased low, as some of the light scattered will exit the cell through these apertures; this is called truncation. The correction for this lost light is the truncation correction factor and is discussed in detail in the next section. The corrected extinction measurement and wet effective diameter are used to determine the truncation correction factor.

The truncation correction factor (C_{ts}) is applied to yield the corrected scattering $b_{sca,corr}$ by dividing the raw scattering measurement $b_{sca,meas}$ by the truncation correction factor:

Equation (4), $$\boldsymbol{b_{sca,corr}} = \boldsymbol{b_{sca,meas}} \Big/ \boldsymbol{C_{ts}}$$

The C_{ts} will be a value between zero and one. The lower the C_{ts} value, the larger the losses from truncation, and thus the larger the corrected scattering value. Values of C_{ts} close to one will yield corrected scattering values only slightly larger than measured.

3.3 Truncation Correction Factor and Validation

As noted above, not all the scattered light is measured by the integrating nephelometer due to the geometry of the cell and limitations in characterizing scattering in the near forward and backward directions. The truncation correction factor accounts for unmeasured scattering and is used to correct the observed scattering. Values of C_{ts} for a given system can be developed via empirical measurements or theoretical modeling. Onasch et al. (2015) derived a theoretical C_{ts} for the CAPS-PM_{SSA} based on Mie theory, which has since been updated to include an additional probability-based correction for reflection of light off the inner glass tubing (Modini et al. 2021; Liu et al. 2018). The C_{ts} depends on the following parameters: the complex refractive index of the particles, incident light wavelength, cell geometry, and particle diameter.

We expand on this previous work, specifically the Modini et al. (2021) update to Onasch et al. (2015), to account for the influence of growth by water uptake along with any changes in the refractive index due to water uptake on the truncation correction factor. We also introduce an iterative approach that can be used to determine the truncation correction factor for systems of unknown composition, and therefore unknown refractive index.

3.3.1 *Truncation correction factor for Known Species*

Upon humidification, aerosols may take up water and grow, impacting both the size and refractive index relative to the dry particle. This affects the scattering phase function and thus the

truncation correction factor necessary. Larger particles tend to preferentially scatter more in the forward direction, which corresponds to a larger truncation. Consequently, water uptake increases the value of C_{ts} relative to the dry particle. Water uptake also leads to a change in the refractive index, typically a decrease in both the real and imaginary components. The impact of both effects much be accounted for to determine an appropriate truncation correction factor for humidified particles.

The influence of particle growth induced by water uptake is accounted for here by determining the RH- and composition-dependent GF_{RH} values from the $f_{RH,ext}$ values, as discussed above. This provides both the effective wet particle diameter and the associated refractive index for use in calculations of the truncation correction factor.

For non-absorbing systems, the SSA calculated using the uncorrected scattering ($b_{sca,meas}$) and the corrected extinction ($b_{ext,corr}$) corresponds to the C_{ts}. We refer to this initially uncorrected SSA as the raw SSA (SSA_{raw}). The reason for the equivalency of SSA_{raw} and C_{ts} for a non-absorbing system is implicit in the definition of the SSA and the truncation correction factor; the actual SSA for a non-absorbing system is one, and thus any deviation from one for SSA_{raw} must result from scattered light lost from truncation. Consequently, size-dependent measurements of SSA_{raw} for a non-absorbing system provide a test for theoretical formulations for the truncation correction factors.

Here, we assessed the theoretical truncation correction factor (Onasch et al. (2015); Modini et al., (2020)) by comparing with the observed SSA_{raw} values (equivalent to C_{ts}) for both dry and wet ammonium sulfate particles (Figure 3). The dry and humidified measurements have been grouped into a single dataset and are shown versus the appropriate dry or wet particle diameter.

For reference, the dry selected diameters ranged from 75-500nm (with corresponding $D_{p,m,eff}$ values from 121-684nm). Truncation curves are shown for constant GF values ranging from 1.1 to 2.5 to illustrate the impact of water uptake on the truncation correction factor. The truncation curves exhibit little dependence on the assumed GF below wet diameters of 700 nm or so indicating a lack of sensitivity to variation in the refractive index for these non-absorbing particles. Above this size the observations are most consistent with the theoretical curves for larger GF values.

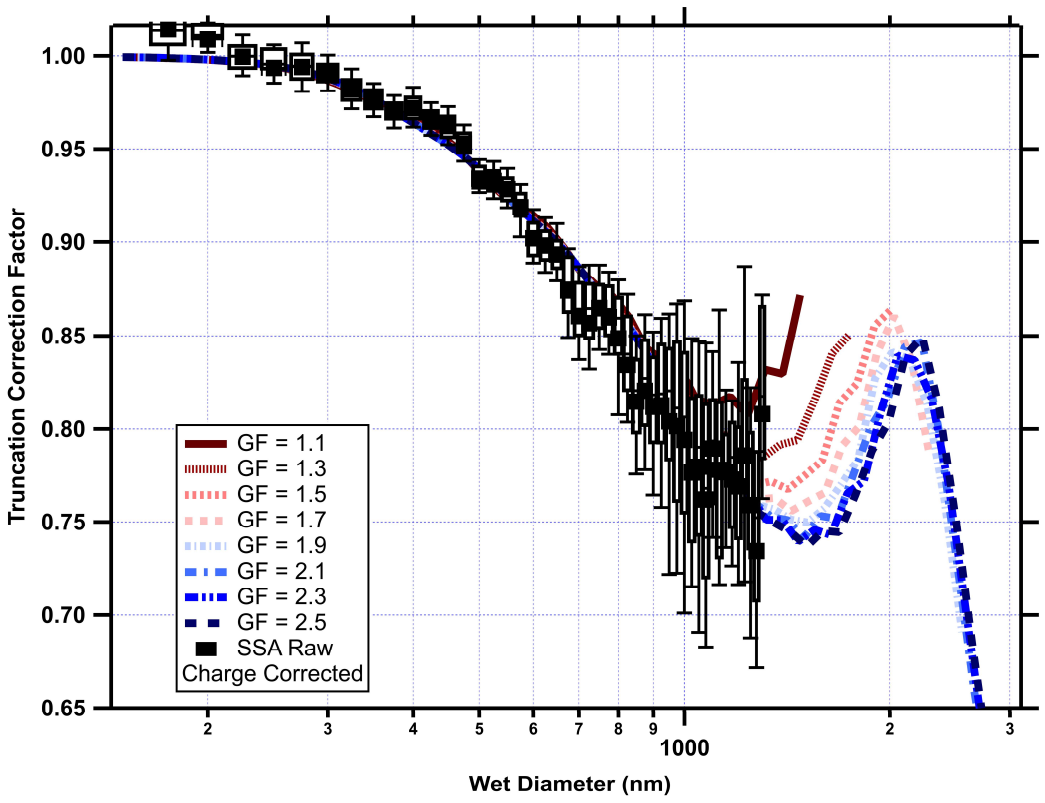

Figure 3-3. Calculated (lines) and measured (box and whisker) truncation correction factor values as a function of wet particle equivalent diameter for dry and humidified ammonium sulfate particles. Different line color/styles correspond to different assumed growth factors. Note

that the measured values have been graphed against their respective $D_{pm,eff}^{RH}$ values to account for the influence of multiply charged particles.

As noted above, the presence of multiply charged particles leads to the observed extinction cross-sections to be larger than expected based on the selected particle size. This in turn has implications for calculation of the truncation correction factor. If the selected diameter were used, rather than the effective diameter, the calculated C_{ts} is overestimated (closer to unity) and the truncation correction therefore underestimated. Additionally, if the diameters used did not account for particle growth due to water uptake the truncation would again be underestimated. For reference, Figure S2 shows the calculated dry truncation correction factor without accounting for scattering off the inner quartz tube, and without accounting for multiply charged particles. Similar to Figure S2, other studies comparing theoretical truncations with scattering measurements observe C_{ts} that are higher than the measured SSA (Carrico et al. 2021).

There is generally good agreement between the observed raw SSA and calculated truncation correction factor below effective diameters around 700 nm. At larger wet diameters the spread of observed SSA_{raw} values at a given wet diameter increases. This aligns approximately with the point at which the different calculated truncation curves begin to diverge for different GF values. Recall that the humidified measurements here were made at a range of RH values above the deliquescence point and thus the measurements at a given wet diameter correspond to various combinations of dry diameter and GF values. Although there is greater spread at these larger diameters the observed SSA_{raw} still fall within the variance of the calculated truncation curves for particles up to 1200nm. Given that the largest dry $D_{p,eff}$ = 684 nm it is perhaps not surprising,

however, that the average SSA_{raw} values most agree with the truncation curves corresponding to larger GF values for larger particles.

The model-measurement comparison in Figure 3 demonstrates that the Onasch-Modini truncation model, updated to account for water uptake and the influence of multiply charged particles, provides an accurate accounting of the influence of truncation on the scattering measurements. However, the curve shown is specific to humidified ammonium sulfate particles. Distinct, system-specific truncation correction factor curves are needed for particles with different real refractive indices or that are absorbing (i.e., non-zero imaginary components). We explore this by calculating and comparing truncation curves for four aerosol types corresponding to ammonium sulfate (m = 1.521 + 0i), nigrosine (m = 1.67 + 0.26i), fullerene soot (m = 1.8 + 0.6i), and a highly absorbing aerosol (m = 1.8 + 1.13i). The calculations are preformed both for dry particles and assuming varying GF values under volume mixing assumptions.

For dry particles, the calculated truncation curves for absorbing aerosol all decrease monotonically up to the largest dry diameter considered here and exhibit much less structure compared to the non-absorbing aerosol (Figure 4). The absolute values of the truncation correction factors differ between the absorbing and non-absorbing systems above about 350 nm diameter, with smaller C_{ts} (and therefore larger truncation) for the absorbing systems. The calculated curves exhibit relatively small differences between absorbing systems despite their very different imaginary refractive indices.

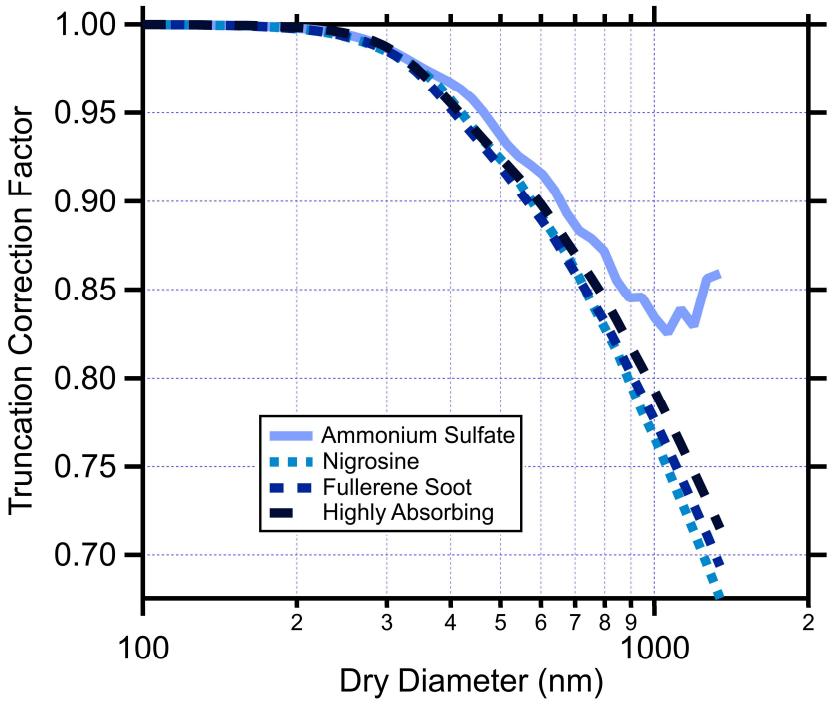

Figure 3-4 Modeled truncation curves for dry particles of different composition and refractive index. Differences between the curves becomes notable above 350nm, with all absorbing systems differing greatly from the non-absorbing system (ammonium sulfate), especially above 1000nm. The truncation correction factors for the absorbing systems are generally smaller than for the non-absorbing system larger particles and the curves generally smoother.

Calculated truncation curves are shown as a function of wet diameter for the humidified particles with assumed GF values >1 (Figure 5), with the same curves versus the original dry diameter shown for reference in Figure S3. Comparison between the truncation curves shown versus dry diameter and versus wet diameter illustrates the importance of capturing both the effects of particle growth and of changes to the refractive index from water uptake. In general, for the absorbing systems, the calculated C_{ts} values at a given wet diameter increases towards unity as the GF increases. However, for these systems the influence of water uptake decreases as the

imaginary refractive increases, i.e., as the systems become more absorbing, for a given diameter. The effect of water uptake for the absorbing systems contrasts starkly with the non-absorbing system, for which water uptake leads to a smaller C_{ts} for a given wet diameter. Note that consideration of the C_{ts} values at a given wet diameter illustrates the influence of changes to the refractive index on the truncation, separate from the influence of growth. For the largest GF values considered the truncation curves for the non-absorbing and less absorbing systems start to converge, likely because at the largest GF the particles are more than 90% water by volume. This is most evident in the 'bump' in the truncation curve at about 2,000 nm. However, for the strongly absorbing system (Figure 5D) the effect of water uptake is limited. For GF = 2.5 the complex RI values for the absorbing systems are 0.017 (nigrosine), 0.038 (fullerene soot), and 0.072 (strongly absorbing). Comparing these suggests that water uptake must reduce the complex RI to less than about 0.07 to have a notable impact on the truncation correction factor, but even then, the influence is most notable above about 1,000 nm diameter.

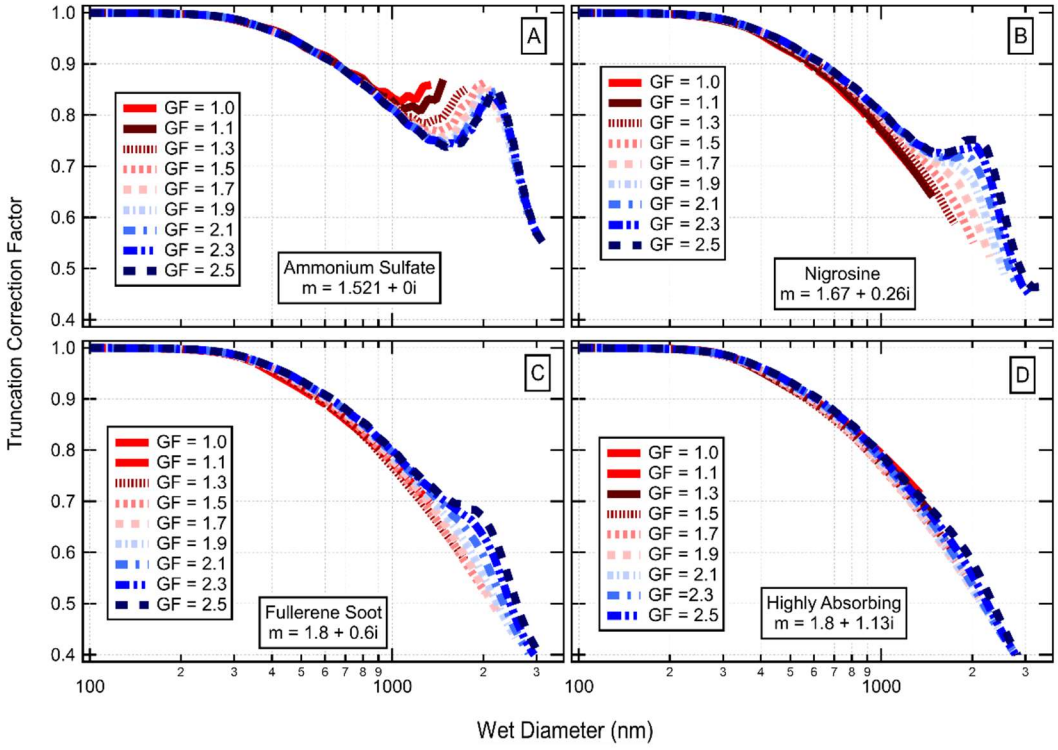

Figure 3-5. Modeled truncation correction factor as a function of wet diameter and growth factor for four dry particle systems. Calculations are shown for (A) ammonium sulfate, (B) nigrosine, (C) for fullerene soot, and (D) for a highly absorbing aerosol.

It is important to note that these calculations assume volume mixing rules apply for water and the absorbing species, which may not be appropriate for highly absorbing species such as black carbon. Moreover, such highly absorbing components tend to have limited intrinsic solubility and thus would not exhibit large growth factors even at high RH when externally mixed from other components. Internal mixing of soluble components, such as ammonium sulfate, with non-soluble absorbing components like black carbon can enable water uptake by the mixed-component particle with the overall GF dependent on the relative abundance of the soluble and non-soluble components (Baynard et al. 2006).

3.3.2 *Truncation Correction Factor for Unknown Species*

As illustrated above the truncation correction factor can be calculated for any particle of known refractive index. However, for unknown systems, which includes ambient particles, the refractive indices are not a priori known. Consequently, determination of the truncation correction factor becomes more difficult. We propose that an iterative approach can allow for reasonable determination of the system-appropriate truncation correction factor. As shown above, the effect of using an inappropriate refractive index is particularly important for particle diameters larger than about 1,000 nm, as below 1,000 nm the truncation curves are reasonably similar, although do depend on the absorptivity of the system. Figure 6 shows examples of the dependence of C_{ts} on the imaginary part of the refractive index for four particle diameters ranging from 440 nm to 1343 nm. In these examples the real part of the refractive index linearly increases with the imaginary portion, following the (n,k) pairs discussed later on. . The C_{ts} values are reasonably independent of k below about 0.07, but at $k > 0.07$ the calculated C_{ts} first decrease and then increase.

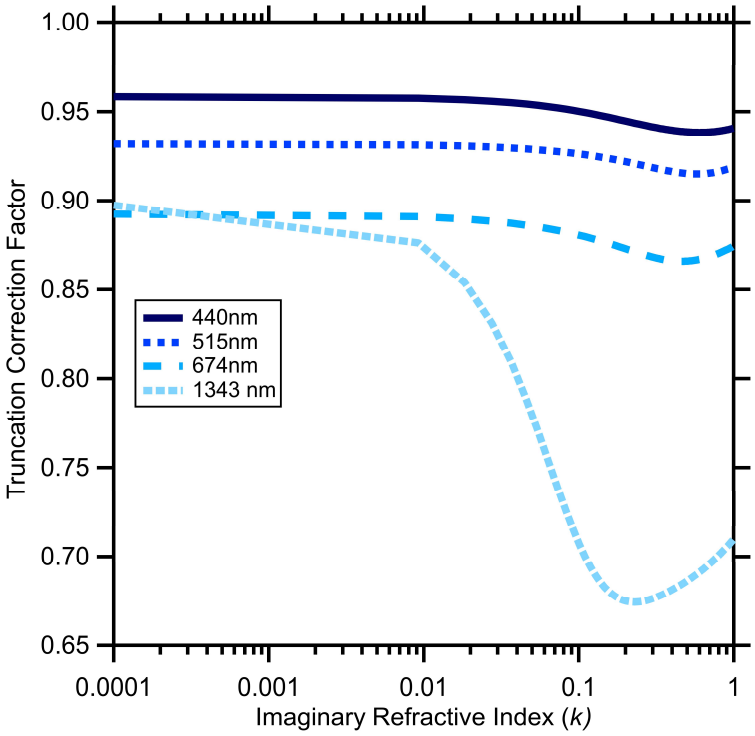

Figure 3-6. Truncation correction factor vs. imaginary refractive index (k) for 440, 515, 674, and 1343 nm diameter particles. At more absorbing imaginary refractive indices, the curves' behaviors deviate with larger diameter particles experiencing a strong decrease in C_{TS}.

The refractive index for an unknown mono- or polydisperse system can be inverted from the measurement of any two of extinction, scattering, absorption cross-sections under a spherical particle and homogeneous mixture assumption. In the CAPS-PM_{SSA} the extinction measurement is independent of knowledge of the refractive index. However, this is not the case for scattering (and therefore also for absorption) as the measured scattering must be corrected for truncation losses, which depends on knowledge of the refractive index. As such, in the case of particles with unknown refractive index a recursive method is required to determine the appropriate truncation correction factor. We develop the following general approach to this problem.

We start by constraining the space of (*n,k*) pairs that reasonably characterize aerosol complex refractive indices. Specifically, we assume a functional form for the relationship between n and k that spans from non-absorbing to highly absorbing. Here, we have chosen a functional form that approximately connects ammonium sulfate to nigrosine to fullerene soot to strongly absorbing aerosol (i.e., BC). In the computational implementation we use 110 linearly spaced (*n,k*) pairs; see supplemental section S3, and Figure S4 for more information. This reasonably captures the range of refractive indices seen in common aerosols (Zarzana et al. 2014).

The (*n,k*) pairs are used to generate 2D matrices of extinction and scattering cross-sections and of SSA as functions of particle diameter and refractive index for dry particles. The associated truncation correction factor for each (*n,k*)-diameter combination is calculated for dry particles and also for the corresponding wet particles as a function of growth factor, with the RI adjusted to account for water uptake assuming volume mixing. In the computational implementation we use steps of $\Delta GF_{RH} = 0.01$ from 1.00 to 2.5. The range and set of particle diameters used is arbitrary but should be selected to conform with experimental needs; in our case, we used 110 diameters corresponding to the median diameters scanned by a Brechtel SEMS as used by our group in recent field studies. Although the experiments in this study use monodisperse particles, we generalize the method for application to either monodisperse or polydisperse systems.

For monodisperse particles we calculate the SSA_{raw} for particles and use the selected particle diameter to determine an initial (*n,k*) pair to use by selecting that which minimizes $\boldsymbol{\Delta SSA = |SSA_{raw} - SSA_{calc}|}$. With this initial (*n,k*) pair the observed and calculated extinction cross sections are compared, as discussed above, to select an effective diameter to use. Then, the C_{ts} is calculated using this initial (*n,k*) pair and the $D_{p,m,eff}$, allowing for an initial correction of the

scattering coefficient and determination of a corrected SSA. The process is then repeated to extract an updated (*n,k*) pair using the corrected SSA, which is used to determine an updated $D_{p,m,eff}$ and then C_{ts}, and finally a newly corrected scattering coefficient and SSA.

For polydisperse distributions, the size-dependent extinction and scattering cross-section values are weighted by an observed number concentration size distribution of a particular sample ($dN/dlogD_{p,m}$). Integration across all sizes allows for determination of appropriately size-weighted properties (i.e., the b_{ext}, b_{sca}, and SSA) as a function of refractive index. The observed SSA_{raw} is compared with the matrix of calculated SSA values, and the refractive index that minimizes $\boldsymbol{\Delta SSA}$ is selected. A size-weighted truncation correction factor is determined using this initial (*n,k*) pair, which is in turn used to correct the scattering coefficient. As with monodisperse particles, the process is repeated to yield a fully corrected scattering coefficient and SSA. Figure 7 visualizes this methodology.

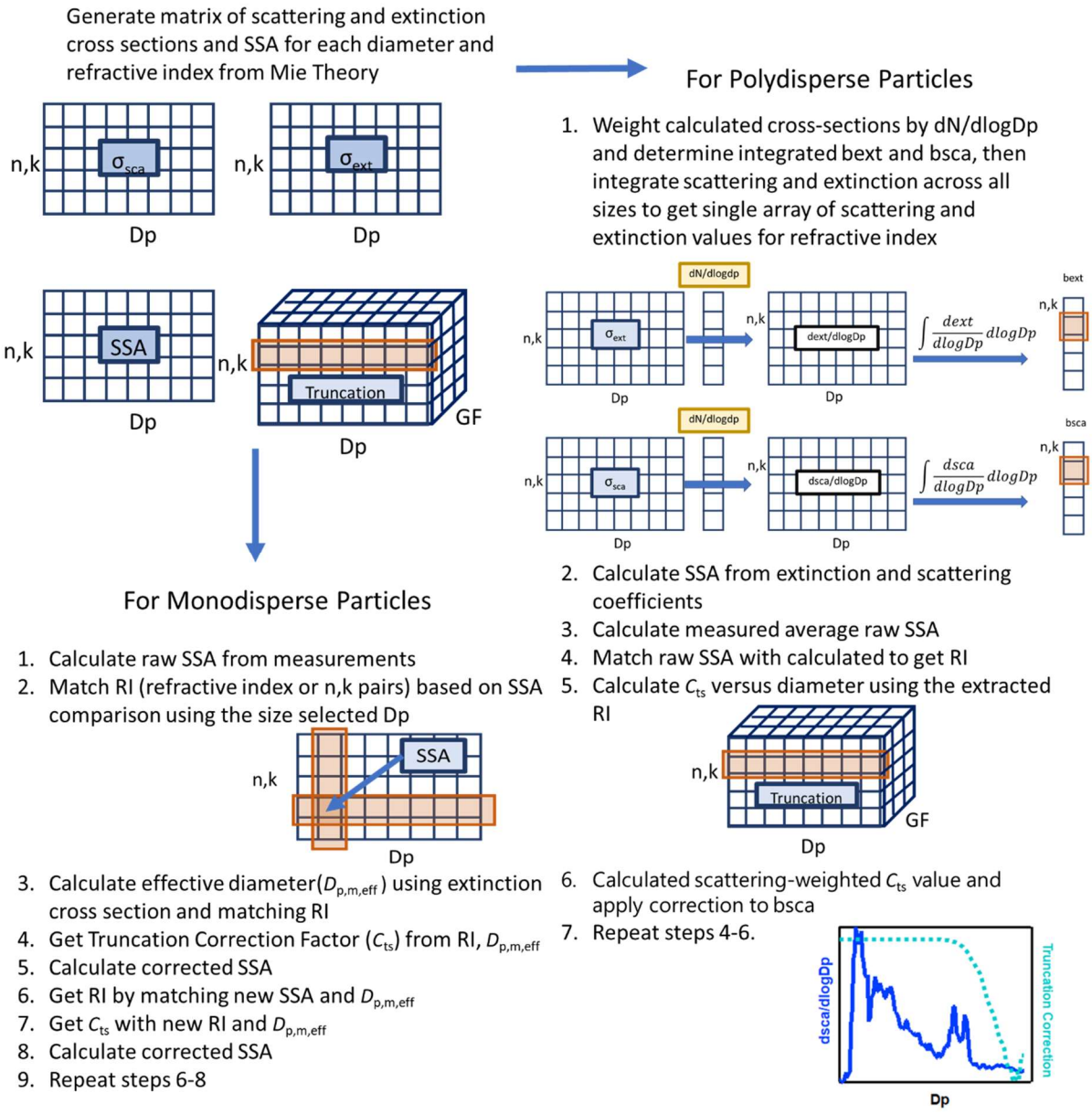

Figure 3-7. Schematic of methodology used to determine truncation correction factor for an aerosol sample of unknown composition.

Figure 8 shows examples of the SSA as a function of k for six dry diameters; in this case, the general (n,k) relationship is used and so the n values are changing with the k values. With increasing k, the SSA drops monotonically up to about $k = 0.1$ for all sizes considered. As k continues to increase (along with n) the SSA approximately levels off or even increases in the

case of the larger particle sizes. Consequently, for some sizes consideration of the $\boldsymbol{\Delta SSA}$ values does not yield a unique (*n,k*) pair. In such instances, the pair with the smallest *k* is chosen in the iterative approach. Note that if the *n* were held constant the SSA would decrease monotonically with *k*.

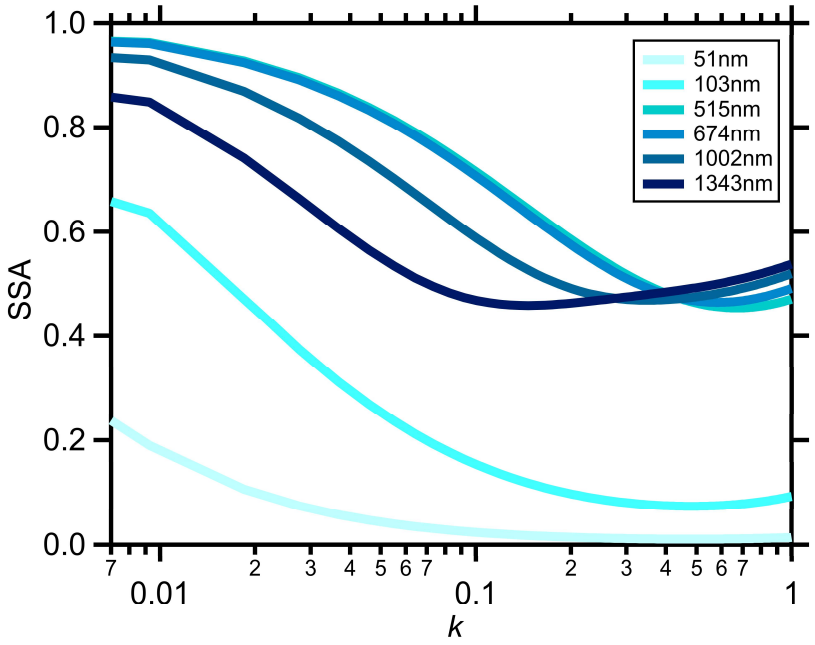

Figure 3-8. Modeled SSA for six different diameters as a function of the imaginary refractive index, k. For smaller k values, the aerosol has higher scattering properties and thus a larger SSA that drops quickly with an increase in k.

The effectiveness of this iterative method was tested experimentally using monodisperse nigrosine and fullerene soot particles. The iterative method retrieved a complex refractive index for 150 nm selected diameter nigrosine particles of $n = 1.57 + 0.13i$ and a corrected SSA value of 0.47. This compares favorably with the corrected SSA obtained using the literature RI for nigrosine ($1.67 + 0.26i$), with $SSA_{corr} = 0.45$. For 200 nm size selected fullerene soot, the

retrieved RI was $n = 1.67 + 0.52i$, with a corrected SSA value of 0.29. This too compares favorably to the corrected SSA obtained using the literature RI of fullerene soot (1.80 + 0.6), with $SSA_{corr} = 0.27$. The proposed methodology retrieved an SSA within 0.02 of the calculated value using literature refractive index values for both solutions and convergence was achieved within three iterations.

3.4 Laboratory Measurements

3.4.1 *Non-absorbing Aerosol – Ammonium Sulfate*

The influence of water uptake on ammonium sulfate extinction, scattering, and the SSA for monodisperse particles was characterized by ramping RH from 65% to 88% RH and comparing with dry particles (RH <20%) (Figure 8). The results shown are averaged across all dry sizes (ranging from 100-300nm). Clear deliquescence behavior is observed at 78% RH, with both the $f(RH)_{ext}$ and $f(RH)_{sca}$ increasing from unity at that threshold; the observed deliquescence RH is consistent with literature values (Seinfeld and Pandis 2016). Although the deliquescence is quite sharp some minor growth is observed starting at 77% RH, which could result from slight temperature gradients in the CAPS-PMSSA enclosure. We note that our design improves on that of Brem et al. (2012) in that by cooling the optical cell the deliquescence points obtained are consistent with literature, rather than being underestimated. As ammonium sulfate is non-absorbing the SSA should be constant at 1 throughout the RH range. We measure an average SSA of 0.99 +/- 0.03 in the pre-deliquescence range and 0.98 +/- 0.02 in the post-deliquescence range, yielding a ΔSSA of 0.01 (***Figure 3-9***). This illustrates the effectiveness of the GF-dependent truncation correction factor method introduced above. For a non-absorbing system, the absorption is zero and the $f(RH)_{abs}$ therefore ill-defined and thus not presented.

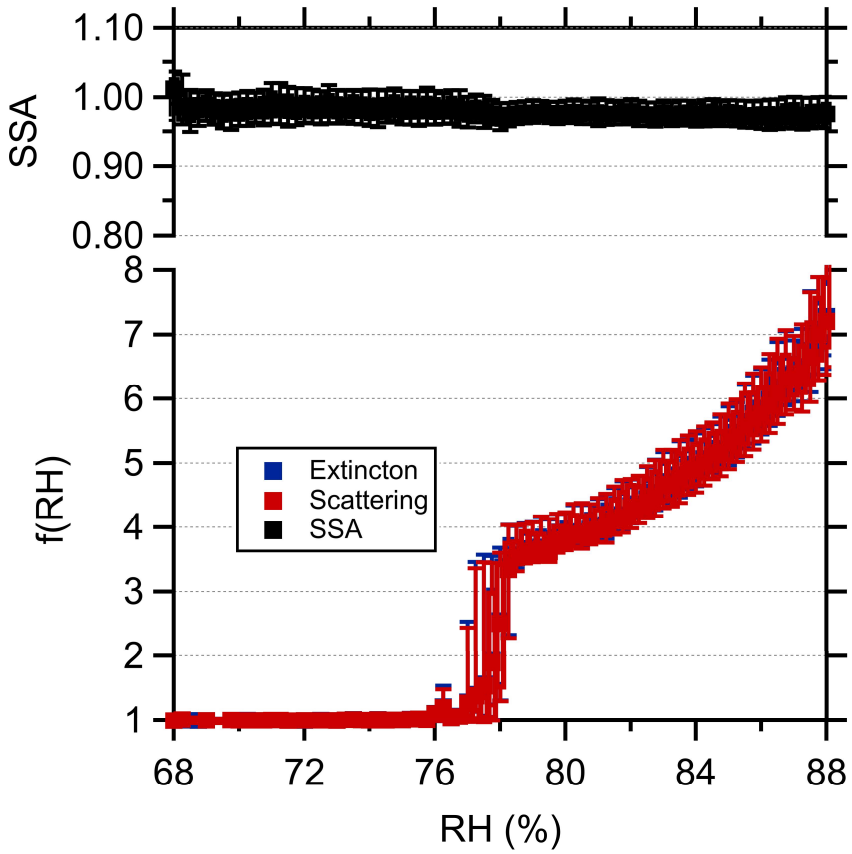

Figure 3-9. The f(RH) for extinction and scattering (bottom) and SSA (top) for size-selected ammonium sulfate ramping from dry RH to 88% RH averaged over all diameters ranging from 100nm- 300nm. A step change in f(RH) extinction and scattering is observed around 78% RH, at the expected deliquescence point of ammonium sulfate.

3.4.2 *Absorbing Aerosol – Nigrosine and Fullerene Soot*

The optical properties of size selected 150nm nigrosine and 200nm fullerene soot were measured from below 40% RH (dry) to above 85% RH**.** Nigrosine is partially soluble in water at approximately 0.1% (w/v) at room temperature. The $f(RH)_{ext}$ and $f(RH)_{sca}$ values exhibit continuous, albeit relatively small increases with increasing RH, ultimately reaching 1.4 and 1.7, respectively, at 87% RH. The $f(RH)_{abs}$ also increases continuously with RH, reaching 1.1 at 87%

RH. Since the $f(RH)_{sca} > f(RH)_{ext}$ the SSA increases with RH, from 0.45 for dry particles to 0.52 for particles at 87% RH (***Figure 3-10***).

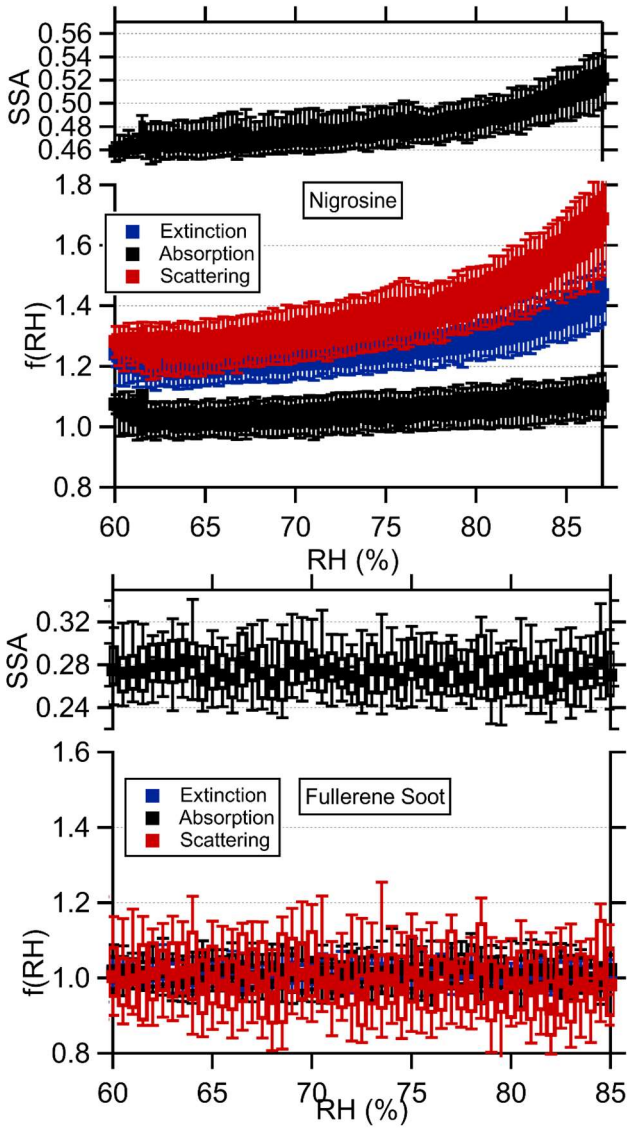

Figure 3-10. (a) The f(RH) for extinction and scattering and SSA for nigrosine particles size selected at 150nm. Extinction increases slowly with RH, with scattering contributing to most of the increase. (b) The f(RH) for extinction and scattering and SSA for fullerene soot particles size-

selected at 200nm. The f(RH) values and the SSA are all constant with RH indicating a lack of water uptake.

The f(RH) values determined here are qualitatively consistent with those derived from the data presented in Brem et al. **(2012)** for nigrosine particles in that the $f(RH)_{sca}$ are greater than the $f(RH)_{ext}$ and the $f(RH)_{abs}$ are observable but small. However, the $f(RH)_{ext}$ and $f(RH)_{sca}$ values here are larger than from Brem et al.**(2012)**. This difference likely reflects their use of polydisperse particles while we used mono-disperse particles. Our $f(RH)_{sca}$ and $f(RH)_{ext}$ values are also somewhat larger than those reported in Carrico et al. **(2021)** and Zhou et al. **(2020)**for size-selected particles. We speculate that their dry reference measurements were not made at sufficiently low RH, leading to measured f(RH) values that are too low, but the difference could also result from operation at different wavelengths (450 nm in Carrico et al. and 532nm in Zhou et al. vs. 630 nm here) or from differences in the truncation correction that was applied (or in the case of Zhou et al., not applied), at least for scattering. Notably, the Carrico et al.**(2021)** instrument does not observe deliquescence behavior for ammonium sulfate, likely owing to differences in design; such behavior could indicate additional factors also contribute to the differences observed here, although we note that nigrosine does not deliquesce. Despite the differences in $f(RH)_{sca}$ and $f(RH)_{ext}$, the $f(RH)_{abs}$ results here are reasonably consistent with those of Carrico et al.**(2021)** and Zhou et al.**(2020)**.

Fullerene soot is effectively non-soluble and hydrophobic. Consistent with this, the f(RH) values for extinction, scattering, and absorption all remain at unity as RH is increased, up to 85% (the highest RH considered). Correspondingly, the SSA remains constant with an average value of 0.28. The constant f(RH) values and SSA indicate that the pure fullerene soot particles do not

uptake water at any subsaturated RH. We are not aware of other studies that have characterized the influence of water uptake on fullerene soot optical properties, but we note that Ohata et al. **(2016)** find negligible water uptake by fullerene soot over a similar RH range. The clearly observable difference in behavior of fullerene soot and nigrosine in terms of the $f(RH)_{abs}$ response to increasing RH demonstrates that the HCAPS developed here is capable of measuring even small absorption enhancements that can result from water uptake.

3.5 Conclusions

In this work we have characterized a new instrument, the HCAPS, that allows for measurement of light absorption, along with scattering and extinction, at elevated relative humidities up to ~90%. The HCAPS combines a CAPS-SSA_{PM}, modified to allow temperature control and stabilization of the optical cell, with an aerosol humidification system. The instrument characterization was facilitated by the development of a general theoretical method to determine the scattering truncation correction factor (C_{ts}) that extends the work of Onasch et al. **(2015)** and Modini et al.**(2021)**. Specifically, our method accounts for the influence of particle growth due to water uptake on the C_{ts} and can be applied to systems with either known or unknown dry particle optical properties (i.e., the complex refractive index) and for either size-selected particles or particle distributions. This is achieved through an iterative methodology that uses measured extinction and scattering cross-sections, and the associated single scatter albedo, for both dry and wet particles to account for the potential influence of multiply-charged particles (for size-selected experiments) and changes in the refractive index from water uptake.

We validated the method using RH-dependent measurements of light extinction and scattering for size-selected, non-absorbing ammonium sulfate particles. The sensitivity of the calculated

truncation correction to the dry particle refractive index was explored by theoretically comparing a non-absorbing system to various absorbing systems (specifically corresponding to nigrosine, fullerene soot, and a highly absorbing aerosol). We show that proper consideration of the dry particle refractive index, and especially changes imposed by water uptake, is necessary to allow for determination of the influence of water uptake on absorption.

Measurements for two absorbing systems, size-selected nigrosine and fullerene soot particles, demonstrated the potential for measuring the influence of water uptake on light absorption specifically. We found that the absorption for nigrosine, which is somewhat soluble, increases modestly upon humidification, with an $f(RH)_{abs}$ ~1.1 at 85% RH. In contrast, the absorption for fullerene soot is unchanged upon humidification up to 85%, reflecting the non-hygroscopic nature of these particles. Comparison between nigrosine and fullerene soot illustrates that water-uptake-induced absorption enhancements can be determined at the level of at least $f(RH)_{abs} = 1.1$. To enhance generalizability, future studies could include more representative aerosol analogs and varied conditions including mixing state.

The results presented here demonstrate that it is possible to measure relatively small absorption enhancements for absorbing aerosol systems. Future efforts should aim to establish how mixing of non-absorbing and absorbing, hygroscopic and non-hygroscopic, and solid and non-solid components affects the water-driven absorption enhancement. Moreover, laboratory investigation must be complemented by field observations of the influence of water uptake on absorption to guide updates to models that predict and quantify global aerosol absorption and the impacts on climate. The HCAPS can be deployed *in situ* to measure the absorption enhancement due to increased relative humidity on ambient aerosol samples. Complementing laboratory

experiment findings with field observations and modeling efforts can bridge the gap between controlled experiments and real-world applications.

3.6 Acknowledgements

The authors thank Jesse Kroll (MIT) for the use of the CAPS-PMSSA and Tim Onasch and Andy Freedman (Aerodyne Research) for technical support and guidance.

3.7 Funding

R. Dal Porto, N. Wang, and C. D. Cappa were supported by of the US Department of Energy (DOE) Office of Biological and Environmental Research (OBER), Atmospheric System Research (ASR) Program through Grant No. DE-SC0020182.

3.8 REFERENCES

Baynard, T., Garland, R.M., Ravishankara, A.R., Tolbert, M.A., and Lovejoy, E.R. (2006). Key factors influencing the relative humidity dependence of aerosol light scattering. *Geophys. Res. Lett.* 33 (6). doi:10.1029/2005GL024898.

Bond, T.C., Doherty, S.J., Fahey, D.W., Forster, P.M., Berntsen, T., DeAngelo, B.J., Flanner, M.G., Ghan, S., Kärcher, B., Koch, D., Kinne, S., Kondo, Y., Quinn, P.K., Sarofim, M.C., Schultz, M.G., Schulz, M., Venkataraman, C., Zhang, H., Zhang, S., Bellouin, N., Guttikunda, S.K., Hopke, P.K., Jacobson, M.Z., Kaiser, J.W., Klimont, Z., Lohmann, U., Schwarz, J.P., Shindell, D., Storelvmo, T., Warren, S.G., and Zender, C.S. (2013). Bounding the role of black carbon in the climate system: A scientific assessment. *J. Geophys. Res. Atmospheres* 118 (11):5380–5552. doi:10.1002/jgrd.50171.

Bond, T.C., Habib, G., and Bergstrom, R.W. (2006). Limitations in the enhancement of visible light absorption due to mixing state. *J. Geophys. Res. Atmospheres* 111 (D20). doi:10.1029/2006JD007315.

Brem, B.T., Mena Gonzalez, F.C., Meyers, S.R., Bond, T.C., and Rood, M.J. (2012). Laboratory-Measured Optical Properties of Inorganic and Organic Aerosols at Relative Humidities up to 95%. *Aerosol Sci. Technol.* 46 (2):178–190. doi:10.1080/02786826.2011.617794.

Cappa, C.D., Lack, D.A., Burkholder, J.B., and Ravishankara, A.R. (2008). Bias in Filter-Based Aerosol Light Absorption Measurements Due to Organic Aerosol Loading: Evidence from Laboratory Measurements. *Aerosol Sci. Technol.* 42 (12):1022–1032. doi:10.1080/02786820802389285.

Cappa, C.D., Onasch, T.B., Massoli, P., Worsnop, D.R., Bates, T.S., Cross, E.S., Davidovits, P., Hakala, J., Hayden, K.L., Jobson, B.T., Kolesar, K.R., Lack, D.A., Lerner, B.M., Li, S.-M., Mellon, D., Nuaaman, I., Olfert, J.S., Petäjä, T., Quinn, P.K., Song, C., Subramanian, R., Williams, E.J., and Zaveri, R.A. (2012). Radiative Absorption Enhancements Due to the Mixing State of Atmospheric Black Carbon. *Science* 337 (6098):1078–1081. doi:10.1126/science.1223447.

Carrico, C.M., Capek, T.J., Gorkowski, K.J., Lam, J.T., Gulick, S., Karacaoglu, J., Lee, J.E., Dungan, C., Aiken, A.C., Onasch, T.B., Freedman, A., Mazzoleni, C., and Dubey, M.K. (2021). Humidified single-scattering albedometer (H-CAPS-PMSSA): Design, data analysis, and validation. *Aerosol Sci. Technol.* 0 (0):1–20. doi:10.1080/02786826.2021.1895430.

Cui, X., Wang, X., Yang, L., Chen, B., Chen, J., Andersson, A., and Gustafsson, Ö. (2016). Radiative absorption enhancement from coatings on black carbon aerosols. *Sci. Total Environ.* 551–552:51–56. doi:10.1016/j.scitotenv.2016.02.026.

Erlick, C., Abbatt, J.P.D., and Rudich, Y. (2011). How Different Calculations of the Refractive Index Affect Estimates of the Radiative Forcing Efficiency of Ammonium Sulfate Aerosols. *J. Atmospheric Sci.* 68 (9):1845–1852. doi:10.1175/2011JAS3721.1.

Fierce, L., Bond, T.C., Bauer, S.E., Mena, F., and Riemer, N. (2016). Black carbon absorption at the global scale is affected by particle-scale diversity in composition. *Nat. Commun.* 7 (1):12361. doi:10.1038/ncomms12361.

Fuller, K.A. (1995). Scattering and absorption cross sections of compounded spheres. II. Calculations for external aggregation. *JOSA A* 12 (5):881–892. doi:10.1364/JOSAA.12.000881.

Fuller, K.A., Malm, W.C., and Kreidenweis, S.M. (1999). Effects of mixing on extinction by carbonaceous particles. *J. Geophys. Res. Atmospheres* 104 (D13):15941–15954. doi:10.1029/1998JD100069.

Ghan, S.J., Liu, X., Easter, R.C., Zaveri, R., Rasch, P.J., Yoon, J.-H., and Eaton, B. (2012). Toward a Minimal Representation of Aerosols in Climate Models: Comparative Decomposition of Aerosol Direct, Semidirect, and Indirect Radiative Forcing. *J. Clim.* 25 (19):6461–6476. doi:10.1175/JCLI-D-11-00650.1.

Jacobson, M.Z. (2012). Investigating cloud absorption effects: Global absorption properties of black carbon, tar balls, and soil dust in clouds and aerosols. *J. Geophys. Res. Atmospheres* 117 (D6). doi:10.1029/2011JD017218.

Jacobson, M.Z. (2001). Strong radiative heating due to the mixing state of black carbon in atmospheric aerosols. *Nature* 409 (6821):695–697. doi:10.1038/35055518.

Khalizov, A.F., Xue, H., Wang, L., Zheng, J., and Zhang, R. (2009). Enhanced Light Absorption and Scattering by Carbon Soot Aerosol Internally Mixed with Sulfuric Acid. *J. Phys. Chem. A* 113 (6):1066–1074. doi:10.1021/jp807531n.

Knox, A., Evans, G.J., Brook, J.R., Yao, X., Jeong, C.-H., Godri, K.J., Sabaliauskas, K., and Slowik, J.G. (2009). Mass Absorption Cross-Section of Ambient Black Carbon Aerosol in Relation to Chemical Age. *Aerosol Sci. Technol.* 43 (6):522–532. doi:10.1080/02786820902777207.

Lack, D.A. and Cappa, C.D. (2010). Impact of brown and clear carbon on light absorption enhancement, single scatter albedo and absorption wavelength dependence of black carbon. *Atmospheric Chem. Phys.* 10 (9):4207–4220. doi:10.5194/acp-10-4207-2010.

Lack, D.A., Cappa, C.D., Covert, D.S., Baynard, T., Massoli, P., Sierau, B., Bates, T.S., Quinn, P.K., Lovejoy, E.R., and Ravishankara, A.R. (2008). Bias in Filter-Based Aerosol Light Absorption Measurements Due to Organic Aerosol Loading: Evidence from Ambient Measurements. *Aerosol Sci. Technol.* 42 (12):1033–1041. doi:10.1080/02786820802389277.

Lack, D.A., Langridge, J.M., Bahreini, R., Cappa, C.D., Middlebrook, A.M., and Schwarz, J.P. (2012). Brown carbon and internal mixing in biomass burning particles. *Proc. Natl. Acad. Sci.* 109 (37):14802–14807. doi:10.1073/pnas.1206575109.

Laskin, A., Laskin, J., and Nizkorodov, S.A. (2015). Chemistry of Atmospheric Brown Carbon. *Chem. Rev.* 115 (10):4335–4382. doi:10.1021/cr5006167.

Li, J., Carlson, B.E., Yung, Y.L., Lv, D., Hansen, J., Penner, J.E., Liao, H., Ramaswamy, V., Kahn, R.A., Zhang, P., Dubovik, O., Ding, A., Lacis, A.A., Zhang, L., and Dong, Y. (2022). Scattering and absorbing aerosols in the climate system. *Nat. Rev. Earth Environ.* 3 (6):363–379. doi:10.1038/s43017-022-00296-7.

Liu, F., Snelling, D.R., Thomson, K.A., and Smallwood, G.J. (2018). Estimate of scattering truncation in the cavity attenuated phase shift PMSSA monitor using radiative transfer theory. *Aerosol Sci. Technol.* 52 (5):588–596. doi:10.1080/02786826.2018.1437891.

Liu, X., Huey, L.G., Yokelson, R.J., Selimovic, V., Simpson, I.J., Müller, M., Jimenez, J.L., Campuzano-Jost, P., Beyersdorf, A.J., Blake, D.R., Butterfield, Z., Choi, Y., Crounse, J.D., Day, D.A., Diskin, G.S., Dubey, M.K., Fortner, E., Hanisco, T.F., Hu, W., King, L.E., Kleinman, L., Meinardi, S., Mikoviny, T., Onasch, T.B., Palm, B.B., Peischl, J., Pollack, I.B., Ryerson, T.B., Sachse, G.W., Sedlacek, A.J., Shilling, J.E., Springston, S., Clair, J.M.S., Tanner, D.J., Teng, A.P., Wennberg, P.O., Wisthaler, A., and Wolfe, G.M. (2017). Airborne measurements of western U.S. wildfire emissions: Comparison with prescribed burning and air quality implications. *J. Geophys. Res. Atmospheres* 122 (11):6108–6129. doi:https://doi.org/10.1002/2016JD026315.

Lund, M.T., Myhre, G., Haslerud, A.S., Skeie, R.B., Griesfeller, J., Platt, S.M., Kumar, R., Myhre, C.L., and Schulz, M. (2018). Concentrations and radiative forcing of anthropogenic aerosols from 1750 to 2014 simulated with the Oslo CTM3 and CEDS emission inventory. *Geosci. Model Dev.* 11 (12):4909–4931. doi:10.5194/gmd-11-4909-2018.

McMeeking, G.R., Fortner, E., Onasch, T.B., Taylor, J.W., Flynn, M., Coe, H., and Kreidenweis, S.M. (2014). Impacts of nonrefractory material on light absorption by aerosols emitted from biomass burning. *J. Geophys. Res. Atmospheres* 119 (21):12,272-12,286. doi:https://doi.org/10.1002/2014JD021750.

Mikhailov, E.F., Vlasenko, S.S., Podgorny, I.A., Ramanathan, V., and Corrigan, C.E. (2006). Optical properties of soot–water drop agglomerates: An experimental study. *J. Geophys. Res. Atmospheres* 111 (D7). doi:10.1029/2005JD006389.

Modini, R.L., Corbin, J.C., Brem, B.T., Irwin, M., Bertò, M., Pileci, R.E., Fetfatzis, P., Eleftheriadis, K., Henzing, B., Moerman, M.M., Liu, F., Müller, T., and Gysel-Beer, M. (2021). Detailed characterization of the CAPS single-scattering albedo monitor (CAPS PMssa) as a field-deployable instrument for measuring aerosol light absorption with the extinction-minus-scattering method. *Atmospheric Meas. Tech.* 14 (2):819–851. doi:10.5194/amt-14-819-2021.

Moffet, R.C. and Prather, K.A. (2009). In-situ measurements of the mixing state and optical properties of soot with implications for radiative forcing estimates. *Proc. Natl. Acad. Sci.* 106 (29):11872–11877. doi:10.1073/pnas.0900040106.

Ohata, S., Schwarz, J.P., Moteki, N., Koike, M., Takami, A., and Kondo, Y. (2016). Hygroscopicity of materials internally mixed with black carbon measured in Tokyo. *J. Geophys. Res. Atmospheres* 121 (1):362–381. doi:10.1002/2015JD024153.

Onasch, T.B., Massoli, P., Kebabian, P.L., Hills, F.B., Bacon, F.W., and Freedman, A. (2015). Single Scattering Albedo Monitor for Airborne Particulates. *Aerosol Sci. Technol.* 49 (4):267–279. doi:10.1080/02786826.2015.1022248.

Peng, J., Hu, M., Guo, S., Du, Z., Zheng, Jing, Shang, D., Levy Zamora, M., Zeng, L., Shao, M., Wu, Y.-S., Zheng, Jun, Wang, Y., Glen, C.R., Collins, D.R., Molina, M.J., and Zhang, R. (2016). Markedly enhanced absorption and direct radiative forcing of black carbon under polluted urban environments. *Proc. Natl. Acad. Sci.* 113 (16):4266–4271. doi:10.1073/pnas.1602310113.

Saliba, G., Subramanian, R., Saleh, R., Ahern, A.T., Lipsky, E.M., Tasoglou, A., Sullivan, R.C., Bhandari, J., Mazzoleni, C., and Robinson, A.L. (2016). Optical properties of black carbon in cookstove emissions coated with secondary organic aerosols: Measurements and modeling. *Aerosol Sci. Technol.* 50 (11):1264–1276. doi:10.1080/02786826.2016.1225947.

Scarnato, B.V., Vahidinia, S., Richard, D.T., and Kirchstetter, T.W. (2013). Effects of internal mixing and aggregate morphology on optical properties of black carbon using a discrete dipole approximation model. *Atmospheric Chem. Phys.* 13 (10):5089–5101. doi:10.5194/acp-13-5089-2013.

Schnaiter, M., Linke, C., Möhler, O., Naumann, K.-H., Saathoff, H., Wagner, R., Schurath, U., and Wehner, B. (2005). Absorption amplification of black carbon internally mixed with secondary organic aerosol. *J. Geophys. Res. Atmospheres* 110 (D19). doi:10.1029/2005JD006046.

Seinfeld, J.H. and Pandis, S.N. (2016). Atmospheric Chemistry and Physics: From Air Pollution to Climate Change. John Wiley & Sons.

Szopa, S., Naik, V., Adhikary, B., Artaxo, P., Berntsen, T., Collins, W.D., Fuzzi, S., Gallardo, L., Kiendler-Scharr, A., Klimont, Z., Liao, H., Unger, N., and Zanis, P. (2023). Short-Lived Climate Forcers. In Climate Change 2021: The Physical Science Basis. Contribution of Working Group I to the Sixth Assessment Report of the Intergovernmental Panel on Climate Change, 1st ed. Cambridge University Press.

Williams, A.I.L., Stier, P., Dagan, G., and Watson-Parris, D. (2022). Strong control of effective radiative forcing by the spatial pattern of absorbing aerosol. *Nat. Clim. Change* 12 (8):735–742. doi:10.1038/s41558-022-01415-4.

Xie, C., Xu, W., Wang, J., Liu, D., Ge, X., Zhang, Q., Wang, Q., Du, W., Zhao, J., Zhou, W., Li, J., Fu, P., Wang, Z., Worsnop, D., and Sun, Y. (2019). Light absorption enhancement of black carbon in urban Beijing in summer. *Atmos. Environ.* 213:499–504. doi:10.1016/j.atmosenv.2019.06.041.

You, R., Radney, J.G., Zachariah, M.R., and Zangmeister, C.D. (2016). Measured Wavelength-Dependent Absorption Enhancement of Internally Mixed Black Carbon with Absorbing and Nonabsorbing Materials. *Environ. Sci. Technol.* 50 (15):7982–7990. doi:10.1021/acs.est.6b01473.

Zarzana, K.J., Cappa, C.D., and Tolbert, M.A. (2014). Sensitivity of Aerosol Refractive Index Retrievals Using Optical Spectroscopy. *Aerosol Sci. Technol.* 48 (11):1133–1144. doi:10.1080/02786826.2014.963498.

Zhang, R., Khalizov, A.F., Pagels, J., Zhang, D., Xue, H., and McMurry, P.H. (2008). Variability in morphology, hygroscopicity, and optical properties of soot aerosols during atmospheric processing. *Proc. Natl. Acad. Sci.* 105 (30):10291–10296. doi:10.1073/pnas.0804860105.

Zhou, J., Xu, X., Zhao, W., Fang, B., Liu, Q., Cai, Y., Zhang, W., Venables, D.S., and Chen, W. (2020). Simultaneous measurements of the relative-humidity-dependent aerosol light extinction, scattering, absorption, and single-scattering albedo with a humidified cavity-enhanced albedometer. Atmospheric Meas. Tech. 13 (5):2623–2634. doi:10.5194/amt-13-2623-2020.

3.9 Supplemental Materials for: Development and validation of a humidified CAPS-PMSSA with an improved methodology to calculate truncation correction factor

3.9.1 S1. Instrument Performance

The HCAPS system relies on water temperature and a dry and humidified line to control the RH of the aerosol flow. Figure S1 shows the responsivity of the system to programmed rapid switching between the dry and humidified line with clean air (particle free) flow. There are two RH probes in the system as described in the main text, one located right before the outlet of the RH box, and another at the outlet of the CAPS. The measured RH in both the CAPS and the RH Box respond quickly to switches between the dry and humidified lines.

3.9.2 S2. Ammonium Sulfate Truncation Correction Validation

The differential mobility analyzer size selects particles from an air stream using the particles electrical mobility diameter. The electrical mobility diameter is inversely proportional to particle size, and can be described by Equation S1.

$$Zp = \frac{veC(Dp)}{3\pi\mu Dp} \qquad \textit{Equation S1}$$

Zp = Electrical mobility

C(Dp) = Cunningham slip correction factor

v = Number of elementary charges

e = Elementary charge

μ = Air Dynamic Viscosity

Dp = Physical Diameter

Since we are interested in the particle's physical diameter as that is the parameter that influences optical properties, the size selected diameter we choose has to be converted from physical diameter

to electrical mobility diameter. Singly, doubly, triply, and higher number of charge carrying particles may make it through to the monodisperse aerosol flow. These particles will have the same electrical mobility diameter, but larger physical diameters than the singly charged particle of interest. This causes an overestimation of light extinction attributed to the selected diameter.

To account for the presence of multiply charged particles, the extinction measurement from the HCAPS system was used to determine an effective particle diameter to use, rather than the selected diameter. The extinction cross section for a range of particles of known composition were calculated using Mie Theory with the refractive index of ammonium sulfate. Then, the measured extinction cross section was cross referenced to the resultant array, and the effective diameter associated with the closest match was used.

Figure S2 shows the measured ammonium sulfate without multiple charge correction vs the truncation correction factor (C_{ts}) without glass included. The apparent measurement validation is biased low in comparison to the modeled truncation. The inclusion of scattering off the inner glass tube brings the truncation correction factor down slightly, while the incorporation of an effective diameter brings the measured ammonium sulfate SSA up, causing the measured and modelled to better converge as is seen in the main text.

3.9.3 S3. Theoretical Truncation Correction Factor Matrix

To constrain (*n,k*) pairs to reasonably characterize potential aerosol complex refractive indices, we assumed a linear relationship between n and k spanning from a non-absorbing aerosol, ammonium sulfate, to a highly absorbing aerosol, BC. The refractive index assumed for ammonium sulfate was 1.54 + 0k , for BC it was 1.8 + 1k as a reasonably midpoint for current literature values of BC **(Liu et al. 2020; Bond and Bergstrom 2006)**. In the computational

implementation we use 110 linearly spaced (*n,k*) pairs. This reasonably captures the range of refractive indices seen in common aerosols **(Zarzana et al. 2014)**. The linear relationship and associated fit are shown in Figure S4.

References

Bond, T.C. and Bergstrom, R.W. (2006). Light Absorption by Carbonaceous Particles: An Investigative Review. *Aerosol Science and Technology* 40 (1):27–67. doi:10.1080/02786820500421521.

Corbin, J.C., Czech, H., Massabò, D., de Mongeot, F.B., Jakobi, G., Liu, F., Lobo, P., Mennucci, C., Mensah, A.A., Orasche, J., Pieber, S.M., Prévôt, A.S.H., Stengel, B., Tay, L.-L., Zanatta, M., Zimmermann, R., El Haddad, I., and Gysel, M. (2019). Infrared-absorbing carbonaceous tar can dominate light absorption by marine-engine exhaust. *npj Clim Atmos Sci* 2 (1):1–10. doi:10.1038/s41612-019-0069-5.

Liu, F., Yon, J., Fuentes, A., Lobo, P., Smallwood, G.J., and Corbin, J.C. (2020). Review of recent literature on the light absorption properties of black carbon: Refractive index, mass absorption cross section, and absorption function. *Aerosol Science and Technology* 54 (1):33–51. doi:10.1080/02786826.2019.1676878.

Zarzana, K.J., Cappa, C.D., and Tolbert, M.A. (2014). Sensitivity of Aerosol Refractive Index Retrievals Using Optical Spectroscopy. *Aerosol Science and Technology* 48 (11):1133–1144. doi:10.1080/02786826.2014.963498.

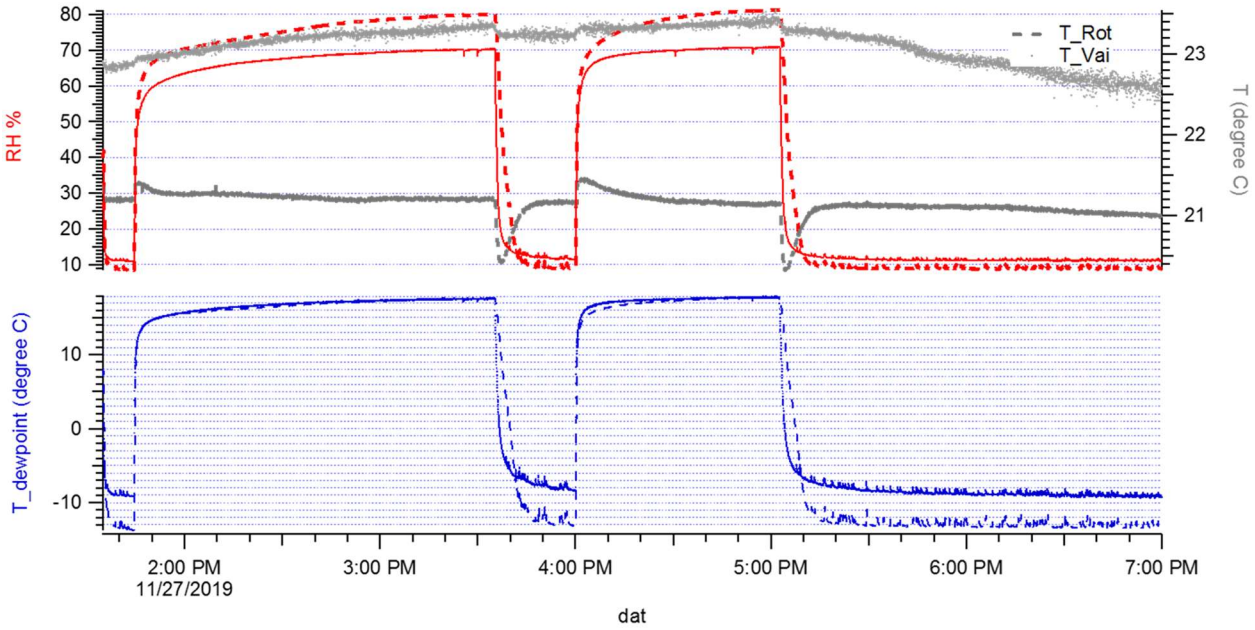

*Figure S**3-1**. Instrument RH responsivity to rapid switching between the dry and humidified lines when no particles are present in the air stream. T_rot represents the temperature measured in the CAPS cell, while T_vai represents the temperature measured in the outlet of the RH Box preceding the CAPS instrument.*

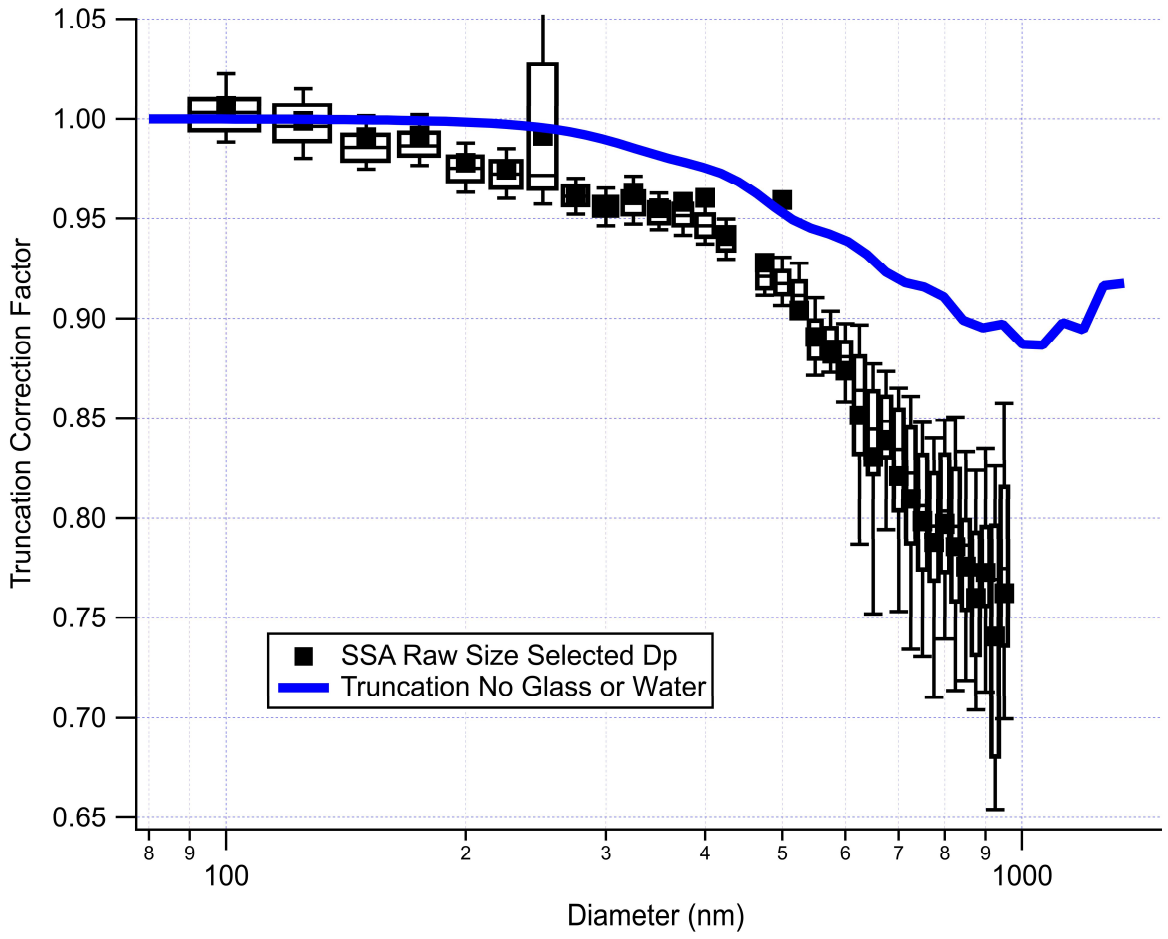

Figure S3-2. Truncation factor comparison with raw SSA prior to corrections. The truncation correction presented with the solid line does not include reflection off the glass tubing, nor does it account for water uptake and humidification. The raw SSA presented does not account for multiple charged particles.

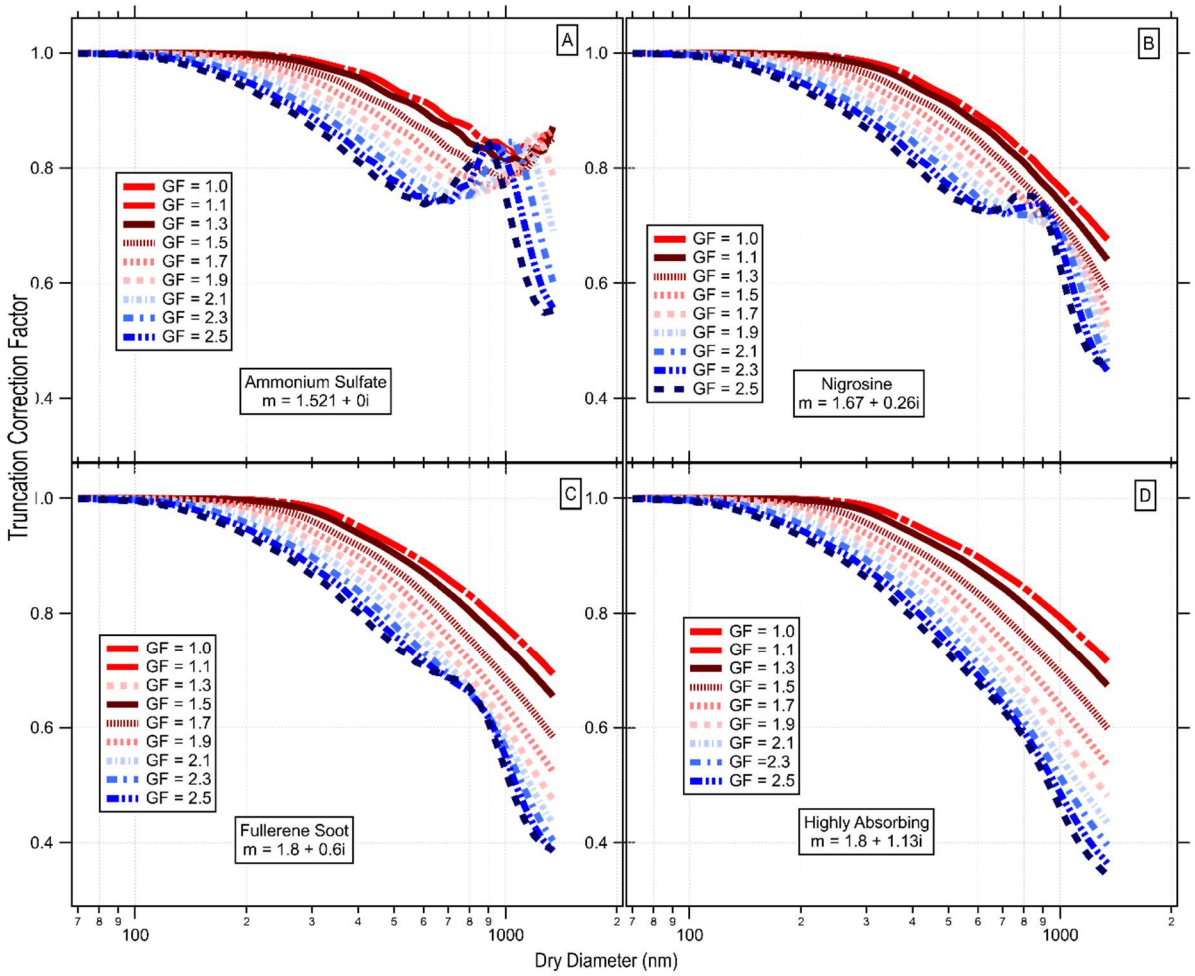

Figure S3-3. Modeled truncation correction factor curves plotted against dry diameter and for multiple growth factors for four different compositions. The tiles increase in absorptivity from A-D. (A) shows the truncation for ammonium sulfate, (B) for nigrosine, (C) for fullerene, (D) for a highly absorbing aerosol.

4 Absorption by Black Carbon, Brown Carbon, and Dust Aerosols During the TRACER Field Campaign in Houston, TX in July 2022

Authors: Rachael Dal Porto[1], Kyle Gorkowski[2], James E. Lee[2], Ryan N. Farley[2,3,4], Zewen Zheng[3], Katherine B. Benedict[2], Allison C. Aiken[2], Manvendra K. Dubey[2], Qi Zhang[3,4], Christopher D. Cappa[1]

[1]Department of Civil and Environmental Engineering, University of California, Davis, CA, 95616 USA

[2]Earth and Environmental Sciences Division, Los Alamos National Laboratory, Los Alamos, NM, USA

[3]Agricultural and Environmental Chemistry Graduate Group, University of California Davis, CA, 95616, USA

[4]Department of Environmental Toxicology, University of California Davis, CA, 95616, USA

CONTACT Christopher D. Cappa cdcappa@ucdavis.edu

Abstract

Absorbing aerosols, including black carbon (BC), brown carbon (BrC), and dust, play a critical role in atmospheric processes by altering the Earth's radiative balance. This study examines aerosol optical properties in Houston, Texas, during the TRacking Aerosol Convection Interactions ExpeRiment (TRACER) campaign in July 2022. Measurements were conducted using a suite of instruments to characterize particle composition, size distributions, water uptake, and light absorption and extinction at 405nm and 532nm. Mass absorption coefficients (MAC) were determined for BC, dust, and organic aerosol (i.e., absorption by BrC), with derived MAC values of 8.5 ± 0.2 $m^2 g^{-1}$ at 532nm and 11.1 ± 0.5 $m^2 g^{-1}$ at 405nm for black carbon, 0.036 ± 0.002 $m^2 g^{-1}$ (532 nm) and 0.128 ± 0.005 $m^2 g^{-1}$ (405 nm) for dust, and 0.20 ± 0.04 $m^2 g^{-1}$ (532 nm) and 0.2 ± 0.1 $m^2 g^{-1}$ (405 nm) for organic aerosols. On average, the fraction of absorption attributable to BC, dust, and BrC at 405 nm was 0.61, 0.34, and 0.06, respectively, and at 532 nm was 0.75, 0.16, and 0.09, respectively. Additionally, the imaginary component of the refractive index (k) for dust was retrieved and determined to be $k = 0.0040i$ at 405 nm, $k = 0.0016i$ at 532 nm.

4.1 Introduction

Absorbing aerosols, including black carbon (BC), brown carbon (BrC), and dust, influence Earth's climate through their direct interactions with solar radiation and their indirect influence on cloud properties (Lambe et al. 2015). BC is primarily emitted during the incomplete combustion of fossil fuels and biomass and significantly affects global climate due to its strong light-absorbing properties (Intergovernmental Panel On Climate Change 2023; Bond et al. 2013; Ramanathan and Carmichael 2008; Jacobson 2001). BrC corresponds to a broad category of organic aerosols that exhibit light-absorbing properties in the visible and ultraviolet (UV) regions

of the spectrum. BrC encompasses a variety of different compounds and substances with diverse chemical compositions and properties, and is believed to mainly originate from biomass burning and secondary organic aerosol formation (Laskin et al. 2015) or nitration of organics (Mohr et al 2013) Dust aerosols are generated through mechanical processes (e.g., wind action) and exhibit varying optical properties (Li et al. 2021; Rodriguez-Navarro et al. 2018; Kok et al. 2014).

The optical characteristics of absorbing aerosols are determined by their size, morphology, composition, and mixing state. BC aggregate formation and optical properties are shaped by atmospheric aging, and they exhibit enhanced light absorption when mixed with other aerosol types (Cappa et al. 2012, 2019; Schnaiter et al. 2003) . BrC is less absorbing than BC, and the optical properties of BrC vary substantially depending on the source and aging processes (Cappa et al. 2019; Laskin et al. 2015; Lack et al. 2012; Andreae and Gelencsér 2006). However, because the concentration of organic aerosol is typically much larger than BC, its contribution to regional and global radiative forcing is significant (Zhang et al. 2017; Ramanathan et al. 2005). Dust particles, with their varying sizes and compositions, show significant differences in radiative effects based on their origin and atmospheric interactions (Kok et al. 2014).

Houston, TX, USA is influenced by a diverse set of aerosols, including BC, BrC, and dust, that originate from a variety of local and far-field sources. Local sources include vehicles, ship traffic, petroleum processing, and chemical manufacturing that can be studied to address gaps in understanding of regional impacts from these aerosols. Houston is also seasonally affected by aged dust plumes that originate from the Sahara Desert in Africa, whose properties and aging represent a significant uncertainty in climate models. Additionally, in the subtropical climate, high humidity, high incoming solar radiation, and frequent convective storms affects aerosol hygroscopic growth and mixing state, another process driving uncertainty in aerosol budget

affecting atmospheric lifetime and optical properties that also interacts with the local urban/industrial emissions(Al-Naiema et al. 2018; Zhang et al. 2017; Ramanathan et al. 2005). This study addresses these gaps by investigating aerosol events observed during the TRACER campaign, focusing on how the local conditions and complex emission sources in Houston influence the absorption characteristics of BC, BrC, and dust. In this paper we discuss three distinct types of aerosol events observed during the campaign and will describe the contributions of black carbon, brown carbon, and dust to absorption in the region. This study also aims to investigate the optical properties of aerosols measured during the TRACER campaign, with a particular focus on the contributions of dust and the limited evidence of BrC presence. Furthermore, we will assess aerosol hygroscopicity variability.

4.2 TRACER Campaign and Measurement Methods

The Department of Energy (DOE) Atmosphere Systems Research (ASR) TRacking Aerosol Convection ExpeRiment (TRACER) was an observational field campaign in Houston, TX, conducted to investigate the interactions between aerosols, convection, and cloud formation within the urban environment. Measurements during TRACER were made at three locations across the Houston area; here, we focus on measurements made at the AMF1 main site located at the La Porte Municipal Airport, La Porte, Tx. A wide range of aerosol- and gas-phase measurements were made during TRACER at the AMF1 site. Here, we focus on measurements made during the Carbonaceous Aerosols Thrust (TRACER-CAT) sub-campaign over the period July 1 to July 31, 2022.

The La Porte site is situated about 30 kilometers east-southeast of downtown Houston and is near major industrial and coastal environments and activities. The site is approximately 3 miles from the Houston Ship Channel in Galveston Bay, a major estuary linked to the Gulf of Mexico with

ship traffic into and out of the Port of Houston, one of the most heavily trafficked port in the U.S. by tonnage ("Port Statistics" n.d.). Additionally, the region surrounding La Porte hosts numerous petrochemical plants and refineries, placing it in an area with substantial industrial emissions. Lastly, there is extensive transportation infrastructure surrounding the site, including State Highway 225 and Interstate 45 contributing to vehicular emissions, *Figure 4-1* shows a map of the site and surrounding land uses.

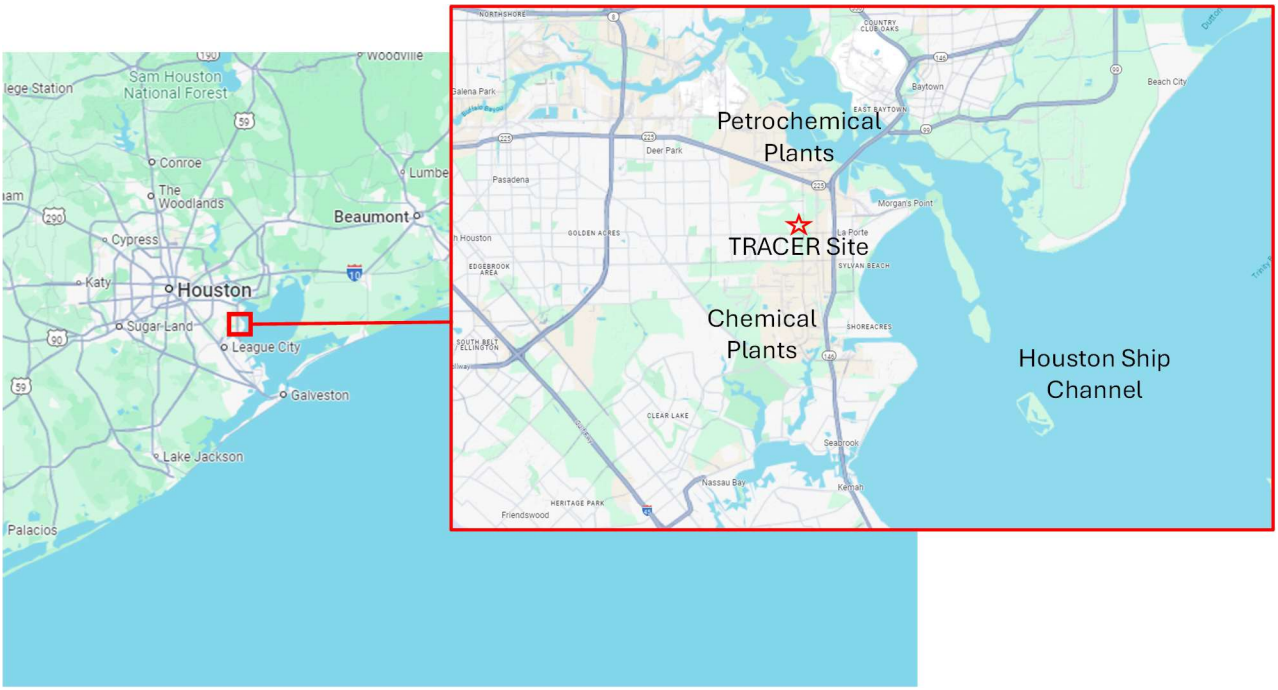

Figure 4-1. Map of TRACER site showing surrounding features that produce unique aerosol emissions.

Climatologically, La Porte has a subtropical climate, defined by hot, humid weather and frequent thunderstorms in the summer. The average temperature during the campaign was 29 ± 3°C, with relative humidity averaging 72 ± 13%, both exhibiting strong diurnal variations. Several heavy precipitation events occurred during the measurement period. These were generally brief, rarely

persisting for more than a few hours. Wind patterns displayed a consistent diurnal profile, with weak southerly to southwesterly winds (< 2 m/s) overnight and stronger southeasterly winds (> 5 m/s) in the afternoon (Farley et al. 2024). The consistent diurnal wind patterns, influenced by the boundary layer height and sea-breeze effect, result in the transport of marine or processed air masses during the day. This dynamic meteorological setting, coupled with industrial and urban emissions, as well as long range transport from the Saharan desert, which is regularly observed, provides a unique context for investigating the impact of absorbing aerosols, such as BC, BrC, and dust, on local and regional air quality and climate (Li et al. 2020; Banta 2008).

4.3 Description of Instrumentation

During the TRACER campaign, detailed measurements of BC, BrC, and dust were made using a combination of optical, chemical, and physical aerosol characterization techniques. All instruments were co-located in a temperature-controlled mobile facility that was built as a customized aerosol observation system by LANL. Air was sampled from 10 m above the ground through a common inlet. The sampled air was split to pass either through a $PM_{2.5}$ cyclone or to an aerodynamic particle sizer (APS). Both air streams were passed through Perma Pure monotube driers (MD-700) to reduce the relative humidity and then sampled to the various instrumentation. An additional drier was added on July 14th at 07:00 inline upstream of select instrumentation to further reduce the relative humidity (see *Figure S**4-1**Figure S**4-1**:*). All data were synchronized to a common time reference, and the reported measurements were averaged over 30-minute intervals. Figure S1 shows a scheme of the configuration of instruments in the trailer.

4.4 Optical Property Measurements

Optical properties were measured using a combination of cavity ringdown spectroscopy (CRDS) and photoacoustic spectroscopy (PAS), which were integrated into a single system (the UC Davis CRD-PAS (Cappa et al. 2012; Lack et al. 2012; Langridge et al. 2011)). Light extinction coefficients (b_{ext}) were measured at two wavelengths, 405 nm and 532 nm, using CRDS. The b_{ext} coefficients were measured at both wavelengths for dry particles. Initially, drying of the aerosol stream was limited to an RH of 45% ± 5% from July 1-13. Improvements to the sample preparation on July 14 reduced the dry RH to 29% ± 3% for data collected July 14-31. Light extinction was measured at 532 nm for humidified particles, with an average humidified RH of 88% ± 2% obtained by passing the sampled, dried air through Nafion humidifiers (Perma Pure MD-110-12). Light absorption coefficients (b_{abs}) were measured at 405 nm and 532 nm for dry particles using PAS. The PAS was calibrated prior to the campaign by measuring the PAS response to NO_2 in air and referencing this to concurrent measurements of b_{ext}. Scattering coefficients (b_{sca}) were determined as $b_{sca} = b_{ext} - b_{abs}$. To minimize the potential for interference in the b_{ext} and b_{abs} aerosol measurements from gas-phase component the airstream entering the CRD-PAS was sampled through a charcoal-cloth lined denuder. Additionally, continuous measurements of b_{ext} coefficients for filtered air samples were made at both wavelengths and indicated negligible absorption by gas-phase component. The CRD-PAS was zeroed for 3 minutes out of every 30 minutes by sampling filtered air. Relative humidity in the CRD cells was monitored using Vaisala RH probes that were calibrated using saturated salt solutions. The wavelength-dependent single scatter albedo (*SSA*) is derived from the extinction and absorption measurements as $SSA = (b_{ext} - b_{abs})/b_{ext}$. The wavelength dependence of extinction,

scattering, and absorption are characterized by their Ångstrom exponents (the *EAE*, *SAE*, *AAE*, respectively), calculated as

$$EAE = -\log\left(\frac{b_{ext,405nm}}{b_{ext,532nm}}\right) / \log\left(\frac{405\ nm}{532\ nm}\right) \quad (1.)$$

and with a similar expression based on b_{sca} for the SAE and the b_{abs} values for the *AAE*. *AAE* values close to unity generally indicate that absorption is dominated by BC (Bond and Bergstrom 2006) while larger values can indicate an influence from either BrC or dust. *EAE* values larger than unity generally indicate that extinction is dominated by smaller particles (<1 μm or so) while smaller values indicate that extinction is dominated by larger particles (>1 μm) (Cappa et al. 2016).

4.5 Size Distribution Measurements

Size distributions for dry particles were measured using a scanning electrical mobility spectrometer (SEMS; Brechtel Model 2002) and an aerodynamic particle sizer (APS; TSI Model 3321). The SEMS characterized particles by their electrical mobility diameters ($D_{p,m}$) over the range 10-1340 nm; problems with arcing later identified in the system when operating at higher voltages ultimately limited the SEMS size range to <800 nm. The SEMS was located behind the $PM_{2.5}$ cyclone The APS characterized particles by their aerodynamic diameter ($D_{p,a}$) over the range 0.5 to 20 μm. The APS was not located behind the PM2.5 cyclone. To facilitate comparison with the optical property and composition measurements, only particles with vacuum aerodynamic diameters ($D_{p,a}$) less than 2.5 μm are considered here, which corresponds to an equivalent $D_{p,m}$ = 1.8 μm, assuming spherical particles and a particle density of 2.0 g cm^{-3}. Under an assumption of spherical particles the mobility diameter is equivalent to the physical diameter

appropriate for optical property calculations. The SEMS and APS size distributions were merged by converting the APS diameters from aerodynamic to mobility-equivalent, assuming a particle density of 2.0 g cm^3.

4.6 Composition Measurements

Particle composition was measured using two high-resolution soot particle aerosol mass spectrometers (SP-AMS) to analyze refractory black carbon (rBC) and its associated coating material using the ensemble size-resolved mass spectral mode and the event trigger single particle (ETSP) mode. The two SP-AMS instruments used here were operated in different configurations. In one, the SP-AMS included only a laser vaporizer. This "laser only" SP-AMS selectively characterizes only those particles that contain BC. In the other, the SP-AMS included both a laser vaporizer and a thermal vaporizer. This "laser-thermal" SP-AMS characterizes all non-refractory (NR) components, such as sulfate, nitrate, organics (OA), ammonium and chloride, independent of whether they are internally mixed with BC. Additionally, the laser-only SP-AMS was equipped with a standard aerodynamic lens, limiting its measurements to submicron particles (PM_1), whereas the laser-thermal SP-AMS was equipped with a $PM_{2.5}$ lens, enabling it to analyze larger particles.

Spectral interpretation of AMS data was performed using the SQUIRREL/PIKA software package developed in Igor (Wavemetrics) by Aerodyne Research Inc. Ion concentrations are determined from the high-resolution peak fitting, with concentrations reported in nitrate-equivalent mass. The instrument sensitivity was calibrated at the beginning and end of the campaign using ammonium-nitrate standards. Aerosol species (Org, Nitrate, Sulfate, Ammonium, etc) are then determined as the sum of their ion fragments using fragmentation

patterns (DeCarlo 2006; Canagaratna 2007). Organics are classified as ions, composed of carbon, hydrogen, oxygen and may also contain nitrogen and sulfur and subtracting fragments attributable to prevalent gas species (CO2).A single particle soot photometer (SP2, Droplet Measurement Technologies) (Lee et al. 2020, 2022; Slowik et al. 2007; Schwarz et al. 2006) was used to measure the size and mass of black carbon in particles on a single-particle basis. As a BC-containing particle passes through the optical cavity, it absorbs energy from the laser, heats up, and incandesces with the emitted light being proportional to the BC mass. As such, the SP2 provides a direct measurement of the black carbon content in each particle. The incandescence channel was calibrated at the beginning of the TRACER-CAT campaign using differential-mobility-size selected aquadag aerosol. Aquadag is known to produce a higher incandescence signature than ambient rBC of the same carbon mass and the measured ambient rBC mass was corrected following (Baumgardner et al. 2012).

Two methods were used to estimate dust mass concentrations. In one method, we assume that all particles having mobility diameters >650 nm correspond to dust, with the cut diameter corresponding to a size at which there is a clear minimum between modes in the surface area-weighted size distribution (*Figure S4-2*). This approach aligns with the general size range of dust particles compared to smaller aerosols like black and brown carbon. Alternatively, the NRPM measured from the AMS and the BC mass measured from the SP2 was subtracted from the $PM_{2.5}$ mass determined from the size distribution measurements, with the remaining aerosol components being attributed to dust. The dust concentrations derived from the two methods agree well (Figure S2), with a slope of 1.0351 and $r^2 = 0.97$ All following calculations and observations regarding dust use the dust mass derived from the size distribution method.

4.7 Dust Events

Here we discuss types of events and plumes seen throughout the campaign to set the background for further discussion regarding optical properties observed. Throughout the campaign, there were notable BC plumes, primary emissions and nucleation events stemming from traffic emissions, and events during which aerosol mass concentration is largely dominated by dust. *Figure 4-2* shows the size distribution plot for the entirety of the campaign. The image plot shows time series data of particle size distributions weighted by number (bottom panel), surface area (middle panel), and volume (top panel), with black lines representing the total number, surface area, and volume concentrations, respectively. Changes in the size distributions suggest variations in particle sources, atmospheric processing, or environmental factors. Larger particles play a bigger role in volume and surface area, while smaller particles dominate the number concentrations. The figure highlights spikes in particle concentrations from July 9-14, and two prolonged events on July 17-19 and July 21-23 with increased surface area and volume

specifically from large particles, attributed to dust.

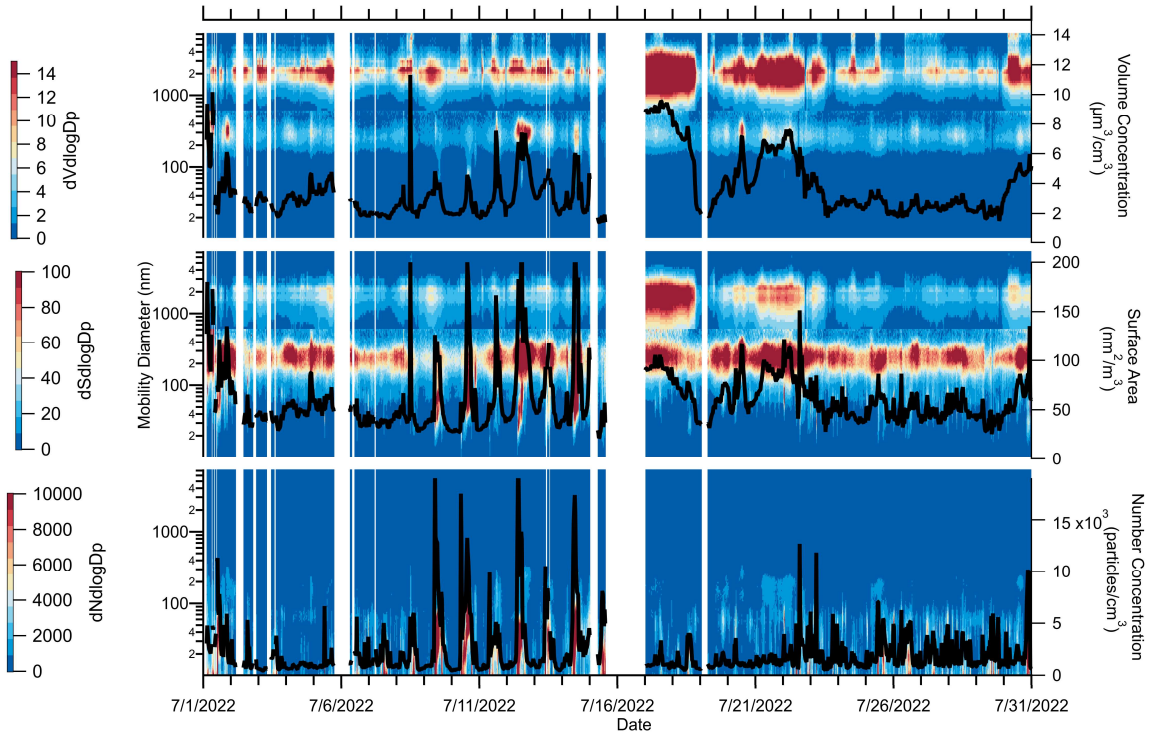

Figure 4-2. Time series of (bottom) number-weighted, (middle) surface-area weighted, and (top) volume-weighted particle size distributions, along with the number, surface area, and volume concentrations (black lines). Gaps in the data reflect times when one or both of the SEMS and APS were down or not collecting data

Figure 4-3 distinguishes the different events by including extinction, absorption, and NRPM mass. The brown shaded area encompasses the two main dust events. Broad and large increase in mass concentration and extinction and absorption coefficients correspond with the increased observed extinction and absorption in *Figure 4-3*, cross referenced with the broad surface area and volume peaks in *Figure 4-2*.

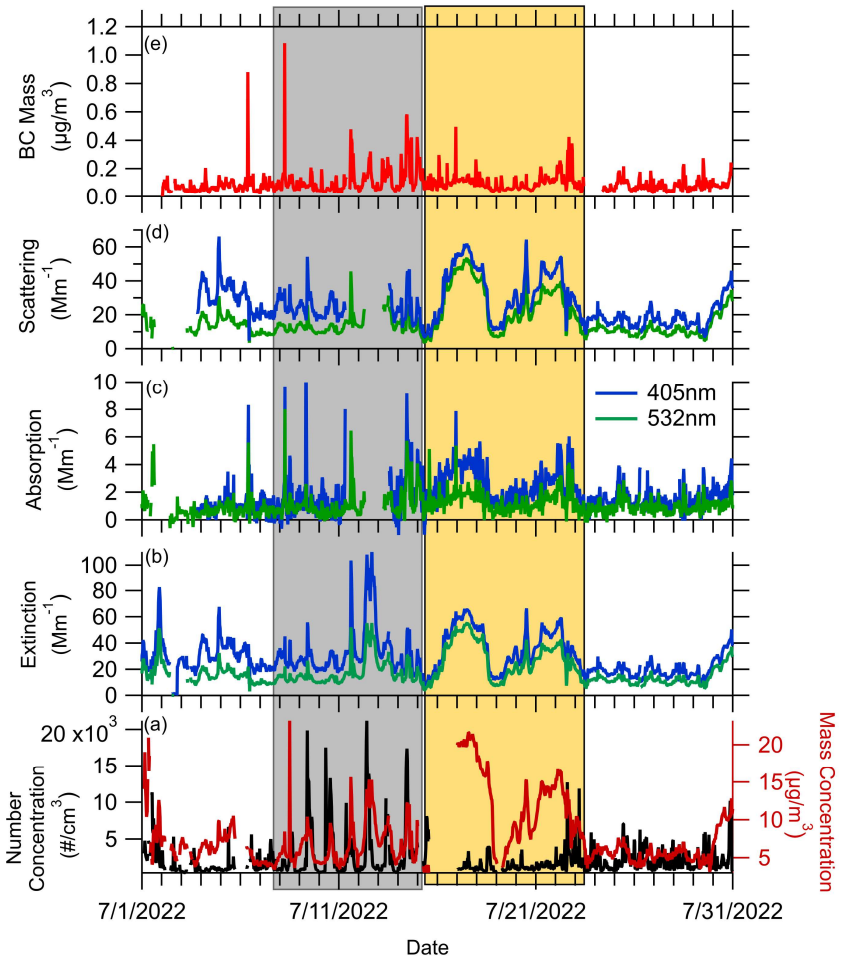

Figure 4-3: Panel (a) shows the number concentration and mass concentration time series, panel (b) the extinction time series as measured by the CRD-PAS, panel (c) shows the absorption time series as measured by the CRD-PAS, panel (d) shows the scattering time series as calculated, and Panel (e) shows the calculated BC mass as measured by the SP2. Where applicable, the green lines denote properties measured at 532nm, and the blue lines denote properties measured at 405nm.

Back trajectory models for the two periods of high PM concentration during July 16-18 and July 20-23 show that the dust was likely transport of Saharan dust. A large broad peak in PM2.5 and light extinction was observed from 16-18 July and a second peak from 19-23 July. The first

period is dust transported from the Sahara Desert region in Africa, which was shown in a back trajectory by NOAA Hysplit transport model (*Figure 4-4*). Additional trajectories are shown to start over the Atlantic Ocean, northwest of the Saharan. These may represent air parcels that incorporate marine aerosols, or potential dust particles from the Saharan that were carried west by prevailing trade winds that then could have mixed with marine air masses The colors represent individual particle trajectories.

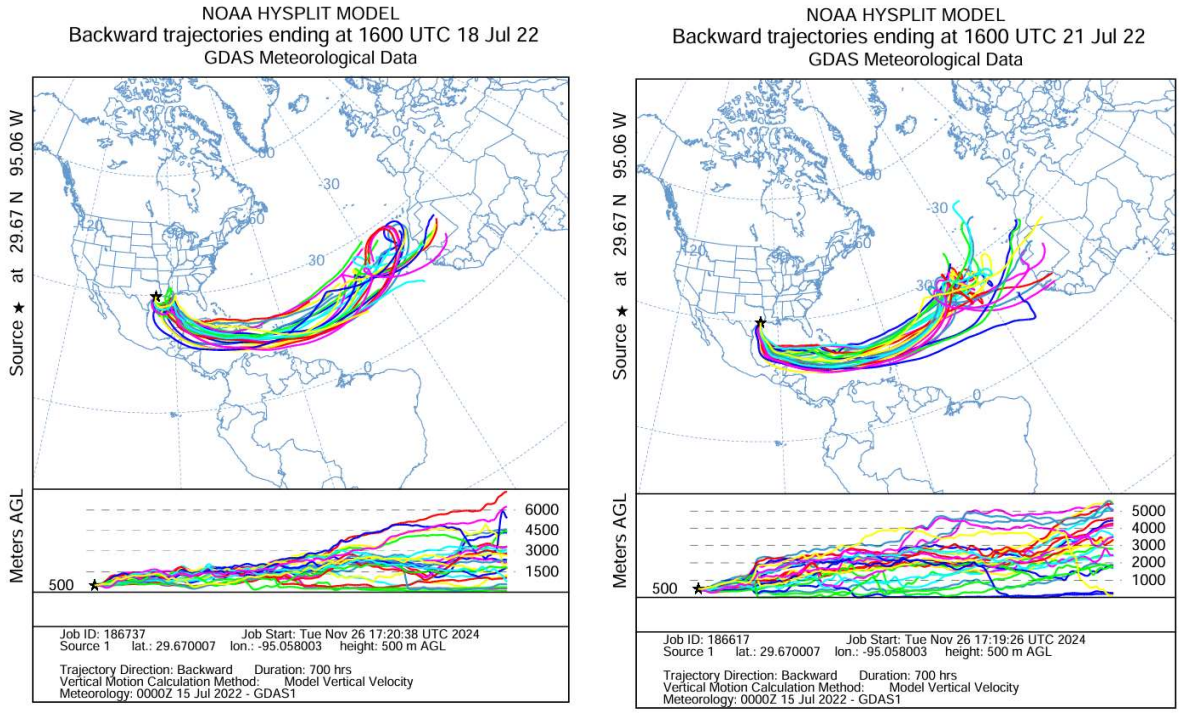

Figure 4-4: NOAA Hysplit model for each dust event. First panel for the dust event during July 16-18 and the second panel for the dust event during July 20-23. The trajectory duration was 700 hours from a height of 500m AGL.

Black carbon was detected in elevated concentrations twice in early July, specifically on July 6 and July 8. The source of the rBC plume on July 8 was likely a small biomass fire visible from the TRACER-CAT site, but the origin of the plume on July 6 remains unidentified. Aside from

these two elevated concentration events, smaller BC events are consistent throughout much of the campaign. For the major rBC plumes, the single-scatter albedo (SSA) at 405 nm was 0.7, and at 532nm was 0.75 compared to a typical campaign-average SSA of 0.97. Generally, throughout the campaign, there was a strong inverse correlation between SSA and the rBC mass fraction.

Linear regression analysis was used to assess the relationships between BC, dust, and the NRPM components. There is a modest relationship between OA and NO_3 and a very weak relationship between NH_4 and NO_3, which could indicate the presence of nitrated organics as a source of brown carbon (Yuan et al. 2020, 2021; Mohr et al. 2009). BC has the strongest correlation with OA and NO_3, suggesting they may derive from a common source. Dust has very weak correlations with BC and all NRPM components, consistent with long-range transport of the dust from the Sahara.

Table 4-1: R^2 correlations between BC, dust and other NRPM components

	BC	*Cl*	*Dust*	*NH_4*	*NO_3*	*OA*	*SO_4*
BC	1						
Cl	0.15	1					
Dust	0.14	0.24	1				
NH_4	0.21	0.08	0.06	1			
NO_3	0.53	0.24	0.26	0.32	1		
OA	0.58	0.13	0.02	0.49	0.68	1	
SO_4	0.17	0.06	0.08	0.99	0.31	0.48	1

Cell colors correspond to R^2 values of <0.25 (light red), 0.25-0.50 (light green), 0.51-0.75 (medium green), and >0.75 (dark green)

4.8 Component Contributions to Light Absorption

The observed light absorption reflects the combination of contributions from BC, BrC, and dust. Moreover, the properties of BrC and dust can vary depending on their sources. We assess the contributions and properties of each absorbing component using a two independent approaches.

4.8.1 Mass Absorption Coefficients

A commonly determined absorption property is the mass absorption coefficient referenced to BC (MAC_{BC}), defined as:

$$\mathrm{MAC_{BC}} = \frac{\mathrm{b_{abs}}}{[\mathrm{BC}]} \qquad \textbf{(1.)}$$

Absent contributions from other aerosol components (e.g., BrC or dust) or the influence of coatings, the MAC_{BC} is a nominally fundamental property of BC that depends on the wavelength of light. (Forestieri et al. 2018) report MAC_{BC} values for pure BC of 9.1 ± 1.1 m^2/g at 532 nm and 12.1 ± 1.4 m^2/g at 405 nm. Liu et al. (2020), in an assessment of recent literature, conclude that the MAC_{BC} at 532 nm is 8.0 ± 0.7 m^2/g. The observation of MAC_{BC} values larger than these indicates contributions from other aerosol components or coatings. We find that the observed MAC_{BC} values at both 405 nm and 532 nm vary with the [BC]/[dust] ratio (*Figure 4-5*).

As the [BC]/[dust] ratio increases the MAC_{BC} asymptotes to around the value expected for pure BC. A fit to the empirical function

$$\mathrm{MAC_{BC}} = \mathrm{p_1} + \mathrm{p_2} \cdot \exp\left(-\frac{\frac{[\mathrm{BC}]}{[\mathrm{dust}]}}{\mathrm{p_3}}\right) \qquad \textbf{(2.)}$$

yields MAC_{BC} = 12.5 m^2/g at 405 nm and 10.3 m^2/g at 532 nm at the high [BC]/[dust] limit, which are reasonably consistent with the values expected for pure BC. This suggests, but does not rule out, contributions from BrC and coatings to the observed absorption. At the low

[BC]/[dust], when dust is the major mass fraction of absorbing aerosol, we observed high values of MAC_{BC} is 33.7 m^2/g at 405 nm and 18.1 m^2/g at 532 nm. The increase over the pure MAC_{BC} value is proportionally greater at 405 nm than 532 nm, reflecting stronger absorption by dust as wavelength decreases. At 405nm, lower AAE values (colorscale in *Figure 4-5***)** correspond with lower MAC values, but throughout the [BC]/[Dust] ratio. Conversely, at 532nm, the lower AAE values correspond with both higher [BC]/[Dust] and MAC values.

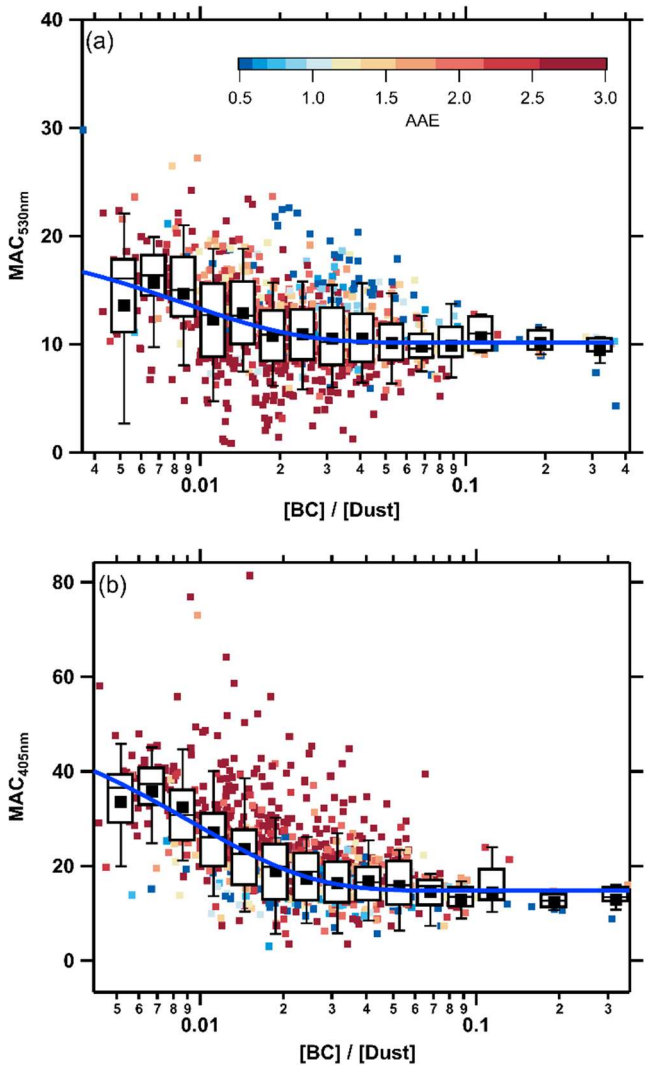

Figure 4-5: Relationship between MAC values at 532 nm (top panel) and 405 nm (bottom panel) with the ratio of BC to dust mass concentration. The points are colored according to AAE.

To further differentiate between the contributions from the different absorbing components we have performed a multi-linear regression. This assumes additivity of the absorption by the different components. Specifically, we have tested the following regression equation:

$$b_{abs} = MAC_{BC} \cdot [BC] + MAC_{dust} \cdot [dust] + MAC_{BrC} \cdot [OA] \qquad \textbf{(3.)}$$

where the fit coefficients are the component-specific *MAC* values. The adjusted R^2 values from the fits were 0.90 (405 nm) and 0.95 (532 nm).

Strong and significant associations with BC and dust are found at both 405 nm and 532 nm. The retrieved MAC_{BC} values of 11.1 ± 0.5 $m^{2\cdot}$ g^{1} (405 nm) and 8.5 ± 0.2 $m^{2\cdot}g^{1}$ (532 nm) are very similar to the values expected for pure BC and correspond to an *AAE* = 0.98. The reported uncertainties correspond to the fit standard error. The retrieved MAC_{dust} values were 0.128 ± 0.005 m^2/g (405 nm) and 0.036 ± 0.002 m^2/g (532 nm), which correspond to an *AAE* value of 4.65. The derived MAC_{dust} at 532 nm is consistent with that determined by (Lack et al. 2009) in the same region for dust transported from the Sahara. Measurements by (Rocha-Lima et al. 2018) show that the MAC_{dust} increases rapidly as wavelength decreases below 600 nm; we derive an AAE value of ~3.9 from their data, which is reasonably consistent with the large value determined here.

At 532 nm there is a strong association (*p* value < 10^{-5}), with the retrieved MAC_{BrC} = 0.20 ± 0.04 m^2/g. The value derived here falls on the somewhat more absorbing side (Cappa et al. 2019; Moschos et al. 2018). However, at 405 nm there is a relatively weak association between absorption and OA, with the multi-linear regression returning *p* = 0.042 with an MAC_{BrC} = 0.2 ± 0.1 m^2/g. It would be surprising if the BrC absorption at 532 nm and 405 nm were equal. The much lower *p* value for 532 nm indicates that the MAC_{BrC} value is more reliable than the value at 405 nm. Outside of the strongly dust-influenced events the b_{abs} values were relatively small. It could be that the generally lower noise on the PAS measurements at 532 nm compared to 405 nm allowed for retrieval of more robust results, which is perhaps consistent with both the *p* value and standard error being smaller for 532 nm than 405 nm.

Similar to the MAC, the mass extinction efficiency (MEE) can be determined via multilinear regression:

$$b_{\mathbf{ext}} = M\boldsymbol{EE}_{BC} \cdot [BC] + M\boldsymbol{EE}_{dust} \cdot [dust] + M\boldsymbol{EE}_{BrC} \cdot [OA] \qquad \textbf{\textit{(4.)}}$$

where the fit coefficients are the component-specific *MAC* values. The MEE for dust w The retrieved MEE_{dust} values were 2.45 ± 0.105 m^2/g (405 nm) and 2.46 ± 0.059 m^2/g (532 nm). The derived MEE_{dust} at 532 nm is consistent with that determined by (Kim et al. 2014, 2019)

Table 4-2: Derived MAC and MEE for BC, Dust, and OA at 532nm and 405nm and their corresponding p values as determined by MLR.

	MAC (m^2/g)	*p* value	MAC (m^2/g)	*p* value	MEE (m^2/g)	*p* value	MEE (m^2/g)	*p* value
	532 nm		405 nm		532 nm		405 nm	
BC	8.5 ± 0.2	$<10^{-5}$	11.1 ± 0.5	$<10^{-5}$	12.4 ± 3.7	0.001	15.04 ± 6.7	0.024
Dust	0.036 ± 0.002	$<10^{-5}$	0.128 ± 0.005	$<10^{-5}$	2.46 ± 0.06	$<10^{-5}$	2.45 ± 0.11	$<10^{-5}$
[OA]	0.20 ± 0.04	$<10^{-5}$	0.2 ± 0.1	0.042	10.21 ± 0.78	$<10^{-5}$	19.83 ± 1.37	$<10^{-5}$

4.9 Relative Component Contributions to Absorption and their Correlations

Using the above MAC values, the relative absorption contributions were determined for each component at 405 nm and 532 nm as both a time series and average over the entire study period (*Figure 4-6*). At both wavelengths, BC contributes to the majority of absorption, with an average fractional contribution of 0.61 (405 nm) and 0.75 (532 nm). For dust, the fractional contribution

is much greater at 405 nm (0.34) than 532 nm (0.16) owing to the relatively large wavelength dependence of the dust MAC. The BrC contribution was modest, <10% on average at both wavelengths.

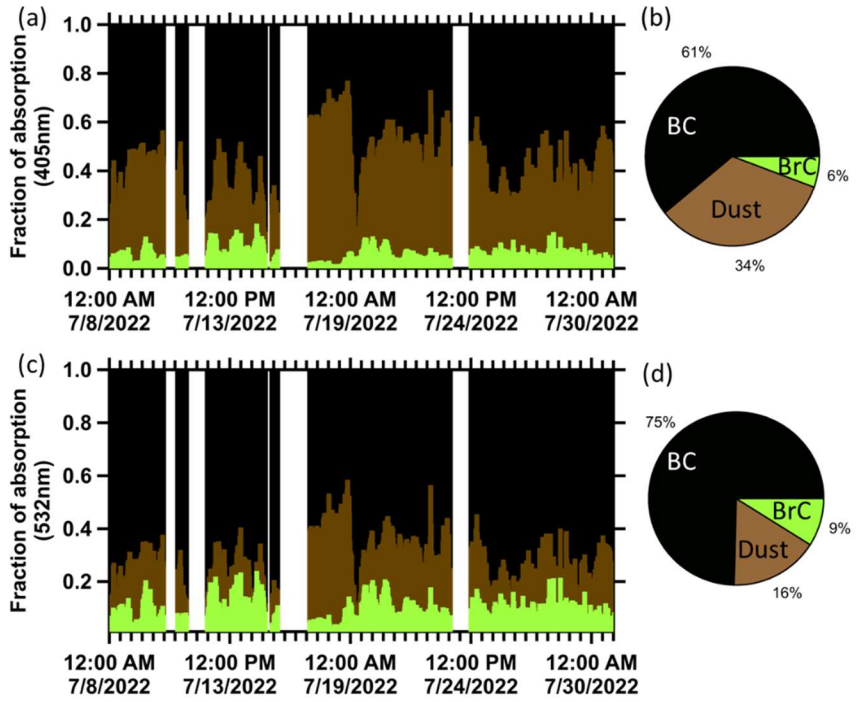

Figure 4-6: *The temporal variability in the relative contributions of BC, BrC, and dust to absorption for (a) 532 nm and (b) 405 nm. Campaign average values are shown in (b) and (d).*

Additional understanding of the contributions of the different aerosol components can be derived from consideration of the relationship between the AAE and SAE (Cappa et al. 2016)(Cazorla et al. 2013). In general, the SAE depends primarily on particle size while the AAE depends on particle composition. As such, a particular combination of the AAE and SAE can help identify the dominant absorbing particle types at a given time. Larger particles, such as dust, have smaller

SAE values while smaller particles, such as BC and OA have larger SAE values. Larger AAE values, specifically AAE > 1, indicate notable contributions to absorption by BrC or dust, while AAE values close to unity indicate absorption by BC dominates (Cappa et al. 2016; Cazorla et al. 2013).

The interpretation of the AAE-SAE relationship can be strengthened by considering the relationship between the AAE and SAE and other metrics. Specifically, the AAE should vary with the BC-to-dust ratio and also with the overall dust fraction of $PM_{2.5}$, while the SAE should vary with the dust fraction of $PM_{2.5}$. These relationships are shown in *Figure 4-7* along with the zones describing the nominal classifications of the AAE-SAE relationship in terms of particle types from (Cappa et al. 2016; Cazorla et al. 2013). The uncertainty in the AAE can be large when the b_{abs} values are small; to highlight the general relationships, graphs involving the AAE the points have been sized and colored according to the observed $b_{abs,532nm}$ values. We find that the AAE-SAE observations generally span from the region classified as mixed dust/BC/BrC to that classified as BC dominated (*Figure 4-7*a). The AAE decreases from around 3 at small BC-to-dust ratios to around unity at large ratios (*Figure 4-7*b) while increasing from around unity at small dust mass fractions to around 3 at large dust mass fractions *Figure 4-7*d), consistent with the generally stronger wavelength dependence of absorption expected for dust compared to BC.

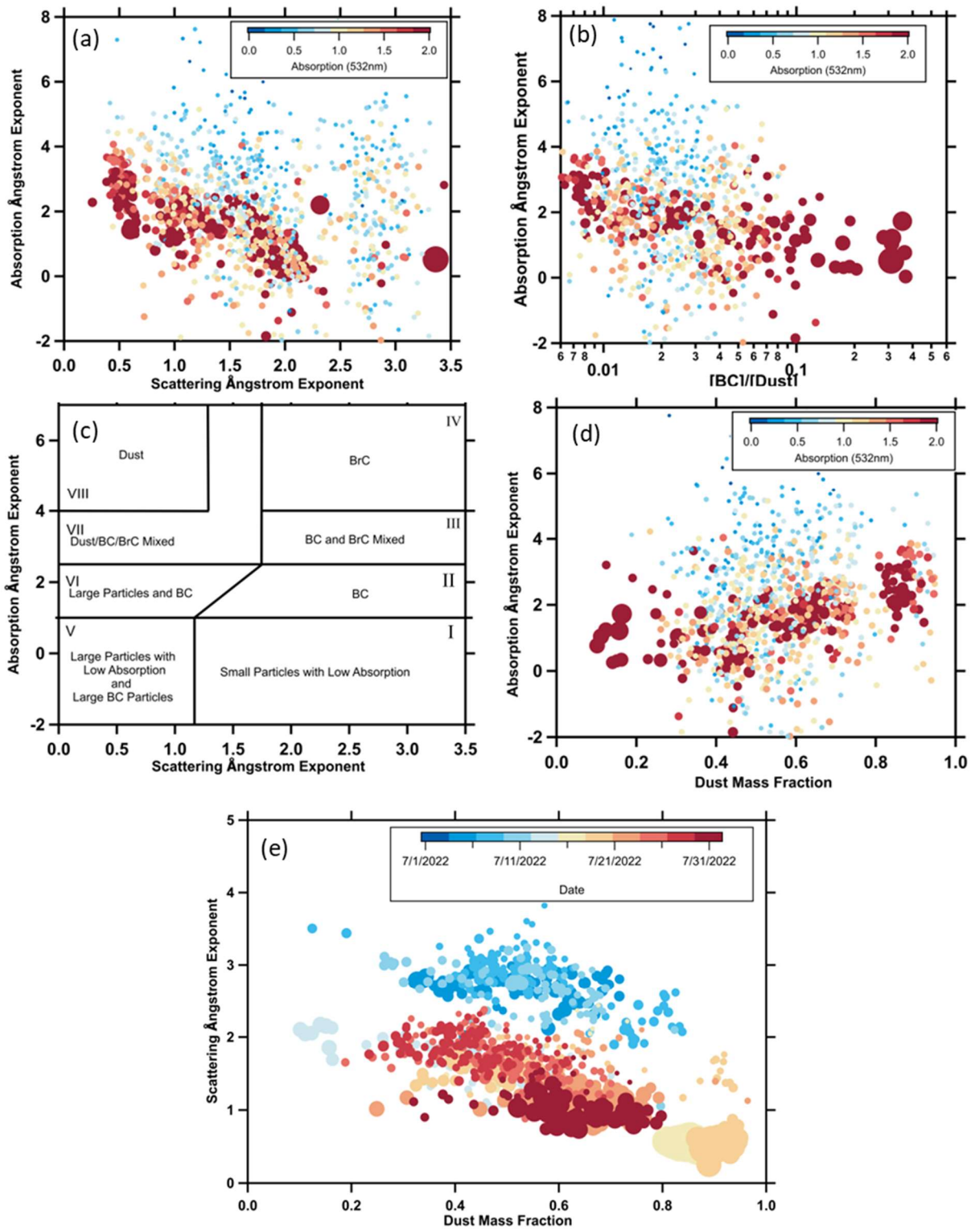

Figure 4-7: Panel (a) shows the relationship between the Absorption Ångström Exponent (AAE) and Scattering Ångström Exponent (SAE), with point size and color representing absorption at

532nm. Panel (b) plots AAE against the [BC]/[Dust] ratio, with point size and color reflecting absorption at 532 nm. Panel (c) provides a classification diagram based on AAE and SAE, categorizing aerosols into eight types: (I) small particles with low absorption, (II) BC, (III) BC and BrC mixed, (IV) BrC, (V) large particles with low absorption and large BC particles, (VI) large particles and BC, (VII) dust/BC/BrC mixed, and (VIII) dust. Panel (d) illustrates AAE versus dust mass fraction, with point size and color indicating absorption. Panel (e) displays SAE versus dust mass fraction, where point color represents the date of the measurement.

We also see that the SAE generally decreases as the dust fraction increases (*Figure 4-7*e), consistent with the larger size of the dust compared to the other $PM_{2.5}$ components. However, a group of points exists off the general SAE-dust fraction trend, with higher SAE values for a given dust fraction. These points correspond to the period before July 13th, at which point there is a clear shift in the SAE from higher to lower values. This shift occurs one day prior to the addition of an extra drier (see methods), suggesting that it does not result from a change in the relative humidity of the measured aerosol. It is possible that the shift in the SAE-dust fraction relationship indicates a change in the dust source, or potentially a misattribution of the large particles as dust rather than another large particle type (e.g., sea spray). NOAA Hysplit Models for July 9-14th support this potential theory, as they show predominant trajectories in the Atlantic from the 9-12th, with the 13th and 14th showing additional trajectories both from the Northern Pacific and from the Saharan Desert (*Figure S4-4*). Additionally, we note that on July 13th, minor adjustments were made due to a potential leak in the SEMS. This may also provide an explanation on the observed shift in SAE-dust fraction, due to losses of larger particles.

4.10 Dust Refractive Index

The absorptivity of aerosols can also be described using the complex refractive index ($m = n + ik$), with both the real (n) and imaginary (k) part of the refractive index influencing absorption. The refractive index of atmospheric dust varies depending on the origin, minerology, and age of the dust. A summary of field and lab measurements of dust absorption indicates k varies from 0.0001 to 0.008 at 520 nm and 0.0001 to 0.0088 at 370 nm (Di Biagio et al. 2019).

We have derived k values for the dust sampled here at both 405 nm and 532 nm by performing an optical closure. Optical closure requires that the absorption due to dust, separate from the other components, is known. We assume that the dust absorption ($b_{abs,dust}$) can be calculated according to:

$$b_{abs,dust} = b_{abs,obs} - \left(b_{abs,BC} + b_{abs,BrC}\right)$$
$$= b_{abs,obs} - \left(MAC_{BC,MLR} \cdot [BC] + MAC_{BrC,MLR} \cdot [OA]\right)$$

where the *MAC* values for BC and BrC are from the multilinear regression. The observed absorption due to dust is compared to that calculated using the measured size distribution for the dust mode (i.e., particles with 650 nm ≤ $D_{p,m}$ ≤ 1.8 μm; see Section 4.6). The value of k_{dust} is determined as that which minimizes the difference between the observed and calculated dust absorption (i.e., minimizes $(b_{abs,dust,obs} - b_{abs,dust,calc})^2$) at each point in time for an assumed value of the real refractive index. We have assumed n_{dust} = 1.6 (Di Biagio et al. 2019). The retrieved k_{dust} values at both wavelengths are log-normally distributed, and a log-normal fit to the distributions yields k_{dust}(405 nm) = 0.0039 and k_{dust}(532 nm) = 0.0016 (*Figure S**4-5***). Both retrieved k_{dust} values fall within the range of literature values at similar wavelengths. Similar

results are obtained if the closure is performed using the campaign average absorption and size distributions.

4.11 Hygroscopicity Analyses

Water uptake influences aerosol light extinction and depends on particle composition. The influence of water uptake on light extinction is often characterized by the dimensionless parameter γ_{RH}, defined as:

$$\gamma_{RH} = [\frac{\log(f_{RH})}{\log(\frac{100 - RH_{dry}}{100 - RH_{wet}})}]$$

where f_{RH} is defined as the ratio between the extinction measured for humidified (RH_{wet}) and dry (RH_{dry}) conditions. The γ_{RH} parameter assumes that water uptake varies continuously with relative humidity and provides a nominally RH-independent metric that can be used to assess changes in particle hygroscopicity over time. γ_{RH} depends on both particle size and composition, with the latter often dominating the behavior. Various studies (e.g., (Massoli et al. 2009; Quinn et al. 2005)) have found a nominally linear relationship between γ_{RH} and the OA mass fraction for sub-micron aerosol. (Zhang et al. 2014) extended such analyses to consider also the impacts of dust on water uptake for supermicron particles.

Figure 4-8 shows γ_{RH} as a function of the ratio of less hygroscopic aerosol components (i.e., dust, OA, and BC) to the total PM2.5, which includes the more hygroscopic inorganic salts. The observations have been split into two periods to account for the addition of an extra drier on 14 July (see methods), with the average dry RH = 48.3% ± 1.4% before the addition of the drier and RH = 28.5% ± 2.5% after. The average RH for the humidified airstream was unaffected by the addition of the drier, with the high RH = 88.7% ± 1.5% before and RH = 87.2% ± 1.7% after.

We find that the extent of drying that occurred with the ambient sample had a notable influence on the observed hygroscopicity. Comparably lower overall γ_{RH} values were observed for a given less hygroscopic $PM_{2.5}$ fraction when the drying was less efficient (i.e., with higher dry RH), which suggests that there was residual water present. Residual water would lead to larger dry b_{ext} values and thus lower γ_{RH}. Below, we refer to the observations before and after the addition of the extra drier as "less dry" and "more dry," respectively.

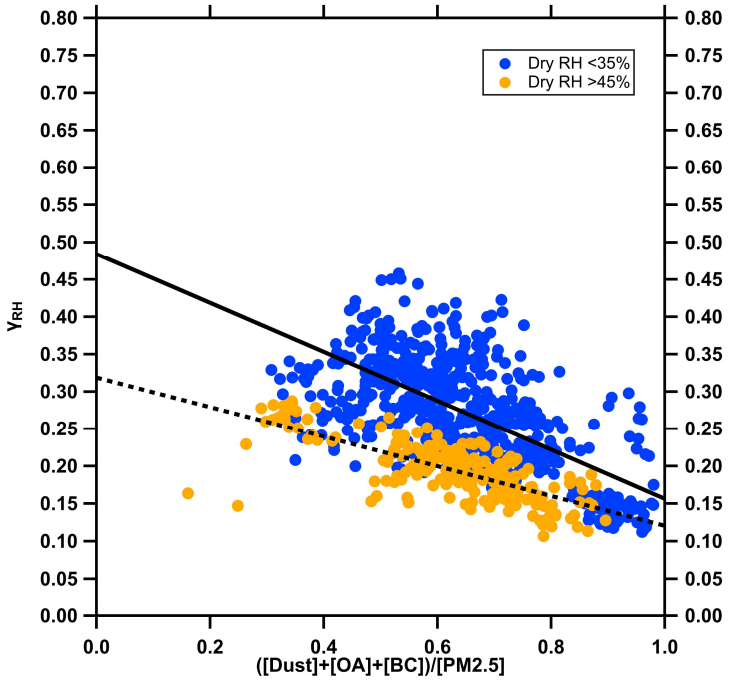

Figure 4-8: γ_{RH} vs the ratio of the combined mass concentration of dust, OA and BC to mass concentration of PM2.5. Points are colored by the RH achieved after the dryers and before any humidification.

Considering the less dry and more dry observations independently, we find there is a reasonable inverse relationship between the observed γ_{RH} and the mass fraction of the less hygroscopic

components in both cases (*Figure 4-8*). The spread in the γ_{RH} is somewhat greater for the more dry observations. We find no dependence of γ_{RH} for the more dry observations on RH variations over the "dry" range 25-35% suggesting that the variability is not due to additional smaller scale changes in the dry RH.

Focusing on the more dry observations, we find that a linear fit to γ_{RH} vs dust+BC+OA mass fraction yields a slope of -0.3 and a y-intercept of $\gamma_{RH} = 0.48$, with $R^2 = 0.44$. This indicates that the γ_{RH} =0.48 for the more hygroscopic inorganic salts while $\gamma_{RH} = 0.15$ for the less hygroscopic components. These values are reasonably consistent with the observations from Quinn et al. 2005 and Massoli et al. 2009, which were 0.9 and 0.39-0.66, respectively, despite the differences in the definition of the fraction used (e.g., OA fraction or (OA+BC+dust) fraction). As has been noted by Titos et al. (2016), in deducing relationships between γ_{RH} and composition it is important to comprehensively consider the major aerosol components. Indeed, consideration of the OA fraction or the OA+BC fraction, excluding dust, does not provide for a robust relationship with γ_{RH} ($R^2 = 0.04$ for both). For the less dry observations, the slope = -0.20 and the intercept = 0.32, with $R^2 = 0.54$. This intercept is lower than expected and illustrates the importance of ensuring sufficient drying.

We have also considered whether variability in the relative contribution of dust versus OA and BC together contributes to the variability in the observed γ_{RH} for the more dry conditions and find no clear relationship. It may be that differences in the hygroscopicity of the dust (c.f.,(Zhang et al. 2014)) or the OA (c.f., Jimenez et al. 2009) between events or with time, perhaps dependent on the extent of atmospheric processing, are driving the variability. We should also recognize that we lack a direct measurement of dust, instead assuming that all particles >650 nm are dust. It could be that some fraction of the "dust" actually corresponds to sea spray particles,

which are highly hygroscopic, and that variations in this fraction could contribute to variability in the γ_{RH}. However, we note that the dust-to-(OA+BC) mass ratio averages 10.4, indicating that dust dominates over OA and BC most of the time. If sea spray contributed substantially to the "dust" mass then the observed γ_{RH} values should be substantially larger, but nonetheless contributions from sea spray cannot be ruled out.

4.12 Conclusions

This study provides an analysis of $PM_{2.5}$ optical properties measured using in situ methods, with a particular focus on absorption, during the TRACER-CAT campaign in Houston, TX in July 2022. We find that black carbon, brown carbon, and dust all contribute to the observed absorption for urban pollution and long-range Saharan dust episodes. On average, BC contributed most to the absorption (61% at 405 nm and 75% at 532 nm), followed by dust (34% and 16%, respectively), and then brown carbon (6% and 9%, respectively). It was not possible to separately deduce the influence of coatings on the BC absorption, although this effect appears to be small. Component-specific mass absorption coefficient values were determined using multi-linear regression, with the derived $MAC_{532nm} = 8.5 \pm 0.2$ m² g⁻¹ and MAC_{405nm} 11.1 ± 0.5 m² g⁻¹ for black carbon, $MAC_{532nm} = 0.036 \pm 0.002$ m² g⁻¹ and $MAC_{405nm} = 0.128 \pm 0.005$ m² g⁻¹ for dust, and $MAC_{532nm} = 0.20 \pm 0.04$ m² g⁻¹ and $MAC_{405nm} = 0.2 \pm 0.1$ m² g^{-1} for brown carbon (and where it is assumed that all organic aerosol is brown carbon). BC and OA exhibited a modest correlation, potentially indicating that they derive from a common source. BC and OA also exhibited modest correlations with nitrate, but not with other inorganic salts (i.e., sulfate, ammonium, and chloride), suggesting that nitrated organic species may contribute to brown carbon absorption. Back trajectory analysis indicated that the dust was likely transported from the Sahara Desert in Africa. Dust had a weak correlation with nitrate, which suggests that the

dust has undergone some chemical processing during transport. A closure analysis was performed to determine the dust refractive index values, with the retrieved values of $k = 0.00396$ at 405 nm and $k = 0.0016$ at 532 nm. Consideration of the aerosol hygroscopicity show that sufficiently drying aerosols prior to measurement improves γ_{RH} estimation. Additionally, the variability seen in γ_{RH} likely stems from differences in dust and OA hygroscopicity, potential sea spray contributions, and atmospheric processing. Overall, this work emphasizes the importance of understanding the interaction between aerosol components, atmospheric processes, and hygroscopicity.

Our findings are specific to the mixed urban and dust episodes observed during summer in the coastal subtropics. Different environmental regimes present distinct characteristics. Understanding these variations across diverse environments is essential for improving estimates of radiative forcing and impacts in global climate models.

4.13 References

Allen, R.W., Carlsten, C., Karlen, B., Leckie, S., van Eeden, S., Vedal, S., Wong, I., and Brauer, M. (2011). An air filter intervention study of endothelial function among healthy adults in a woodsmoke-impacted community. *Am J Respir Crit Care Med* 183 (9):1222–1230. doi:10.1164/rccm.201010-1572OC.

Al-Naiema, I.M., Hettiyadura, A.P.S., Wallace, H.W., Sanchez, N.P., Madler, C.J., Cevik, B.K., Bui, A.A.T., Kettler, J., Griffin, R.J., and Stone, E.A. (2018). Source apportionment of fine particulate matter in Houston, Texas: insights to secondary organic aerosols. *Atmospheric Chemistry and Physics* 18 (21):15601–15622. doi:10.5194/acp-18-15601-2018.

Andreae, M.O. and Gelencsér, A. (2006). Black carbon or brown carbon? The nature of light-absorbing carbonaceous aerosols. *Atmospheric Chemistry and Physics* 6 (10):3131–3148. doi:10.5194/acp-6-3131-2006.

Andreae, M.O. and Rosenfeld, D. (2008). Aerosol–cloud–precipitation interactions. Part 1. The nature and sources of cloud-active aerosols. *Earth-Science Reviews* 89 (1):13–41. doi:10.1016/j.earscirev.2008.03.001.

AR6 Climate Change 2022: Mitigation of Climate Change — IPCC. (n.d.). Available at https://www.ipcc.ch/report/sixth-assessment-report-working-group-3/ (Accessed 28 April 2022).

Banta, R.M. (2008). Stable-boundary-layer regimes from the perspective of the low-level jet. *Acta Geophys.* 56 (1):58–87. doi:10.2478/s11600-007-0049-8.

Baumgardner, D., Popovicheva, O., Allan, J., Bernardoni, V., Cao, J., Cavalli, F., Cozic, J., Diapouli, E., Eleftheriadis, K., Genberg, P.J., Gonzalez, C., Gysel, M., John, A., Kirchstetter, T.W., Kuhlbusch, T. a. J., Laborde, M., Lack, D., Müller, T., Niessner, R., Petzold, A., Piazzalunga, A., Putaud, J.P., Schwarz, J., Sheridan, P., Subramanian, R., Swietlicki, E., Valli, G., Vecchi, R., and Viana, M. (2012). Soot reference materials for instrument calibration and intercomparisons: a workshop summary with recommendations. *Atmospheric Measurement Techniques* 5 (8):1869–1887. doi:10.5194/amt-5-1869-2012.

Baynard, T., Garland, R.M., Ravishankara, A.R., Tolbert, M.A., and Lovejoy, E.R. (2006). Key factors influencing the relative humidity dependence of aerosol light scattering. *Geophysical Research Letters* 33 (6). doi:10.1029/2005GL024898.

Bond, T.C. and Bergstrom, R.W. (2006). Light Absorption by Carbonaceous Particles: An Investigative Review. *Aerosol Science and Technology* 40 (1):27–67. doi:10.1080/02786820500421521.

Bond, T.C., Doherty, S.J., Fahey, D.W., Forster, P.M., Berntsen, T., DeAngelo, B.J., Flanner, M.G., Ghan, S., Kärcher, B., Koch, D., Kinne, S., Kondo, Y., Quinn, P.K., Sarofim, M.C., Schultz, M.G., Schulz, M., Venkataraman, C., Zhang, H., Zhang, S., Bellouin, N., Guttikunda, S.K., Hopke, P.K., Jacobson, M.Z., Kaiser, J.W., Klimont, Z., Lohmann, U., Schwarz, J.P., Shindell, D., Storelvmo, T., Warren, S.G., and Zender, C.S. (2013). Bounding the role of black carbon in the climate system: A scientific assessment. *Journal of Geophysical Research: Atmospheres* 118 (11):5380–5552. doi:10.1002/jgrd.50171.

Bond, T.C., Habib, G., and Bergstrom, R.W. (2006). Limitations in the enhancement of visible light absorption due to mixing state. *Journal of Geophysical Research: Atmospheres* 111 (D20). doi:10.1029/2006JD007315.

Brem, B.T., Mena Gonzalez, F.C., Meyers, S.R., Bond, T.C., and Rood, M.J. (2012). Laboratory-Measured Optical Properties of Inorganic and Organic Aerosols at Relative Humidities up to 95%. *Aerosol Science and Technology* 46 (2):178–190. doi:10.1080/02786826.2011.617794.

Cappa, C.D., Kolesar, K.R., Zhang, X., Atkinson, D.B., Pekour, M.S., Zaveri, R.A., Zelenyuk, A., and Zhang, Q. (2016). Understanding the optical properties of ambient sub- and supermicron particulate matter: results from the CARES 2010 field study in northern California. *Atmospheric Chemistry and Physics* 16 (10):6511–6535. doi:10.5194/acp-16-6511-2016.

Cappa, C.D., Lack, D.A., Burkholder, J.B., and Ravishankara, A.R. (2008). Bias in Filter-Based Aerosol Light Absorption Measurements Due to Organic Aerosol Loading: Evidence from Laboratory Measurements. *Aerosol Science and Technology* 42 (12):1022–1032. doi:10.1080/02786820802389285.

Cappa, C.D., Onasch, T.B., Massoli, P., Worsnop, D.R., Bates, T.S., Cross, E.S., Davidovits, P., Hakala, J., Hayden, K.L., Jobson, B.T., Kolesar, K.R., Lack, D.A., Lerner, B.M., Li, S.-M., Mellon, D., Nuaaman, I., Olfert, J.S., Petäjä, T., Quinn, P.K., Song, C., Subramanian, R., Williams, E.J., and Zaveri, R.A. (2012). Radiative Absorption Enhancements Due to the Mixing State of Atmospheric Black Carbon. *Science* 337 (6098):1078–1081. doi:10.1126/science.1223447.

Cappa, C.D., Zhang, X., Russell, L.M., Collier, S., Lee, A.K.Y., Chen, C.-L., Betha, R., Chen, S., Liu, J., Price, D.J., Sanchez, K.J., McMeeking, G.R., Williams, L.R., Onasch, T.B., Worsnop, D.R., Abbatt, J., and Zhang, Q. (2019). Light Absorption by Ambient Black and Brown Carbon and its Dependence on Black Carbon Coating State for Two California, USA, Cities in Winter and Summer. *Journal of Geophysical Research: Atmospheres* 124 (3):1550–1577. doi:10.1029/2018JD029501.

Carrico, C.M., Capek, T.J., Gorkowski, K.J., Lam, J.T., Gulick, S., Karacaoglu, J., Lee, J.E., Dungan, C., Aiken, A.C., Onasch, T.B., Freedman, A., Mazzoleni, C., and Dubey, M.K. (2021). Humidified single-scattering albedometer (H-CAPS-PMSSA): Design, data analysis, and validation. *Aerosol Science and Technology* 0 (0):1–20. doi:10.1080/02786826.2021.1895430.

Cazorla, A., Bahadur, R., Suski, K.J., Cahill, J.F., Chand, D., Schmid, B., Ramanathan, V., and Prather, K.A. (2013). Relating aerosol absorption due to soot, organic carbon, and dust to emission sources determined from in-situ chemical measurements. *Atmospheric Chemistry and Physics* 13 (18):9337–9350. doi:10.5194/acp-13-9337-2013.

Corbin, J.C., Czech, H., Massabò, D., de Mongeot, F.B., Jakobi, G., Liu, F., Lobo, P., Mennucci, C., Mensah, A.A., Orasche, J., Pieber, S.M., Prévôt, A.S.H., Stengel, B., Tay, L.-L., Zanatta, M., Zimmermann, R., El Haddad, I., and Gysel, M. (2019). Infrared-absorbing carbonaceous tar can dominate light absorption by marine-engine exhaust. *npj Clim Atmos Sci* 2 (1):1–10. doi:10.1038/s41612-019-0069-5.

Cox, J., Isiugo, K., Ryan, P., Grinshpun, S.A., Yermakov, M., Desmond, C., Jandarov, R., Vesper, S., Ross, J., Chillrud, S., Dannemiller, K., and Reponen, T. (2018). Effectiveness of a portable air cleaner in removing aerosol particles in homes close to highways. *Indoor Air* 28 (6):818–827. doi:10.1111/ina.12502.

Cui, X., Wang, X., Yang, L., Chen, B., Chen, J., Andersson, A., and Gustafsson, Ö. (2016). Radiative absorption enhancement from coatings on black carbon aerosols. *Science of The Total Environment* 551–552:51–56. doi:10.1016/j.scitotenv.2016.02.026.

Curtius, J., Granzin, M., and Schrod, J. (2021). Testing mobile air purifiers in a school classroom: Reducing the airborne transmission risk for SARS-CoV-2. *Aerosol Science and Technology* 55 (5):586–599. doi:10.1080/02786826.2021.1877257.

Di Biagio, C., Formenti, P., Balkanski, Y., Caponi, L., Cazaunau, M., Pangui, E., Journet, E., Nowak, S., Andreae, M.O., Kandler, K., Saeed, T., Piketh, S., Seibert, D., Williams, E., and Doussin, J.-F. (2019). Complex refractive indices and single-scattering albedo of global dust aerosols in the shortwave spectrum and relationship to size and iron content. *Atmospheric Chemistry and Physics* 19 (24):15503–15531. doi:10.5194/acp-19-15503-2019.

Erlick, C., Abbatt, J.P.D., and Rudich, Y. (2011). How Different Calculations of the Refractive Index Affect Estimates of the Radiative Forcing Efficiency of Ammonium Sulfate Aerosols. *Journal of the Atmospheric Sciences* 68 (9):1845–1852. doi:10.1175/2011JAS3721.1.

Farley, R.N., Lee, J.E., Rivellini, L.-H., Lee, A.K.Y., Dal Porto, R., Cappa, C.D., Gorkowski, K., Shawon, A.S.M., Benedict, K.B., Aiken, A.C., Dubey, M.K., and Zhang, Q. (2024). Chemical properties and single-particle mixing state of soot aerosol in Houston during the TRACER campaign. *Atmospheric Chemistry and Physics* 24 (7):3953–3971. doi:10.5194/acp-24-3953-2024.

Fierce, L., Bond, T.C., Bauer, S.E., Mena, F., and Riemer, N. (2016). Black carbon absorption at the global scale is affected by particle-scale diversity in composition. *Nat Commun* 7 (1):12361. doi:10.1038/ncomms12361.

Forestieri, S.D., Helgestad, T.M., Lambe, A.T., Renbaum-Wolff, L., Lack, D.A., Massoli, P., Cross, E.S., Dubey, M.K., Mazzoleni, C., Olfert, J.S., Sedlacek III, A.J., Freedman, A., Davidovits, P., Onasch, T.B., and Cappa, C.D. (2018). Measurement and modeling of the multiwavelength optical properties of uncoated flame-generated soot. *Atmospheric Chemistry and Physics* 18 (16):12141–12159. doi:10.5194/acp-18-12141-2018.

Fuller, K.A. (1995). Scattering and absorption cross sections of compounded spheres. II. Calculations for external aggregation. *J. Opt. Soc. Am. A, JOSAA* 12 (5):881–892. doi:10.1364/JOSAA.12.000881.

Fuller, K.A., Malm, W.C., and Kreidenweis, S.M. (1999). Effects of mixing on extinction by carbonaceous particles. *Journal of Geophysical Research: Atmospheres* 104 (D13):15941–15954. doi:10.1029/1998JD100069.

Ghan, S.J., Liu, X., Easter, R.C., Zaveri, R., Rasch, P.J., Yoon, J.-H., and Eaton, B. (2012). Toward a Minimal Representation of Aerosols in Climate Models: Comparative Decomposition of Aerosol Direct, Semidirect, and Indirect Radiative Forcing. *Journal of Climate* 25 (19):6461–6476. doi:10.1175/JCLI-D-11-00650.1.

Intergovernmental Panel On Climate Change (2023). Climate Change 2021 – The Physical Science Basis: Working Group I Contribution to the Sixth Assessment Report of the Intergovernmental Panel on Climate Change, 1st ed. Cambridge University Press.

Jacobson, M.Z. (2012). Investigating cloud absorption effects: Global absorption properties of black carbon, tar balls, and soil dust in clouds and aerosols. *Journal of Geophysical Research: Atmospheres* 117 (D6). doi:10.1029/2011JD017218.

Jacobson, M.Z. (2001). Strong radiative heating due to the mixing state of black carbon in atmospheric aerosols. *Nature* 409 (6821):695–697. doi:10.1038/35055518.

Jimenez, J.L., Canagaratna, M.R., Donahue, N.M., Prevot, A.S.H., Zhang, Q., Kroll, J.H., DeCarlo, P.F., Allan, J.D., Coe, H., Ng, N.L., Aiken, A.C., Docherty, K.S., Ulbrich, I.M.,

Grieshop, A.P., Robinson, A.L., Duplissy, J., Smith, J.D., Wilson, K.R., Lanz, V.A., Hueglin, C., Sun, Y.L., Tian, J., Laaksonen, A., Raatikainen, T., Rautiainen, J., Vaattovaara, P., Ehn, M., Kulmala, M., Tomlinson, J.M., Collins, D.R., Cubison, M.J., E., Dunlea, J., Huffman, J.A., Onasch, T.B., Alfarra, M.R., Williams, P.I., Bower, K., Kondo, Y., Schneider, J., Drewnick, F., Borrmann, S., Weimer, S., Demerjian, K., Salcedo, D., Cottrell, L., Griffin, R., Takami, A., Miyoshi, T., Hatakeyama, S., Shimono, A., Sun, J.Y., Zhang, Y.M., Dzepina, K., Kimmel, J.R., Sueper, D., Jayne, J.T., Herndon, S.C., Trimborn, A.M., Williams, L.R., Wood, E.C., Middlebrook, A.M., Kolb, C.E., Baltensperger, U., and Worsnop, D.R. (2009). Evolution of Organic Aerosols in the Atmosphere. *Science* 326 (5959):1525–1529. doi:10.1126/science.1180353.

Kelly, F.J. and Fussell, J.C. (2019). Improving indoor air quality, health and performance within environments where people live, travel, learn and work. *Atmospheric Environment* 200:90–109. doi:10.1016/j.atmosenv.2018.11.058.

Khalizov, A.F., Xue, H., Wang, L., Zheng, J., and Zhang, R. (2009). Enhanced Light Absorption and Scattering by Carbon Soot Aerosol Internally Mixed with Sulfuric Acid. *J. Phys. Chem. A* 113 (6):1066–1074. doi:10.1021/jp807531n.

Kim, D., Chin, M., Yu, H., Diehl, T., Tan, Q., Kahn, R.A., Tsigaridis, K., Bauer, S.E., Takemura, T., Pozzoli, L., Bellouin, N., Schulz, M., Peyridieu, S., Chédin, A., and Koffi, B. (2014). Sources, sinks, and transatlantic transport of North African dust aerosol: A multimodel analysis and comparison with remote sensing data. *Journal of Geophysical Research: Atmospheres* 119 (10):6259–6277. doi:10.1002/2013JD021099.

Kim, D., Chin, M., Yu, H., Pan, X., Bian, H., Tan, Q., Kahn, R.A., Tsigaridis, K., Bauer, S.E., Takemura, T., Pozzoli, L., Bellouin, N., and Schulz, M. (2019). Asian and Trans-Pacific Dust: A Multimodel and Multiremote Sensing Observation Analysis. *Journal of Geophysical Research: Atmospheres* 124 (23):13534–13559. doi:10.1029/2019JD030822.

Knox, A., Evans, G.J., Brook, J.R., Yao, X., Jeong, C.-H., Godri, K.J., Sabaliauskas, K., and Slowik, J.G. (2009). Mass Absorption Cross-Section of Ambient Black Carbon Aerosol in Relation to Chemical Age. *Aerosol Science and Technology* 43 (6):522–532. doi:10.1080/02786820902777207.

Kok, J.F., Albani, S., Mahowald, N.M., and Ward, D.S. (2014). An improved dust emission model – Part 2: Evaluation in the Community Earth System Model, with implications for the use of dust source functions. *Atmospheric Chemistry and Physics* 14 (23):13043–13061. doi:10.5194/acp-14-13043-2014.

Lack, D.A. and Cappa, C.D. (2010). Impact of brown and clear carbon on light absorption enhancement, single scatter albedo and absorption wavelength dependence of black carbon. *Atmospheric Chemistry and Physics* 10 (9):4207–4220. doi:10.5194/acp-10-4207-2010.

Lack, D.A., Cappa, C.D., Covert, D.S., Baynard, T., Massoli, P., Sierau, B., Bates, T.S., Quinn, P.K., Lovejoy, E.R., and Ravishankara, A.R. (2008). Bias in Filter-Based Aerosol Light Absorption Measurements Due to Organic Aerosol Loading: Evidence from Ambient Measurements. *Aerosol Science and Technology* 42 (12):1033–1041. doi:10.1080/02786820802389277.

Lack, D.A., Langridge, J.M., Bahreini, R., Cappa, C.D., Middlebrook, A.M., and Schwarz, J.P. (2012). Brown carbon and internal mixing in biomass burning particles. *Proceedings of the National Academy of Sciences* 109 (37):14802–14807. doi:10.1073/pnas.1206575109.

Lack, D.A., Quinn, P.K., Massoli, P., Bates, T.S., Coffman, D., Covert, D.S., Sierau, B., Tucker, S., Baynard, T., Lovejoy, E., Murphy, D.M., and Ravishankara, A.R. (2009). Relative humidity dependence of light absorption by mineral dust after long-range atmospheric transport from the Sahara. *Geophysical Research Letters* 36 (24). doi:10.1029/2009GL041002.

Lambe, A.T., Ahern, A.T., Wright, J.P., Croasdale, D.R., Davidovits, P., and Onasch, T.B. (2015). Oxidative aging and cloud condensation nuclei activation of laboratory combustion soot. *Journal of Aerosol Science* 79:31–39. doi:10.1016/j.jaerosci.2014.10.001.

Langridge, J.M., Richardson, M.S., Lack, D., Law, D., and Murphy, D.M. (2011). Aircraft Instrument for Comprehensive Characterization of Aerosol Optical Properties, Part I: Wavelength-Dependent Optical Extinction and Its Relative Humidity Dependence Measured Using Cavity Ringdown Spectroscopy. *Aerosol Science and Technology* 45 (11):1305–1318. doi:10.1080/02786826.2011.592745.

Laskin, A., Laskin, J., and Nizkorodov, S.A. (2015). Chemistry of Atmospheric Brown Carbon. *Chem. Rev.* 115 (10):4335–4382. doi:10.1021/cr5006167.

Lee, J.E., Dubey, M.K., Aiken, A.C., Chylek, P., and Carrico, C.M. (2020). Optical and Chemical Analysis of Absorption Enhancement by Mixed Carbonaceous Aerosols in the 2019 Woodbury, AZ, Fire Plume. *Journal of Geophysical Research: Atmospheres* 125 (15):e2020JD032399. doi:https://doi.org/10.1029/2020JD032399.

Lee, J.E., Gorkowski, K., Meyer, A.G., Benedict, K.B., Aiken, A.C., and Dubey, M.K. (2022). Wildfire Smoke Demonstrates Significant and Predictable Black Carbon Light Absorption Enhancements. *Geophysical Research Letters* 49 (14):e2022GL099334. doi:10.1029/2022GL099334.

Li, J., Carlson, B.E., Yung, Y.L., Lv, D., Hansen, J., Penner, J.E., Liao, H., Ramaswamy, V., Kahn, R.A., Zhang, P., Dubovik, O., Ding, A., Lacis, A.A., Zhang, L., and Dong, Y. (2022). Scattering and absorbing aerosols in the climate system. *Nat Rev Earth Environ* 3 (6):363–379. doi:10.1038/s43017-022-00296-7.

Li, L., Mahowald, N.M., Miller, R.L., Pérez García-Pando, C., Klose, M., Hamilton, D.S., Gonçalves Ageitos, M., Ginoux, P., Balkanski, Y., Green, R.O., Kalashnikova, O., Kok, J.F., Obiso, V., Paynter, D., and Thompson, D.R. (2021). Quantifying the range of the dust direct radiative effect due to source mineralogy uncertainty. *Atmospheric Chemistry and Physics* 21 (5):3973–4005. doi:10.5194/acp-21-3973-2021.

Li, W., Wang, Y., Bernier, C., and Estes, M. (2020). Identification of Sea Breeze Recirculation and Its Effects on Ozone in Houston, TX, During DISCOVER-AQ 2013. *Journal of Geophysical Research: Atmospheres* 125 (22):e2020JD033165. doi:10.1029/2020JD033165.

Liu, D.T., Phillips, K.M., Speth, M.M., Besser, G., Mueller, C.A., and Sedaghat, A.R. (2022). Portable HEPA Purifiers to Eliminate Airborne SARS-CoV-2: A Systematic Review. *Otolaryngology–Head and Neck Surgery* 166 (4):615–622. doi:10.1177/01945998211022636.

Liu, F., Snelling, D.R., Thomson, K.A., and Smallwood, G.J. (2018). Estimate of scattering truncation in the cavity attenuated phase shift PMSSA monitor using radiative transfer theory. *Aerosol Science and Technology* 52 (5):588–596. doi:10.1080/02786826.2018.1437891.

Liu, F., Yon, J., Fuentes, A., Lobo, P., Smallwood, G.J., and Corbin, J.C. (2020a). Review of recent literature on the light absorption properties of black carbon: Refractive index, mass absorption cross section, and absorption function. *Aerosol Science and Technology* 54 (1):33–51. doi:10.1080/02786826.2019.1676878.

Liu, F., Yon, J., Fuentes, A., Lobo, P., Smallwood, G.J., and Corbin, J.C. (2020b). Review of recent literature on the light absorption properties of black carbon: Refractive index, mass absorption cross section, and absorption function. *Aerosol Science and Technology* 54 (1):33–51. doi:10.1080/02786826.2019.1676878.

Liu, X., Huey, L.G., Yokelson, R.J., Selimovic, V., Simpson, I.J., Müller, M., Jimenez, J.L., Campuzano-Jost, P., Beyersdorf, A.J., Blake, D.R., Butterfield, Z., Choi, Y., Crounse, J.D., Day, D.A., Diskin, G.S., Dubey, M.K., Fortner, E., Hanisco, T.F., Hu, W., King, L.E., Kleinman, L., Meinardi, S., Mikoviny, T., Onasch, T.B., Palm, B.B., Peischl, J., Pollack, I.B., Ryerson, T.B., Sachse, G.W., Sedlacek, A.J., Shilling, J.E., Springston, S., Clair, J.M.S., Tanner, D.J., Teng, A.P., Wennberg, P.O., Wisthaler, A., and Wolfe, G.M. (2017). Airborne measurements of western U.S. wildfire emissions: Comparison with prescribed burning and air quality implications. *Journal of Geophysical Research: Atmospheres* 122 (11):6108–6129. doi:https://doi.org/10.1002/2016JD026315.

Lund, M.T., Myhre, G., Haslerud, A.S., Skeie, R.B., Griesfeller, J., Platt, S.M., Kumar, R., Myhre, C.L., and Schulz, M. (2018). Concentrations and radiative forcing of anthropogenic aerosols from 1750 to 2014 simulated with the Oslo CTM3 and CEDS emission inventory. *Geoscientific Model Development* 11 (12):4909–4931. doi:10.5194/gmd-11-4909-2018.

Massoli, P., Bates, T.S., Quinn, P.K., Lack, D.A., Baynard, T., Lerner, B.M., Tucker, S.C., Brioude, J., Stohl, A., and Williams, E.J. (2009). Aerosol optical and hygroscopic properties during TexAQS-GoMACCS 2006 and their impact on aerosol direct radiative forcing. *Journal of Geophysical Research: Atmospheres* 114 (D7). doi:10.1029/2008JD011604.

McMeeking, G.R., Fortner, E., Onasch, T.B., Taylor, J.W., Flynn, M., Coe, H., and Kreidenweis, S.M. (2014). Impacts of nonrefractory material on light absorption by aerosols emitted from biomass burning. *Journal of Geophysical Research: Atmospheres* 119 (21):12,272-12,286. doi:https://doi.org/10.1002/2014JD021750.

McNamara, M.L., Thornburg, J., Semmens, E.O., Ward, T.J., and Noonan, C.W. (2017). Reducing indoor air pollutants with air filtration units in wood stove homes. *Science of The Total Environment* 592:488–494. doi:10.1016/j.scitotenv.2017.03.111.

Mikhailov, E.F., Vlasenko, S.S., Podgorny, I.A., Ramanathan, V., and Corrigan, C.E. (2006). Optical properties of soot–water drop agglomerates: An experimental study. *Journal of Geophysical Research: Atmospheres* 111 (D7). doi:10.1029/2005JD006389.

Modini, R.L., Corbin, J.C., Brem, B.T., Irwin, M., Bertò, M., Pileci, R.E., Fetfatzis, P., Eleftheriadis, K., Henzing, B., Moerman, M.M., Liu, F., Müller, T., and Gysel-Beer, M. (2021). Detailed characterization of the CAPS single-scattering albedo monitor (CAPS PMssa) as a field-deployable instrument for measuring aerosol light absorption with the extinction-minus-scattering method. *Atmospheric Measurement Techniques* 14 (2):819–851. doi:10.5194/amt-14-819-2021.

Moffet, R.C. and Prather, K.A. (2009). In-situ measurements of the mixing state and optical properties of soot with implications for radiative forcing estimates. *Proceedings of the National Academy of Sciences* 106 (29):11872–11877. doi:10.1073/pnas.0900040106.

Mohr, C., Huffman, A., Cubison, M.J., Aiken, A.C., Docherty, K.S., Kimmel, J.R., Ulbrich, I.M., Hannigan, M., and Jimenez, J.L. (2009). Characterization of primary organic aerosol emissions from meat cooking, trash burning, and motor vehicles with high-resolution aerosol mass spectrometry and comparison with ambient and chamber observations. *Environ Sci Technol* 43 (7):2443–2449. doi:10.1021/es8011518.

Moschos, V., Kumar, N.K., Daellenbach, K.R., Baltensperger, U., Prévôt, A.S.H., and El Haddad, I. (2018). Source Apportionment of Brown Carbon Absorption by Coupling Ultraviolet–Visible Spectroscopy with Aerosol Mass Spectrometry. *Environ. Sci. Technol. Lett.* 5 (6):302–308. doi:10.1021/acs.estlett.8b00118.

Ohata, S., Schwarz, J.P., Moteki, N., Koike, M., Takami, A., and Kondo, Y. (2016). Hygroscopicity of materials internally mixed with black carbon measured in Tokyo. *Journal of Geophysical Research: Atmospheres* 121 (1):362–381. doi:10.1002/2015JD024153.

Onasch, T.B., Massoli, P., Kebabian, P.L., Hills, F.B., Bacon, F.W., and Freedman, A. (2015). Single Scattering Albedo Monitor for Airborne Particulates. *Aerosol Science and Technology* 49 (4):267–279. doi:10.1080/02786826.2015.1022248.

Peng, J., Hu, M., Guo, S., Du, Z., Zheng, Jing, Shang, D., Levy Zamora, M., Zeng, L., Shao, M., Wu, Y.-S., Zheng, Jun, Wang, Y., Glen, C.R., Collins, D.R., Molina, M.J., and Zhang, R. (2016). Markedly enhanced absorption and direct radiative forcing of black carbon under polluted urban environments. *Proceedings of the National Academy of Sciences* 113 (16):4266–4271. doi:10.1073/pnas.1602310113.

Port Statistics (n.d.). *Port Houston*. Available at https://porthouston.com/about/our-port/statistics/ (Accessed 3 December 2024).

Quinn, P.K., Bates, T.S., Baynard, T., Clarke, A.D., Onasch, T.B., Wang, W., Rood, M.J., Andrews, E., Allan, J., Carrico, C.M., Coffman, D., and Worsnop, D. (2005). Impact of particulate organic matter on the relative humidity dependence of light scattering: A simplified parameterization. *Geophysical Research Letters* 32 (22). doi:10.1029/2005GL024322.

Ramanathan, V. and Carmichael, G. (2008). Global and regional climate changes due to black carbon. *Nature Geoscience* 1 (4):221–227. doi:10.1038/ngeo156.

Ramanathan, V., Chung, C., Kim, D., Bettge, T., Buja, L., Kiehl, J.T., Washington, W.M., Fu, Q., Sikka, D.R., and Wild, M. (2005). Atmospheric brown clouds: Impacts on South Asian climate and hydrological cycle. *Proceedings of the National Academy of Sciences* 102 (15):5326–5333. doi:10.1073/pnas.0500656102.

Rocha-Lima, A., Martins, J.V., Remer, L.A., Todd, M., Marsham, J.H., Engelstaedter, S., Ryder, C.L., Cavazos-Guerra, C., Artaxo, P., Colarco, P., and Washington, R. (2018). A detailed characterization of the Saharan dust collected during the Fennec campaign in 2011: in situ ground-based and laboratory measurements. *Atmospheric Chemistry and Physics* 18 (2):1023–1043. doi:10.5194/acp-18-1023-2018.

Rodriguez-Navarro, C., di Lorenzo, F., and Elert, K. (2018). Mineralogy and physicochemical features of Saharan dust wet deposited in the Iberian Peninsula during an extreme red rain event. *Atmospheric Chemistry and Physics* 18 (13):10089–10122. doi:10.5194/acp-18-10089-2018.

Saliba, G., Subramanian, R., Saleh, R., Ahern, A.T., Lipsky, E.M., Tasoglou, A., Sullivan, R.C., Bhandari, J., Mazzoleni, C., and Robinson, A.L. (2016). Optical properties of black carbon in cookstove emissions coated with secondary organic aerosols: Measurements

and modeling. *Aerosol Science and Technology* 50 (11):1264–1276. doi:10.1080/02786826.2016.1225947.

Scarnato, B.V., Vahidinia, S., Richard, D.T., and Kirchstetter, T.W. (2013). Effects of internal mixing and aggregate morphology on optical properties of black carbon using a discrete dipole approximation model. *Atmospheric Chemistry and Physics* 13 (10):5089–5101. doi:10.5194/acp-13-5089-2013.

Schnaiter, M., Horvath, H., Möhler, O., Naumann, K.-H., Saathoff, H., and Schöck, O.W. (2003). UV-VIS-NIR spectral optical properties of soot and soot-containing aerosols. *Journal of Aerosol Science, Intercomparison of Soot Measurement Techniques* 34 (10):1421–1444. doi:10.1016/S0021-8502(03)00361-6.

Schnaiter, M., Linke, C., Möhler, O., Naumann, K.-H., Saathoff, H., Wagner, R., Schurath, U., and Wehner, B. (2005). Absorption amplification of black carbon internally mixed with secondary organic aerosol. *Journal of Geophysical Research: Atmospheres* 110 (D19). doi:10.1029/2005JD006046.

Schwarz, J.P., Gao, R.S., Fahey, D.W., Thomson, D.S., Watts, L.A., Wilson, J.C., Reeves, J.M., Darbeheshti, M., Baumgardner, D.G., Kok, G.L., Chung, S.H., Schulz, M., Hendricks, J., Lauer, A., Kärcher, B., Slowik, J.G., Rosenlof, K.H., Thompson, T.L., Langford, A.O., Loewenstein, M., and Aikin, K.C. (2006). Single-particle measurements of midlatitude black carbon and light-scattering aerosols from the boundary layer to the lower stratosphere. *Journal of Geophysical Research: Atmospheres* 111 (D16). doi:10.1029/2006JD007076.

Seinfeld, J.H. and Pandis, S.N. (2016). Atmospheric Chemistry and Physics: From Air Pollution to Climate Change. John Wiley & Sons.

Shaughnessy, R.J. and Sextro, R.G. (2006). What Is an Effective Portable Air Cleaning Device? A Review. *Journal of Occupational and Environmental Hygiene* 3 (4):169–181. doi:10.1080/15459620600580129.

Slowik, J.G., Cross, E.S., Han, J.-H., Davidovits, P., Onasch, T.B., Jayne, J.T., Williams, L.R., Canagaratna, M.R., Worsnop, D.R., Chakrabarty, R.K., Moosmüller, H., Arnott, W.P., Schwarz, J.P., Gao, R.-S., Fahey, D.W., Kok, G.L., and Petzold, A. (2007). <no title>.

Szopa, S., Naik, V., Adhikary, B., Artaxo, P., Berntsen, T., Collins, W.D., Fuzzi, S., Gallardo, L., Kiendler-Scharr, A., Klimont, Z., Liao, H., Unger, N., and Zanis, P. (2023). Short-Lived Climate Forcers. In Climate Change 2021: The Physical Science Basis. Contribution of Working Group I to the Sixth Assessment Report of the Intergovernmental Panel on Climate Change, 1st ed. Cambridge University Press.

Titos, G., Cazorla, A., Zieger, P., Andrews, E., Lyamani, H., Granados-Muñoz, M.J., Olmo, F.J., and Alados-Arboledas, L. (2016). Effect of hygroscopic growth on the aerosol light-scattering coefficient: A review of measurements, techniques and error sources. *Atmospheric Environment* 141:494–507. doi:10.1016/j.atmosenv.2016.07.021.

Williams, A.I.L., Stier, P., Dagan, G., and Watson-Parris, D. (2022). Strong control of effective radiative forcing by the spatial pattern of absorbing aerosol. *Nat. Clim. Chang.* 12 (8):735–742. doi:10.1038/s41558-022-01415-4.

Xie, C., Xu, W., Wang, J., Liu, D., Ge, X., Zhang, Q., Wang, Q., Du, W., Zhao, J., Zhou, W., Li, J., Fu, P., Wang, Z., Worsnop, D., and Sun, Y. (2019). Light absorption enhancement of black carbon in urban Beijing in summer. *Atmospheric Environment* 213:499–504. doi:10.1016/j.atmosenv.2019.06.041.

You, R., Radney, J.G., Zachariah, M.R., and Zangmeister, C.D. (2016). Measured Wavelength-Dependent Absorption Enhancement of Internally Mixed Black Carbon with Absorbing and Nonabsorbing Materials. *Environ. Sci. Technol.* 50 (15):7982–7990. doi:10.1021/acs.est.6b01473.

Yuan, W., Huang, R.-J., Yang, L., Guo, J., Chen, Z., Duan, J., Wang, T., Ni, H., Han, Y., Li, Y., Chen, Q., Chen, Y., Hoffmann, T., and O'Dowd, C. (2020). Characterization of the light-absorbing properties, chromophore composition and sources of brown carbon aerosol in Xi'an, northwestern China. *Atmospheric Chemistry and Physics* 20 (8):5129–5144. doi:10.5194/acp-20-5129-2020.

Yuan, W., Huang, R.-J., Yang, L., Wang, T., Duan, J., Guo, J., Ni, H., Chen, Y., Chen, Q., Li, Y., Dusek, U., O'Dowd, C., and Hoffmann, T. (2021). Measurement report: $PM_{2.5}$-bound nitrated aromatic compounds in Xi'an, Northwest China – seasonal variations and contributions to optical properties of brown carbon. *Atmospheric Chemistry and Physics* 21 (5):3685–3697. doi:10.5194/acp-21-3685-2021.

Zarzana, K.J., Cappa, C.D., and Tolbert, M.A. (2014). Sensitivity of Aerosol Refractive Index Retrievals Using Optical Spectroscopy. *Aerosol Science and Technology* 48 (11):1133–1144. doi:10.1080/02786826.2014.963498.

Zhang, R., Khalizov, A.F., Pagels, J., Zhang, D., Xue, H., and McMurry, P.H. (2008). Variability in morphology, hygroscopicity, and optical properties of soot aerosols during atmospheric processing. *Proceedings of the National Academy of Sciences* 105 (30):10291–10296. doi:10.1073/pnas.0804860105.

Zhang, X., Massoli, P., Quinn, P.K., Bates, T.S., and Cappa, C.D. (2014). Hygroscopic growth of submicron and supermicron aerosols in the marine boundary layer. *Journal of Geophysical Research: Atmospheres* 119 (13):8384–8399. doi:10.1002/2013JD021213.

Zhang, Y., Forrister, H., Liu, J., Dibb, J., Anderson, B., Schwarz, J.P., Perring, A.E., Jimenez, J.L., Campuzano-Jost, P., Wang, Y., Nenes, A., and Weber, R.J. (2017). Top-of-atmosphere radiative forcing affected by brown carbon in the upper troposphere. *Nature Geoscience* 10 (7):486–489. doi:10.1038/ngeo2960.

Zhou, J., Xu, X., Zhao, W., Fang, B., Liu, Q., Cai, Y., Zhang, W., Venables, D.S., and Chen, W. (2020). Simultaneous measurements of the relative-humidity-dependent aerosol light extinction, scattering, absorption, and single-scattering albedo with a humidified cavity-enhanced albedometer. *Atmospheric Measurement Techniques* 13 (5):2623–2634. doi:10.5194/amt-13-2623-2020.

4.14 Supplemental Figures for: Characterization of Absorption by Black Carbon, Brown Carbon, and Dust Aerosols During the TRACER Field Campaign in Houston, TX

Authors: Rachael Dal Porto[1], Kyle Gorkowski[2], James E. Lee[2], Ryan N. Farley[2,3,4], Zewen Zheng[3], Katherine B. Benedict[2], Allison C. Aiken[2], Manvendra K. Dubey[2], Qi Zhang[2,3], Christopher D. Cappa[1]

[1]Department of Civil and Environmental Engineering, University of California, Davis, CA, 95616 USA

[2]Earth and Environmental Sciences Division, Los Alamos National Laboratory, Los Alamos, NM, USA

[3]Agricultural and Environmental Chemistry Graduate Group, University of California Davis, CA, 95616, USA

[4]Earth and Environmental Sciences Division, Los Alamos National Laboratory, Los Alamos, NM, USA

CONTACT Christopher D. Cappa cdcappa@ucdavis.edu

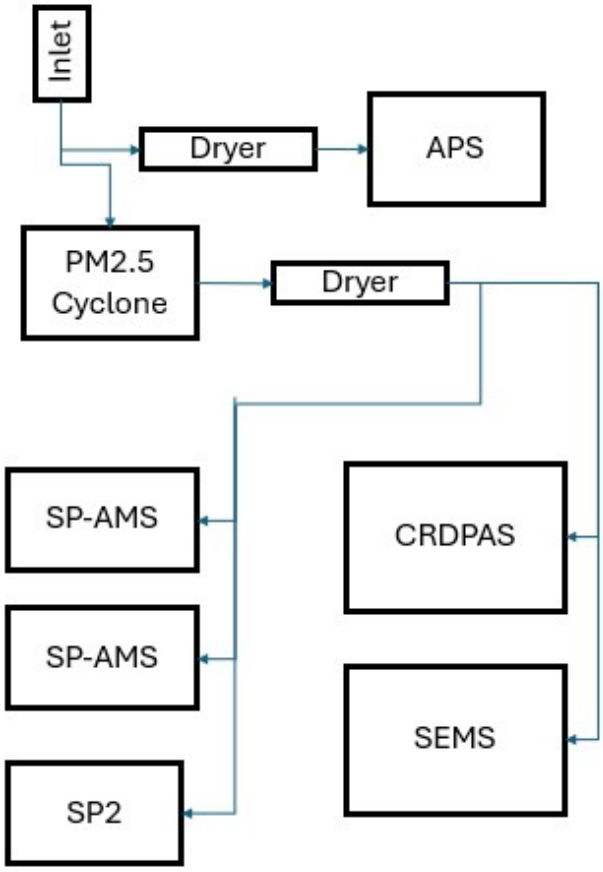

*Figure S**4-1**: Campaign Instrument Set Up Schematic. Instrumentation includes: cavity ringdown spectroscopy (CRDS) and photoacoustic spectroscopy (PAS) (together CRDPAS), a scanning electrical mobility spectrometer (SEMS) and an aerodynamic particle sizer (APS), two high-resolution soot particle aerosol mass spectrometers (SP-AMS), one laser only and one dual vaporizer, an a single particle soot photometer (SP2).*

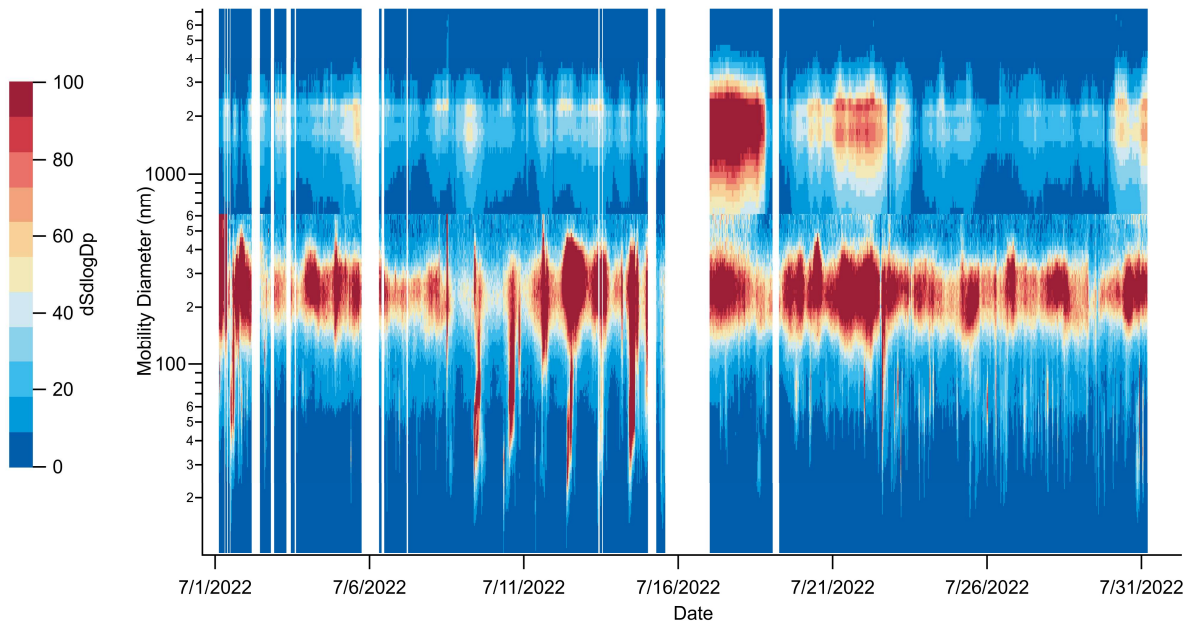

Figure S4-2: Image plot of dSdlogDp, where the cut diameter shown corresponds to the size where there is a clear minimum between the SEMS (bottom) mode, and APS (top) mode in the surface area-weighted size distribution

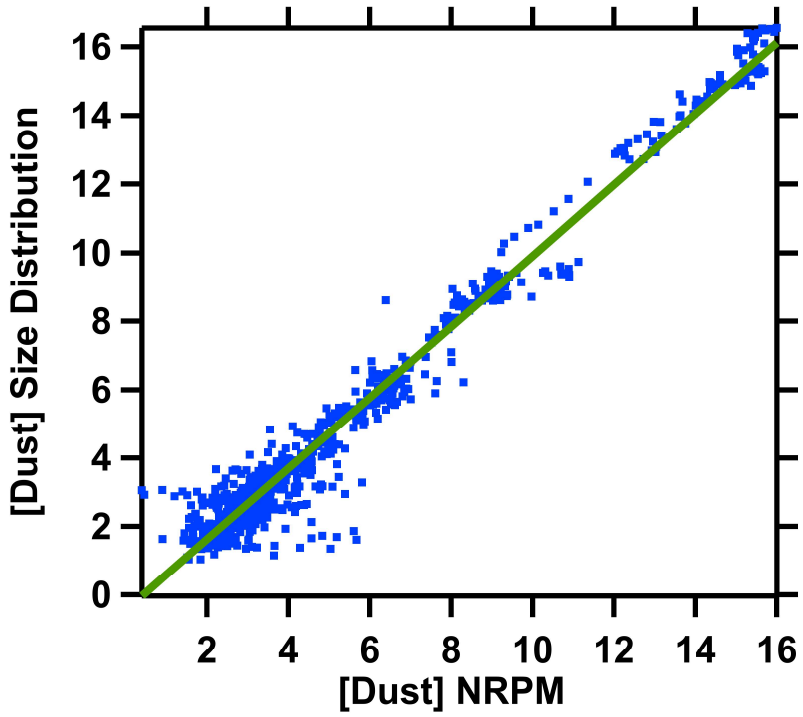

Figure S4-3: Comparison of dust concentrations derived with the y axis representing dust mass concentration as estimated using the size distribution method, and the x-axis representing dust mass concentration as estimated using the NRPM method. The two methods agree well with a slope of 1.0351 and $r^2 = 0.97$.

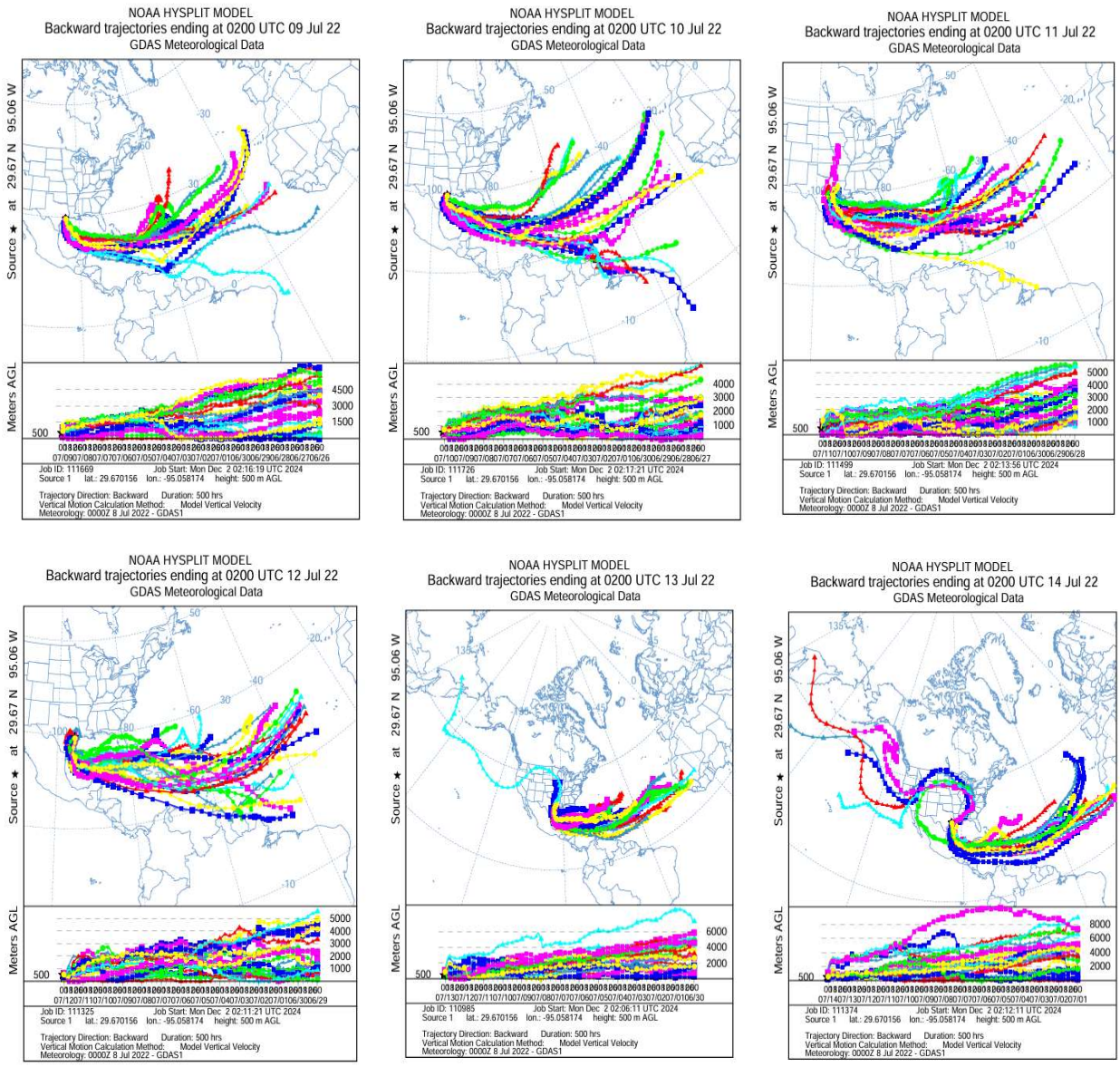

*Figure S**4-4** NOAA Hysplit models from July 9th to July 14th, 2022. All back trajectories start from the same location, and run for the same amount of time.*

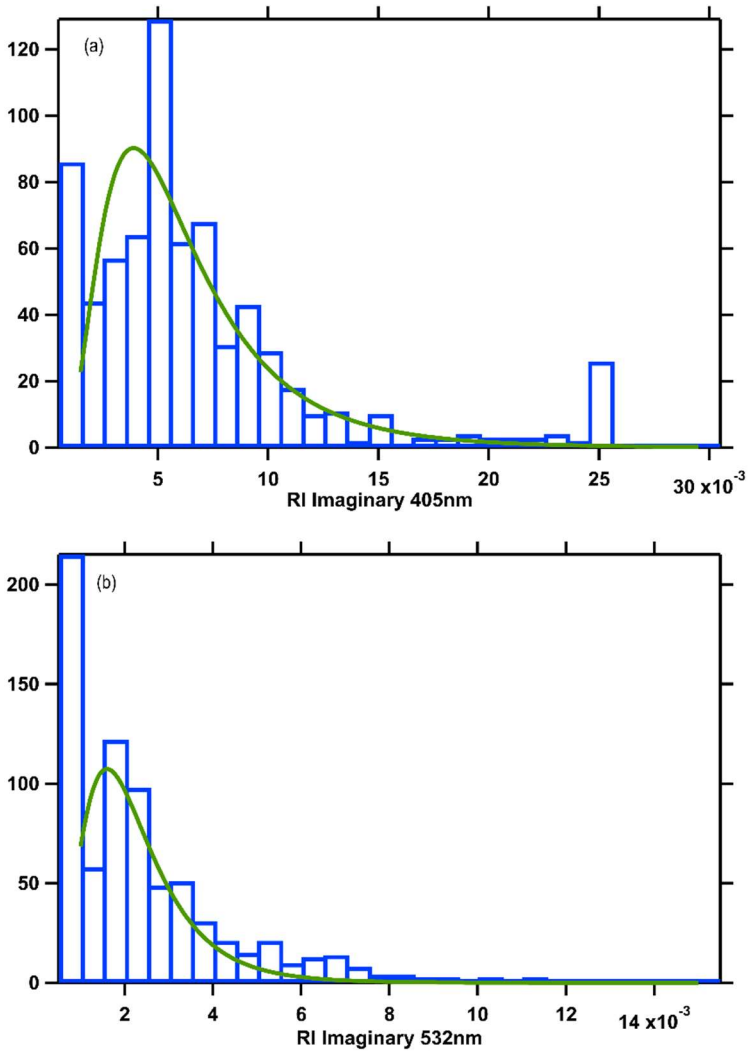

*Figure S**4-5:*** Histograms for retrieved dust imaginary refractive index, panel (a) is the log-normally distributed imaginary index at 405nm, while panel (b) is the log-normally distributed imaginary index at 532nm. A log-normal fit to the distributions yields k_{dust}(405 nm) = 0.0039 and k_{dust} (532 nm) = 0.0016.

5 Conclusion

This dissertation examined three unique aspects of aerosols; advancements in DIY air filtration systems, the development and application of a humidified-cavity attenuated phase shift spectrometer (HCAPS), and insights into aerosol optical properties during field campaigns.

- A low-cost DIY air cleaner, the Corsi-Rosenthal Box (CR Box), was examined to determine efficiency in removing indoor aerosols. For particles greater than 0.5 microns, the system achieves a Clean Air Delivery Rate (CADR) of over 600 ft^3/min (1019 m^3/h) at the lowest fan speed for particles with a median diameter of 1.2 microns. This performance surpasses most commercially available air cleaners. At the highest fan speed, the CADR increases to 850 ft^3/min (1444 m^3/h), albeit with an increase in noise level from 58 dB at low speed to 67 dB at high speed. The CR Box is also highly cost-efficient, with a cost-normalized CADR of less than \$0.072/ft^3/min. This study provides confidence in the performance of this accessible air cleaner in providing homes, offices, or classrooms with efficient air filtration. Future work could focus on reducing noise without compromising performance, evaluating filtration efficiency for smaller particle sizes, and testing alternative designs using different fans and filters or varying filter configurations.
- This dissertation also examined aerosols as they apply to the global climate. Instrumentation was created to bolster the cavity attenuated phase shift spectrometer and retrofit the instrument with a humidifier box to allow for measurements of absorption enhancement on lab generated or ambient aerosols (HCAPS). In addition to the addition of the RH Box, this work added a humidification aspect to the current truncation correction method. Mie theory was used and built upon to account for water uptake when

applying the truncation correction factor to measurements made by the HCAPS, improving reliability of the instrument. This method, validated using ammonium sulfate particles, considers changes in refractive index due to aerosol hygroscopicity. Measurements with nigrosine and fullerene soot particles reveal that nigrosine exhibits modest absorption enhancement at 85% relative humidity (f(RH)abs ~1.1), reflecting its partial solubility, while fullerene soot shows no enhancement, consistent with its non-hygroscopic nature. These findings highlight the instrument's sensitivity to water-uptake-induced absorption changes, which can inform future studies on mixed-component aerosols and complement field observations to refine global aerosol absorption models.

- Lastly, field measurements were made in Houston, Texas during the TRACER field campaign to analyze the relative contribution of BC, BrC and dust to absorption. We found significant absorption from BC, with two notable dust events, and small influence from BrC. Black carbon was the dominant absorber, contributing 61% of absorption at 405 nm and 75% at 532 nm. Dust contributed 34% and 16%, respectively, while brown carbon contributed 6% and 9%. While BC and organic aerosol exhibited modest correlations, nitrate was found to potentially influence brown carbon absorption. Dust, likely transported from the Sahara Desert, showed weak correlations with nitrate, suggesting chemical processing during transit. Refractive index values for dust were determined as k=0.00396 at 405 nm and k=0.0016 at 532 nm, while variability in hygroscopicity indicated the influence of dust, organic aerosols, sea spray, and atmospheric processing. The study underscores the importance of considering interactions between aerosol components, hygroscopic properties, and chemical transformations to accurately assess aerosol impacts on climate.